Structural and optoelectronic properties of heterogeneous metal-halide perovskites from first principles

Von der Universität Bayreuth
zur Erlangung des Grades eines
Doktors der Naturwissenschaften (Dr. rer. nat.)
genehmigte Abhandlung

von

Raisa-Ioana Biega

aus Slobozia, Rumänien

1. Gutachter: Dr. Linn Leppert
2. Gutachter: Prof. Dr. Stephan Kümmel
3. Gutachter: Prof. Dr. Caterina Cocchi

Tag der Einreichung: 11.08.2021
Tag des Kolloquiums: 14.01.2022

Abstract

The development of high-performance light harvesting devices has been one of the main focuses of the photovoltaics community and materials with high crystallinity and low defect concentrations have been thought to be the perfect candidates. In the past decade metal-halide perovskites have challenged this conventional understanding of semiconducting behavior. They have successfully been used in optoelectronic applications with unexpected and remarkably high efficiencies, despite the significant inhomogeneities in local chemistry, defect density, and lattice structure introduced through the facile synthesis methods typically used to grow perovskite films for photovoltaic applications. Furthermore, the full material class of halide perovskites exhibits tremendous chemical and structural heterogeneity leading to a great diversity of optoelectronic properties. This thesis contributes to the atomistic understanding of the effect of different forms of heterogeneity on structural and optoelectronic properties of metal-halide perovskites through an in-depth theoretical study using state-of-the-art first principles calculations.

Double metal-halide perovskites are an emerging class of materials with promising semiconducting properties. In these materials, chemical heterogeneity is introduced through the alternating mono- and trivalent metal cations that build the inorganic crystalline lattice. We use density functional theory and *ab initio* many-body perturbation theory within the G_0W_0 approximation and the Bethe-Salpeter equation approach to study the effect of this chemical heterogeneity on the electronic and excited state structure of halide double perovskites. We find that the magnitude of exciton binding energies and the significance of local field effects in these materials are highly dependent on their band edge orbital character and thus provide atomistic insight into light-matter interactions in this technologically relevant class of materials.

By lowering the dimensionality of both single and double metal-halide perovskites via incorporation of large organic molecules, additional structural heterogeneity is introduced because of symmetry breaking along one direction. We perform first principles density functional theory calculations to investigate the effect of macroscopic structural hetero-

geneity on the structural and electronic properties of such quasi-2D single and double perovskites. We disentangle the effects of chemical substitution, atomic structure, and dimensionality on the electronic structure of these systems and find significant steric effects and band gap changes in both single and double quasi-2D materials in stark difference to their 3D counterparts.

Finally, we study local structural microscale heterogeneities in the all-inorganic halide perovskite $CsPbBr_3$ introduced through intrinsic defects, focusing specifically on halogen-mediated vacancy migration, which has been demonstrated to contribute the most to phase segregation and material degradation. We perform first principles density functional theory calculations to compute energy barriers and minimum-energy pathways of bromine vacancy migration in the bulk and at the surface of cubic $CsPbBr_3$. Moreover, we analyze the effect of macroscopic structural heterogeneities at the surface by passivation of the perovskite surface with alkali-halide monolayers. Our results show that the undesirable substantially lower migration barrier at the surface can be mitigated through passivation with suitable alkali-halide monolayers.

Kurzdarstellung

Die Entwicklung effizienter Solarzellen ist einer der Hauptschwerpunkte der Photovoltaik-Community und hochkristalline Materialien mit geringer Defektkonzentration gelten als die perfekten Kandidaten dafür. In den letzten zehn Jahren haben Metall-Halogenid-Perowskite dieses konventionelle Verständnis des Halbleiterverhaltens in Frage gestellt. Sie wurden erfolgreich in optoelektronischen Anwendungen mit unerwarteten, bemerkenswert hohen Wirkungsgraden eingesetzt, trotz der erheblichen Inhomogenitäten in lokaler Chemie, Defektdichte und Gitterstruktur, die durch die einfachen Synthesemethoden, die typischerweise zum Züchten von Perowskitfilmen für photovoltaische Anwendungen verwendet werden, eingeführt wurden. Darüber hinaus weist die gesamte Materialklasse der Halogenid-Perowskite eine enorme chemische und strukturelle Heterogenität auf, die zu einer großen Vielfalt optoelektronischer Eigenschaften führt. Diese Dissertation trägt zum atomistischen Verständnis des Einflusses verschiedener Formen der Heterogenität auf strukturelle und optoelektronische Eigenschaften von Metall-Halogenid-Perowskiten durch eine eingehende theoretische Studie unter Verwendung modernster first-principles Rechnungen bei.

Metall-Halogenid Doppelperowskite sind eine Materialklasse mit vielversprechenden halbleitenden Eigenschaften. In diesen Materialien hat chemische Heterogenität ihren Ursprung in den abwechselnden ein- und dreiwertigen Metallkationen, die das anorganische Kristallgitter bilden. Wir verwenden Dichtefunktionaltheorie und *ab initio* Vielteilchenstörungstheorie innerhalb der G_0W_0 Näherung und der Bethe-Salpeter-Gleichung, um den Einfluss dieser chemischen Heterogenität auf die elektronische Struktur und die angeregten Zustände von Halogenid-Doppelperowskiten zu untersuchen. Wir stellen fest, dass die Größe der Exzitonenbindungsenergien und die Bedeutung lokaler Feldeffekte in diesen Materialien stark von ihrem Bandkantenorbitalcharakter abhängen und liefern damit atomistische Einblicke in Licht-Materie-Wechselwirkungen in dieser technologisch relevanten Materialklasse.

Durch die Verringerung der Dimensionalität sowohl von Einfach- als auch Doppelper-

owskiten durch den Einbau großer organischer Moleküle wird zusätzliche strukturelle Heterogenität aufgrund von Symmetriebrechung entlang einer Richtung eingeführt. Wir führen first principles Dichtefunktionaltheorie Rechnungen durch, um den Einfluss makroskopischer struktureller Heterogenität auf die strukturellen und elektronischen Eigenschaften solcher quasi-2D Einzel- und Doppelperowskite zu untersuchen. Dabei untersuchen wir systematisch die Auswirkungen chemischer Substitution, atomarer Struktur und Dimensionalität auf die elektronische Struktur dieser Systeme und finden signifikante sterische Effekte und Bandstrukturänderungen sowohl in einfachen als auch in doppelten quasi-2D Materialien, die sich deutlich von ihren 3D Gegenstücken unterscheiden.

Schließlich untersuchen wir lokale strukturelle Heterogenitäten durch intrinsische Defekte im rein anorganischen Halogenid-Perowskits $CsPbBr_3$, wobei wir uns speziell auf die halogenvermittelte Leerstellenmigration konzentrieren, die nachweislich am stärksten zur Phasensegregation und zum Materialabbau beiträgt. Wir führen first principles Berechnungen durch, um Energiebarrieren und Pfade minimaler Energie für die Migration von Brom-Leerstellen im bulk und an der Oberfläche von kubischem $CsPbBr_3$ zu berechnen. Darüber hinaus analysieren wir den Einfluss makroskopischer struktureller Heterogenitäten an der Oberfläche durch Passivierung der Perowskitoberfläche mit Alkalihalogenid-Monolagen. Unsere Ergebnisse zeigen, dass die unerwünschte, wesentlich niedrigere Migrationsbarriere an der Oberfläche durch Passivierung mit geeigneten Alkalihalogenid-Monolagen abgeschwächt werden kann.

Contents

Chapter 1

Introduction

The global energy demand is known to continuously increase due to the economic and industrial growth in both developing and developed countries. Although traditional resources, e.g. coal, oil and gas, account for almost 75 % of the total energy production [1], they have also been leading to an alarming increase in pollution. Its dreadful consequences such as global warming and threats to human health, have stimulated intensive research to develop alternative renewable energy solutions. Fortunately, sunlight alone can provide sustainable energy exceeding the global consumption rate even in the most aggressive scenarios and thus, the direct use of solar energy seems to be one of the most promising alternative approaches to conventional energy generation. Photovoltaic devices converting solar energy into electricity are one of the main topics in the important challenge of developing new strategies to harvest solar energy. To design scalable and efficient light harvesting devices, a deeper understanding of the fundamental properties of absorber materials is of vital importance, therefore the relatively new computational science comes into play. Computational science, which in the recent years became an established complement to purely experimental and theoretical sciences, exploits available computer power to gain enriched understanding from basic laws of physics and forecast new properties and materials suitable for specific practical applications [2]. A key component of computational science is represented by the emerging field of materials modelling in which a very broad range of theoretical models are implemented to derive quantitative description of certain physical properties [3].

In this context, the present thesis focuses on the computational study of metal-halide perovskites, a very promising class of absorber candidates, and some of their fundamental physical properties that are critical for understanding and designing of optoelectronic applications. In the recent years, several reports showed, using various characterisation methods, that these materials feature tremendous structural and chemical heterogeneity [4–6]. Despite the fact that it has been suggested that the structural and chemical heterogeneity negatively impacts the device performance, metal-halide perovskites have been used in optoelectronic applications with outstanding efficiencies [7, 8].

The stoichiometry of metal-halide perovskites is described by the general chemical formula $AB^{II}X_3$, where A is an organic or anorganic cation, B^{II} is a divalent metal cation and X_3 is a halide anion. In the ideal cubic structure, the metal cations are octahedrally coordinated, while the halide anions form an inorganic lattice of corner-sharing B^{II}-centered octhahedra, with the A-site cations sitting in the center of the cuboctahedral cavities between octahedra. The prototypical metal-halide perovskite used in photovoltaic applications is methylammonium lead iodide ($MAPbI_3$, $MA{=}CH_3NH_3$) [9] and its common substitutes are other Pb-based perovskites due to their outstanding semiconducting properties [10, 11]. Although the facile growth of metal-halide perovskites through simple synthesis methods is one of the main advantages of this class of materials that would potentially help the industrialisation, it is also the main cause of variable and complex non-uniformities. The 'soft' lattice of perovskites accommodate pronounced local heterogeneity both on short length scales ($<100\,\mathrm{nm}$) and across long ranges ($>10\,\mu\mathrm{m}$) that impact their structural and optoelectronic properties [6]. The halt in large scale-commercialisation of Pb-based halide perovskites because of their poor stability against moisture, heat and light exposure [12, 13] motivated the search for finding various strategies to mitigate this issue and render new, more stable materials featuring the same advantageous properties. Here, we analyse several halide perovskites obtained using two of the most important strategies, i.e. dimensional reduction [14] and heterovalent substitution at metal site [15, 16]. These different approaches alter the stoichiometry of metal-halide perovskites and introduce additional global chemical and structural heterogeneity through successful incorporation of a wide range of chemical elements in the perovskite structure, leading to a tremendous diversity of optoelectronic properties.

The present thesis features two main parts concerned with the study of the impact of different macroscopic and microscopic inhomogeneities on the structural, electronic and optical properties of metal-halide perovskites. This analysis requires a theoretical framework that can accurately simulate the quantum phenomena involved in the absorption and processing of photons in these complex systems. Therefore, Chapter 2 briefly summarizes the theoretical background of the computational methods used throughout this thesis, covering density functional theory (DFT), *GW* formalism and Bethe-Salpeter equation (BSE) approach. Next, the impact of macroscopic inhomogeneities on electronic properties of metal-halide perovskite is discussed in Chapter 3. We bring into focus 2D Ruddlesden-Popper Pb-based perovskites in order to analyse how their overall structural heterogeneity influence the electronic structure of these materials. We then shift our attention to the emerging class of 3D double halide-perovskite (elpasolites) and their lower-dimensionality derivatives to study the effect of chemical heterogeneity through substitutions at metal sites. Chapter 4 is dedicated to the analysis of optical properties of several prominent members of Ag-pnictogen and Ag-icosagen double metal-halide perovskites $Cs_2AgB^{III}X_6$ with B^{III}=Bi, Sb, In, Tl and X_6=Cl, Br. Further, we discuss the applicability of a standard phenomenological theory typically used to gain insights from experimental data. In Chapter 5 we return to the fully-inorganic $CsPbBr_3$ perovskite to study the process of migration of one of the most common microscopical inhomogeneities, i.e. halogen vacancies. Finally, Chapter 6.1 provides a short summary and an outlook on the further investigations that can be carried out to deeper understand the compelling facts uncovered through this work. From a computational point of view, in order to reach correct and reliable conclusions, one must have a systematic understanding of the sensitivity of the results on the computational setup. Therefore all technical details of practical calculations presented through this thesis are provided in the Appendix.

Chapter 2

Theoretical framework

First principles calculations based on DFT, including spin-orbit coupling (SOC) for treating heavy atoms [17], represent a powerful tool for investigating both fully inorganic and hybrid organic-inorganic metal-halide perovskites [18, 19]. This approach has been widely used for computing structural, electronic and thermal properties such as fundamental band gaps, electron and hole effective masses, carrier mobilities, heat capacities and many other. In one prominent DFT study, Nagamatsu et al. used first principles calculations to compute the critical temperature of magnesium diboride (MgB_2) superconductor [20]. Another great progress in the field of materials modelling was represented by the atomic-scale simulation of the time evolution of nanoscale diamonds at low temperature using *ab initio* molecular dynamics methods [21], conducted by Raty et al. [22]. More recently, Filip et al. scanned a relatively wide range of lead-free perovskites in search for revolutionary materials to be used as absorbers in solar cells [23].

Despite the numerous studies employing DFT, the standard approximations used to DFT lead to notoriously underestimated band gaps [24], a drawback that driven great efforts to develop advanced techniques to yield reliable and accurate predictions. In order to overcome this shortcoming, new methods including the time–dependent DFT (TDDFT) [25], Green's function-based many-body perturbation theory (MBPT) [26–28] and Bethe-Salpeter equation (BSE) approach [29] have been developed and applied to recent theoretical calculations. It has been proven that the GW approach can be used to successfully predict (quasiparticle) band gaps and dispersion relations from first principles for solids [30–32], interfaces [33], and molecules [34]. Furthermore, used together with the BSE, it can predict optical properties of materials remarkably accurately [29, 35–37]. Typical calculations of the ground and excited–state properties using the GW+BSE method can be broken into three steps that will be briefly summarized over the next sections:

- the solution of the ground–state structural and electronic properties (section 2.1)
- the calculation of the quasiparticle energies and wavefunctions within the *GW* approximation for the electron self–energy operator (section 2.3)
- the calculation of the two–particle correlated electron–hole excited states through the solution of Bethe-Salpeter equation (section 2.4)

Exhaustive descriptions of the presented methodologies can be found in Refs. [3, 38, 39] for DFT, Refs. [26, 32, 40–44] for *GW* and Refs. [29, 45] for *GW*+BSE. Additional to this overview of the general methodology used throughout the thesis, in section 2.2 we present a specific DFT method routinely used to determine transition states in materials practically employed to describe the migration process of inhomogeneities of simple $CsPbBr_3$ metal-halide perovskite in chapter 5.

2.1. Density Functional Theory

A wide variety of computational and theoretical methodologies, all related or based on DFT, are nowadays used in state-of-the-art materials modelling [3]. This can only suggest that DFT is an effective technique for qualitatively and quantitatively investigating ground-state properties of materials. The foundations of DFT were first introduced by Hohenberg and Kohn in 1964, when they introduced the first *ab initio* model of interacting inhomogeneous electron gas [46].

2.1.1. Many-body Schrödinger equation

Complex materials are theoretically modelled as collections of electrons and nuclei glued together by the subtle interplay between repulsive (between pairs of electrons and pairs of nuclei, respectively) and attractive (between electrons and nuclei) Coulomb interactions [3]. In principle, their stationary behaviour can be described by solving the following associated many-body time-independent Schrödinger equation (in atomic units):

$$\begin{aligned}\Big[-\sum_i \frac{1}{2}\nabla_i^2 - \sum_I \frac{1}{2M_I}\nabla_I^2 + \frac{1}{2}\sum_{i\neq j}\frac{1}{|\mathbf{r}_i - \mathbf{r}_j|} \\ + \frac{1}{2}\sum_{I\neq J}\frac{Z_I Z_J}{|\mathbf{R}_I - \mathbf{R}_J|} - \sum_{i,I}\frac{Z_I}{|\mathbf{r}_i - \mathbf{R}_I|}\Big]\Psi = E_{\mathrm{tot}}\Psi,\end{aligned} \tag{2.1}$$

where M_I and Z_I represent the atomic masses and numbers, respectively, R_I and r_i are the positions of nuclei and electrons, respectively, Ψ is the total many-body wave function and E_{tot} is the total energy. We note that the indices i and j run from 1 to total number of electrons N, while the indices I and J run from 1 to total number of nuclei M. In practice, equation 2.1 is practically impossible to solve (with the exception of very small molecules) due to the very large number of component particles.

In the following, we assume the Born-Oppenheimer approximation [47], which decouples the degrees of freedom of electrons and nuclei, and only solve the Schrödinger equation of the electrons, assuming $M_I \to \infty$. In this assumption, the kinetic energy of nuclei can be neglected and the Coulomb repulsion between nuclei becomes constant, leading to the definition of the total electronic energy [3]:

$$E = E_{\text{tot}} - \frac{1}{2}\sum_{I \neq J} \frac{Z_I Z_j}{|\mathbf{R}_I - \mathbf{R}_J|}. \tag{2.2}$$

Furthermore, the nuclear coordinates can be treated as external parameters leading to Ψ becoming a function that describes electrons in a Coulomb potential created by the nuclei:

$$V_n(\mathbf{r}) = -\sum_I \frac{Z_I}{|\mathbf{r} - \mathbf{R}_I|}. \tag{2.3}$$

Following this deduction and using the relations 2.2 and 2.3 in equation 2.1, on can write the fundamental equation of electronic structure theory [3]:

$$\left[-\sum_i \frac{1}{2}\nabla_i^2 + \sum_i V_n(\mathbf{r}_i) + \frac{1}{2}\sum_{i \neq j} \frac{1}{|\mathbf{r}_i - \mathbf{r}_j|}\right]\Psi = E\Psi. \tag{2.4}$$

The first term in equation 2.4 represents the many-body Hamiltonian

$$\hat{H} = -\sum_i \frac{1}{2}\nabla_i^2 + \sum_i V_n(\mathbf{r}_i) + \frac{1}{2}\sum_{i \neq j} \frac{1}{|\mathbf{r}_i - \mathbf{r}_j|}, \tag{2.5}$$

where $\hat{T} = \sum_i \frac{1}{2}\nabla_i^2$ is the kinetic energy, $\hat{V}_{\text{ext}} = \sum_i V_n(\mathbf{r}_i)$ is the external potential of the nuclei and $\hat{v} = \frac{1}{2}\sum_{i \neq j} \frac{1}{|\mathbf{r}_i - \mathbf{r}_j|}$ is the electron-electron interaction.

As previously described in Ref. [3], the limitations of the many-body Schrödinger equation lie in the description of the Coulomb repulsion between electrons and stimulated extensive research to find methods that can treat the effects of electron-electron interactions with sufficient accuracy [48–54]. The most dramatic simplification is the independent electrons approximation which neglects the interactions between electrons, but introduces two considerable shortcomings. The solution of the Schrödinger equation within this approximation which can be written as as a product of independent single-particle wave functions [52] $\Psi(\mathbf{r}_1, \mathbf{r}_2, ..., \mathbf{r}_N) = \phi_1(\mathbf{r}_1)\phi_2(\mathbf{r}_2)...\phi_N(\mathbf{r}_N)$, does not obey Pauli's exclusion principle [55]. Furthermore, the Coulomb potential in equation 2.4 cannot actually be neglected since it is of the same order of magnitude as the other terms. A less drastic simplification that still assure a single-particle description is the mean-field approximation, which assumes that every electron "feels" the same average Hartree potential created by the other particles in the system [50]. Since the electrons are not classical particles, this approximation does not yield quantitatively accurate predictions of materials at atomic scale [3]. Further developing this reasoning, for a given Coulomb term, the energy can be minimised with respect to the variations of the orthonormal single-particle wave functions $\phi_i(\mathbf{r})$ and the concept of Hartree-Fock non-local potential arising from Pauli's exclusion principle is introduced for the first time [53]. The equations governing first principles materials modelling are derived in the Kohn-Sham approach that is an exact mapping of the interacting many-body problem onto a system of single particle equations, in which all quantum-mechanical exchange and correlation effects are by definition contained in the exchange-correlation potential.

2.1.2. Hohenberg and Kohn theorem

In general, the total electronic energy of any quantum state of a N-electron systems in equilibrium is a functional of the electronic wave function

$$E = E[\Psi(\mathbf{r}_1, \mathbf{r}_2, ..., \mathbf{r}_N)]. \tag{2.6}$$

The theorem of Hohenberg and Kohn [46] is based on three premises: first, the external potential of the nuclei in the ground state is uniquely determined by the electron density, second, the external potential in any quantum state is uniquely determined by the many-body electronic wave function and third, the total energy in any quantum state is a functional of the many-body electronic wave function. Combining these three presumptions, the total energy of of a many electron system in the ground state can be treated as a functional of the electron density:

$$E = E[n(\mathbf{r})]. \tag{2.7}$$

Furthermore, the total energy of the ground state can be obtained by minimising the total energy functional with respect to the electron density:

$$\frac{\delta E[n]}{\delta n} = 0. \tag{2.8}$$

Using the Rayleigh-Ritz variational principle, the previous relation can be written as:

$$E = \int d\mathbf{r} n(\mathbf{r}) V_n(\mathbf{r}) + \langle \Psi[n] | \hat{T} + \hat{v} | \Psi[n] \rangle , \tag{2.9}$$

where $\langle \Psi[n] | \hat{T} + \hat{v} | \Psi[n] \rangle$ is a universal functional which needs to be accurately determined in order to successfully describe the ground state of the many-electron system.

2.1.3. Kohn-Sham equations

While the first term in equation 2.9 explicitly depends on the electron density n, the dependence on the electron density is only implicit in the kinetic energy $\hat{T}$ and the Coulomb repulsion energy $\hat{W}$. To address this issue, Kohn and Sham [54] reformulated the energy functional as the sum between kinetic and Coulomb energy of independent electrons and an extra term accounting for the difference:

$$E[n] = T_s[n] + E_H[n] + E_{\text{ext}}[n] + E_{xc}[n], \tag{2.10}$$

where $T_s[n] = -\sum_i \int d\mathbf{r}\phi_i^*(\mathbf{r})\frac{\nabla^2}{2}\phi_i(\mathbf{r})$ is the kinetic energy of the non-interacting N-electron system, $E_H = \frac{1}{2}\iint d\mathbf{r}d\mathbf{r}'\frac{n(\mathbf{r})n(\mathbf{r}')}{|\mathbf{r}-\mathbf{r}'|}$ is the classical electrostatic Hartree energy and $E_{\text{ext}} = \int d\mathbf{r}n(\mathbf{r})V_n(\mathbf{r})$ is the external energy. The last term in equation 2.10 is the so-called exchange-correlation (xc) energy functional and it contains every contribution excluded from the first terms.

In order to accurately treat complex materials, the relativistic effect of spin-orbit coupling needs to be taken into account [56, 57] by solving the Dirac equations [58] where the single-particle Kohn-Sham wave functions are replaced by two-component spinors [54, 59] and the total energy needs to be minimised with respect to the electron density $n(\mathbf{r})$ and the spin density $n_\sigma(\mathbf{r})$ [3]. However, in the following all the equations will be written in a non-relativistic framework and assuming a spin-unpolarized system, for simplicity. Using the reformulation introduced in equation 2.10, the set of independent-particle equations can be written in a spin-unpolarized formulation that is generally known as the Kohn-Sham equations [54]:

$$\Big[T_s[n] + V_{\text{ext}}[n] + V_H[n] + V_{xc,\sigma}[n]\Big]\phi_n(\mathbf{r}) = \epsilon_n\phi_n(\mathbf{r}), \tag{2.11}$$

where $V_H[n] = \int d\mathbf{r}'\frac{n(\mathbf{r}')}{|\mathbf{r}-\mathbf{r}'|}$ is the Hartree potential and $V_{xc}[n] = \frac{\delta E_{xc}[n]}{\delta n}$ is the exchange-correlation potential. The external potential $V_{\text{ext}}[n]$ can be the exact, full potential or a so-called "pseudopotential", that replaces the strong Coulomb potential of the nuclei and the tightly bound core electrons by an effective ionic potential acting on the valence electrons only. ϵ_n and $\phi_n(\mathbf{r})$ are the Kohn-Sham eigenvalues and corresponding single-particle eigenfunctions, respectively. The electron density is defined as the sum over all occupied Kohn-Sham orbitals $\phi_n(\mathbf{r})$:

$$n(\mathbf{r}) = \sum_{i=1}^{N} f_n|\phi_n(\mathbf{r})|^2, \tag{2.12}$$

while the total number of electrons can be obtained by summing over all occupation numbers f_n:

$$N = \sum_{i=1}^{N} f_n. \tag{2.13}$$

In practical DFT calculations, the Kohn-Sham equations defined by 2.11, 2.12 and 2.13 are solved self-consistently until the variation of the electron density between two consecutive steps is smaller than a predefined threshold value.

2.1.4. Exchange-correlation approximations

In principle the Kohn-Sham equations 2.11 are exact and could be solved analytically. However, there is no known exact (closed) form of the xc potential and therefore, in practice one must resort to numerical approximations to solve these equations. In the following we will present only a brief summary of the approximations used in the calculations presented throughout the next chapters. A detailed overview of all different approximations can be found in Ref. [60].

The local density approximation (LDA) [61, 62] is the simplest approximation to the xc energy and it bears an explicit dependence on the electronic density. The hypothesis of LDA states that the xc energy in a complex system can be locally approximated with the xc energy in an homogeneous electron gas. This idea of constructing the xc energy of a real system using that of an homogeneous electron gas model has been suggested even before the DFT itself [48, 49, 63, 64]. Within this assumption, the exchange part at each $\mathbf{r}$ point depends only on the electron density at the same point:

$$E_x^{\mathrm{LDA}}[n(\mathbf{r})] = -\frac{3}{4}\left(\frac{3}{\pi}\right)^{1/3} \int n^{4/3}(\mathbf{r}) d\mathbf{r}. \tag{2.14}$$

In contrast, the correlation part has no known analytical form and it needs to be numerically computed using Monte-Carlo methods [61]. Based on these calculations, the correlation energy has been parametrized and therefore, several LDA energy functionals have been developed over the years [62, 65, 66]. Despite the rudimentary assumption that complex systems can be approximated with homogeneous electron gas, the LDA predicts surprisingly reasonable results for a large number of materials. However, the LDA leads to an absolute error of molecular atomization energies of the order of 1 eV [60].

Another class of xc energy approximations explicitly dependent on the electron density is the generalized gradient approximation (GGA), that improves the LDA by taking into account both the electron density at each $\mathbf{r}$ point as well as the rate of its spatial variation:

$$E_{xc}^{\mathrm{GGA}}[n(\mathbf{r})] = \int f(n(\mathbf{r}), \nabla n(\mathbf{r})) d\mathbf{r}. \tag{2.15}$$

The functional $f(n(\mathbf{r}), \nabla n(\mathbf{r}))$ in the expression of this semi-local approximation (equation 2.15) have been constructed such that it reproduces the exact result as good as possible. The GGA approximation of Perdew, Burke and Ernzerhof (PBE) [67] have been defined used this non-empirical framework, where all free parameters are determined to satisfy known exact constraints of the xc energy, and is currently one of the most common approximations used in computational materials modelling. Another approach to construct the functional $f(n(\mathbf{r}), \nabla n(\mathbf{r}))$ is to fit the xc energy to extensive sets of test molecules. An example of such an approximation is BLYP functional, which is parametrized semi-empirically and formed by the exchange functional of Becke [68] and the correlation functional of Lee, Yang and Parr [69]. Although GGA significantly improves the LDA results and renders good predictions for a wide range of materials, it still leads to an absolute error of molecular atomization energies of the order of 0.3 eV [60] and it even dramatically fails for certain systems because of the large self-interaction error (SIE) [62].

The so-called hybrid functionals have been designed to correct this drawback and soon became one of the most popular approximations used in computational chemistry. Within this framework firstly established by Becke [70], the xc energy is defined as the sum of three terms: a fraction of exact exchange E_x^{exact} and semi-local approximations of the correlation and exchange energy denoted by E_c^{approx} and E_x^{approx}, respectively:

$$E_{xc}^{\text{hybrid}} = \alpha E_x^{\text{exact}} + (1-\alpha) E_x^{\text{approx}} + E_c^{\text{approx}}. \tag{2.16}$$

Similar to the case of functional $f(n(\mathbf{r}), \nabla n(\mathbf{r}))$ in the formulation of GGA, the fraction α of exact exchange energy can be obtained either by fitting to large test sets of molecules or based on the adiabatic connection formalism [67, 71]. An example of such a hybrid approximation is the so-called PBE0 functional defined by Adamo et al., which is a variation of the previously described PBE [67], with $\alpha = 0.25$ [72].

Further developments on the hybrid functional lead to the range-separated hybrids (RSHs) constructed such that the exchange electron-electron interaction is split into a long-range (LR) and a short-range (SR) contribution. The importance of this approximation lies in the advantage of keeping the semi-local formulation of the exchange energy for the SR portion, while using fully non-local exchange energy for the LR part. An example of such approximation is the functional of Heyd Scuseria and Ernzerhof (HSE) [73], for which the xc energy takes the form:

$$E_{xc}^{\text{HSE}} = \alpha E_{x,SR}^{\text{exact}}(\omega) + (1-\alpha) E_{x,SR}^{\text{approx}}(\omega) + E_{x,LR}^{approx}(\omega) + E_c^{\text{approx}}, \tag{2.17}$$

where ω is a parameter used to tune the short-rangeness of the interaction. A particular variation of this approach that have been demonstrated to yield exceptional good results for a wide range of systems [74–76] is the so-called HSE06 functional where $\alpha = 0.25$ and $\omega = 0.2$ [77]. We further note that the previously described PBE0 functional [72] can be seen as a particular RSH case with $\omega = 0$.

2.2. The Nudged Elastic Band method

The motion of atoms within the crystal structure is an important process that is frequently studied in computational science to understand fundamental processes such as diffusion or to determine transition rates such as rates of chemical reactions.

The Nudget Elastic Band (NEB) is a geometry optimization technique used to compute the minimum energy pathway (MEP) between two given local minima of the potential energy surface [78]. Subsequently, the MEP is used to determine migration barrier for the transition between the initial and final states within harmonic transition state theory (hTST) [79]. An example of such a path is represented schematically in Figure 2.1, where we show a potential energy surface with two local minima representing the initial and final states and a maximum representing the saddle point between the fixed end points.

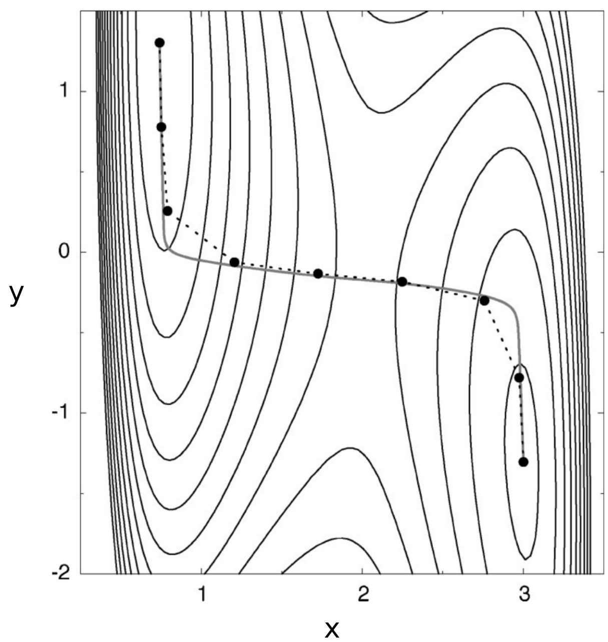

Figure 2.1: Schematic representation of nudged elastic band method reproduced from Ref. [80]. The dashed line is the elastic band converging to the MEP represented in solid line. The dots along the MEP represent the intermediate replicas of the system.

The MEP is achieved by optimising a number of images or replicas of the system along the reaction path [80]. These replicas are nothing else than geometrical configurations of the system in intermediate states between the initial and final points. The adjacent images are connected by springs to ensure the continuity of the path and simulate an elastic band. Once the elastic band is constructed, an optimisation of the band converges it to MEP [80]. In practice, the straightforward approach of disposing the images along a linear interpolation between the initial and final states is, most of the time, a good enough starting point for the optimization process leading to the MEP.

The optimisation of the elastic band is achieved by minimising the forces acting on the images. Note that within this constrained optimisation the forces are tangential at any point along the path [78, 80]. Assuming an elastic band described by the fixed end points $\mathbf{R_0}$, $\mathbf{R_N}$ and $N-1$ mobile intermediate images connected by identical springs with the spring constant k, the sum acting on force i is computed as the sum between the spring force and the true force:

$$F_i = F_i^S - \nabla E(\mathbf{R_i}), \tag{2.18}$$

where E represents the energy of the system, the spring force F_i^S is parallel and the true force $\nabla E(\mathbf{R_i})$ is perpendicular to the local tangent. The spring force is given by

$$F_i^S = k(|\mathbf{R_{i+1}} - \mathbf{R_i}| - |\mathbf{R_i} - \mathbf{R_{i-1}}|)\hat{\tau}_i, \tag{2.19}$$

where k is the spring constant and $\hat{\tau}_i$ is the normalized local tangent at image i. Note that, since we assumed the same k for all springs along the path, the images will converge to the MEP with equal spacing. Generally, because of the perpendicular force $\nabla E(\mathbf{R_i})$ the images around the saddle point will drift away from the local maximum [81]. Therefore, the discrete representation provided by the NEB is not sufficient and the saddle point has to be estimated using an interpolation scheme that can be problematic for a small number of intermediate images.

To surpass this crucial issue, especially important in the calculation of migration barriers, Henkelman et al. introduced the climbing image nudged elastic band method (cNEB) by modifying the above algorithm such that the highest energy image h is not affected by any spring force and as a result is driven to the saddle point [81]. The force acting on this climbing (saddle) image is given by

$$F_h = -\nabla E(\mathbf{R_h}) + 2\nabla E(\mathbf{R_h}) \cdot \hat{\tau}_h \hat{\tau}_h. \tag{2.20}$$

We note that due to the fact that the climbing image does not feel the spring forces, the spacing between the images on the either side of the saddle point in the final MEP will be different[81].

The (c)NEB method is an established tool to understand the transition paths in complex systems and have been successfully employed since late 1990s in combination with DFT[82–84] and with empirical potentials [78, 85, 86]. On of the important recent topic where the (c)NEB approached was used is the simulation of the ion migration process in metal-halide perovskites to gain knowledge about the migrating species and find ways to mitigate this undesirable effect[87–91].

2.3. *GW* formalism

The general aim of this thesis is to understand the structural, electronic and optical properties of some complex materials (namely, simple and double metal-halide perovskites).

One of the key quantities of our in-depth electronic structure analysis of the studied compounds is the fundamental band gap that we theoretically compute by performing quantum mechanical first principles calculations. In order to be relevant, the computed values needs to be compared with the corresponding experimentally determined band gaps.

One of the main drawbacks of using local and semi-local approximations for the exchange-correlation part in DFT is the severe underestimation of the band gaps of semiconductors and insulators with respect to experiment [62, 92]. A method to correct this misalignment is to use hybrid approximations, such as HSE screened hybrid functional that leads to very accurate results for solids with small to medium band gaps [60]. However, even HSE still significantly underestimates the band gap of insulators [93]. Furthermore, the implementation of such a hybrid functional in practical applications is notoriously difficult, limitations arising from the large number of particles necessary to accurately simulate a real system and the tuning procedures necessary for the determination of various parameters. Therefore, the aim of this section is to describe the GW approach. We note that the GW formalism is not computationally more efficient than DFT calculations using hybrid functionals, but is has the great advantage of being a parameter-free formalism. However, although GW approach is known to yield band gap energies in better agreement with the experimentally determined ones [94], this property should be seen with caution. In practice, G_0W_0, which is one of the most used flavors of GW shows a stark dependence of the DFT starting point [95] and therefore the advantage of being parameter-free is lost to some extent.

2.3.1. Theoretical spectroscopy

As described in Ref. [92], the band gap is generally defined as the difference between electron affinity and ionisation potential (IP). The ionisation potential is experimentally determined from photoelectron spectroscopy (PES) [96–98] and it is always below the Fermi level ($IP < E_F$). IP represents the photoexcitation energy from an N-particle ground state with total energy $E(N)$ into an excited state s of an $(N-1)$-particle system with total energy $E(N-1,s)$ upon removal of an electron [99]:

$$\varepsilon_s = E(N) - E(N-1,s). \tag{2.21}$$

The electron affinity (EA) is experimentally determined from inverse photoelectron spectroscopy (IPES) [100–102] and is at or above the Fermi level ($EA \geq E_F$). EA is defined as the addition energy released in the radiative transition in inverse photoemission given by the difference between $E(n+1,s)$ energy of an $(N+1)$-particle system in the excited state s and $E(n)$ energy of the N-particle system in its ground state [99]:

$$\varepsilon_s = E(N+1,s) - E(N), \tag{2.22}$$

The $(N-1)$- and $(N+1)$-particle systems are described by the transition amplitudes $\psi_s = \langle N-1, s|\, \hat{\psi}(\mathbf{r})\, |N\rangle$ and $\psi_s = \langle N|\, \hat{\psi}(\mathbf{r})\, |N+1, s\rangle$, respectively, where $\hat{\psi}(\mathbf{r})$ is the annihilation field operator.

Combining the equations 2.22 and 2.21, the energy of the band gap can be written as:

$$E_{\text{gap}} = [E(N+1) - E(N)] - [E(N) - E(N-1)] \,. \tag{2.23}$$

2.3.2. Single-particle propagator

In order to accurately compute E_{gap} defined by equation 2.23 one needs to be able to describe a quantum system with a variable number of particle. We therefore define the single-particle Green's function [44, 99, 103]:

$$G(\mathbf{r}, t, \mathbf{r}', t') = -i \langle N|\, \hat{T}\{\hat{\psi}(\mathbf{r}, t)\hat{\psi}^\dagger(\mathbf{r}', t')\}\, |N\rangle \,, \tag{2.24}$$

where $\langle N|$ is the normalized ground state many body function and the time-dependent field operators $\hat{\psi}(\mathbf{r}, t) = e^{iHt}\hat{\psi}(\mathbf{r})e^{-iHt}$ and $\hat{\psi}^\dagger(\mathbf{r}, t) = e^{iHt}\hat{\psi}^\dagger(\mathbf{r}, t)e^{-iHt}$ are expressed in the Heisenberg representation. $\hat{T}$ is Wick's time ordering operator [104] that arranges the operators so that time decreases from left to right and the earlier time acts on the ground state $\langle N|$ first. Both time orderings $t > t'$ and $t' > t$ are affordable in $G(\mathbf{r}, t, \mathbf{r}', t')$ leading to retarded (G^+) and advance (G^-) Green's function. Equation 2.24 describes the scenario where an electron with spin σ injected at point $\mathbf{r}$ and time t will propagate through the interacting system, until it is annihilated at point $\mathbf{r}'$ and a later time t'. Therefore, the Green's function is also known as propagator. Alternatively, the single-particle Green's function can be defined in reciprocal space as

$$G(\mathbf{k}, t, \mathbf{k}', t') = -i \langle N|\, \hat{T}\{c_{\mathbf{k}'}(t')c^\dagger_{\mathbf{k}}(t)\}\, |N\rangle \,, \tag{2.25}$$

where $\mathbf{k}$ is the wave vector and $c_{\mathbf{k}'}(t')$ and $c^\dagger_{\mathbf{k}}(t)$ are the destruction and creation operators, respectively. Furthermore, the retarded Green's function can be transcribed in terms of arbitrary single-particle eigenstates $\phi_{\mathbf{k}}(\mathbf{r})$ of an unperturbed single-particle Hamiltonian $H_0(\mathbf{r}) = \sum_i \left[(-\frac{1}{2}\nabla_i^2) + V_n(\mathbf{r}_i) \right]$. In this case, the propagator corresponding to $t' > t$ describes the probability amplitude that if at time t an electron in the state $\phi_{\mathbf{k}}(\mathbf{r})$ is added to the interacting system in its ground state, then at time t' the system will be in its ground state with added electron in the state $\phi_{\mathbf{k}'}(\mathbf{r})$. To be able to extract the energies from this quantity it has to be Fourier transformed, leading to the Lehman (spectral) representation of Green's function [27].Using the completeness relation for the eigenstates, the single-particle propagator can be written as:

$$G(\mathbf{r}, \mathbf{r}', \omega) = \lim_{\eta \to 0^+} \sum_s \psi_s(\mathbf{r})\psi_s^*(\mathbf{r}) \times \left[\frac{\Theta_{\varepsilon - E_F}}{\omega - (\varepsilon_s - i\eta)} - \frac{\Theta_{E_F - \varepsilon}}{\omega - (\varepsilon_s + i\eta)} \right] , \tag{2.26}$$

where $\psi_s(\mathbf{r}) = \langle N | \hat{\psi}(\mathbf{r}) | N+1, s\rangle$, $\langle N+1, s|$ is an eigenstate of the $(N+1)$-particle system and η is a positive infinitesimal such that $\delta \cdot \infty = \infty$. The time ordering is assured by the Heaviside step function $\Theta_x = \begin{cases} 1 & x > 0 \\ 0 & x < 0 \end{cases}$. We note that Green's function is an extremely powerful tool from which one can determine the expectation value of any single-particle operator in the ground state, the ground state energy, momentum distribution, spin and particle density, and one-electron excitation spectrum [32]. Generally, the poles of the single-particle Green's function defined by the equation 2.26 occur at values of ω equal to the difference between the excited state energies of the interacting $(N+1)$-particle system and the ground state energy of the interacting N-particle system. Within the Green's function formalism, the diagonal spectral function $A(\mathbf{r}, \mathbf{r}', \omega) = \frac{1}{\pi} \operatorname{Im} G(\mathbf{r}, \mathbf{r}', \omega) \operatorname{sgn}(E_F - \omega)$ assumes the intuitive form of a many body density of states [99]:

$$A(\mathbf{r}, \mathbf{r}', \omega) = \sum_s \psi_s(\mathbf{r}) \psi_s^*(\mathbf{r}) \delta(\omega - \varepsilon_s). \tag{2.27}$$

The equation of motion of previously described field operators, defined by the equation 2.5, relates the time derivative of $\hat{\psi}(\mathbf{r}, t)$ to the commutator of the field operator and the many-body Hamiltonian [99]: $-i\frac{\partial}{\partial t}\hat{\psi}(\mathbf{r}, t) = \left[\hat{\psi}(\mathbf{r}, t), H\right]$. Using the commutator rules in the Heisenberg picture, one can Fourier transform the equation of motion for the Green's function introduced in equation 2.24 as [40]:

$$\begin{aligned} \Big[\omega - H_0(\mathbf{r}) - V_H(\mathbf{r})\Big] G(\mathbf{r}, \mathbf{r}', \omega) - \\ \int \Sigma(\mathbf{r}, \mathbf{r}'', \omega) G(\mathbf{r}, \mathbf{r}'', \omega) d\mathbf{r}'' = \delta(\mathbf{r} - \mathbf{r}'), \end{aligned} \tag{2.28}$$

where $V_H(\mathbf{r})$ is the Hartree potential previously defined is section 2.1 and $\Sigma(\mathbf{r}, \mathbf{r}'', \omega)$ is the so-called self-energy operator. Using the representation of single-particle propagator from relation 2.26 in 2.28 we obtain the equation of motion in a form that resembles the Kohn-Sham equations:

$$[H_0(\mathbf{r}) - V_H(\mathbf{r})]\, \psi_s(\mathbf{r}, \omega) + \int \Sigma(\mathbf{r}, \mathbf{r}'', \omega) \psi_s(\mathbf{r}'', \omega) d\mathbf{r}'' = E_s \psi_s(\mathbf{r}, \omega). \tag{2.29}$$

Comparing the above relation with the Kohn-Sham equations 2.11, it can noticed that the exchange-correlation potential $V_{xc}[n]$ has been replaced by the non-local self-energy operator $\Sigma(\mathbf{r}, \mathbf{r}'', \omega)$, which mimics the quasiparticle self-interaction [44, 105]. Therefore, instead of solving a problem of many interacting electrons, equation 2.29 transform solves the problem weakly interacting quasiparticles (QP), consisting of a bare additional electron (or hole) introduced in the ground state system screened by the surrounding cloud of other particles [44, 105].

2.3.3. Dyson's equations

Assuming the most simple case of non-interacting particles, the self-energy operator describing the QP self-interaction vanishes [32] and an equation of the non-interacting Green's function becomes apparent:

$$\Big[\omega - H_0(\mathbf{r}) - V_H(\mathbf{r})\Big] G(_0\mathbf{r}, \mathbf{r}', \omega) = \delta(\mathbf{r} - \mathbf{r}'). \tag{2.30}$$

When this expression is plugged back into the equation of motion, it renders the so-called Dyson's equation [32, 40, 105], that links the non-interacting Green's function G_0, to the interacting one G [99]:

$$G = G_0 + G_0 \Sigma G, \tag{2.31}$$

where G_0 is the non-interacting Green's function.

2.3.4. Hedin's equations

After introducing the concept of Green's function and the main equations in the previous sections, we now have to determine an expression for the QP self-energy to be employed in our calculations. Hedin introduced the following set of exact coupled integro-differential equations, where the Green's function and the self-energy operator are expressed in terms of the screened Coulomb interaction [26]:

$$G(1,2) = G_0(1,2) + \int d(3,4) G_0(1,3)\Sigma(3,4)G(4,2), \tag{2.32a}$$

$$\Sigma(1,2) = i \int d(3,4) G(1,4) W(1^+,3)\Gamma(4,2,3), \tag{2.32b}$$

$$W(1,2) = v(1,2) + \int d(3,4) v(1,3) P(3,4) W(4,2), \tag{2.32c}$$

$$P(1,2) = -i \int d(3,4) G(4,2) G(2,3) \Gamma(3,4,1), \tag{2.32d}$$

$$\begin{aligned}\Gamma(1,2,3) = {}& \delta(1,2)\delta(1,3) + \\ & \int d(4,5,6,7) \frac{\partial \Sigma(1,2)}{\partial \delta G(4,5)} G(4,6) G(7,5) \Gamma(6,7,3).\end{aligned} \tag{2.32e}$$

Within the Hedin's formulation, two generic notations have been employed: $i = (\mathbf{r}_i, t_i)$ corresponding to an ensemble of variables consisting of spatial coordinate $\mathbf{r}_i$, time t_i, that is used to describe the i^{th}-particle and $i^+ = (\mathbf{r}_i, t_i + \eta)$ which is a similar set of variables describing the i^{th}-particle at a later time $(t_i + \eta)$. Furthermore, the Hedin's set of equations introduces three new quantities: the screened Coulomb interaction $W(1,2)$ (also referred to as effective interaction), the irreducible polarisability $P(1,2) = \dfrac{\partial n(1)}{\partial V(2)}$

describing the variation of the charge density at a small external perturbation and the vertex function $\Gamma(1,2,3) = \dfrac{\partial G^{-1}(1,2)}{\partial V(3)}$ describing the variation of Green's function upon an external perturbation.

In principle, the QP self-energy can be determined by solving Hedin's equations defined by the expressions 2.32a–2.32e self-consistently [40].

2.3.5. GW approach

In practice, Hedin's functional integro-differential equations are extremely challenging to solve exactly [99]. Consequently, the approach according to which the self-energy response is neglected in the vertex function has been introduced to simplify the theory [40]. Within this approach $\Gamma(1,2,3) = \delta(1,2)\delta(1,3)$ and therefore the Hedin's equations takes the following simplified form:

$$G(1,2) = G_0(1,2) + \int d(3,4) G_0(1,3)\Sigma(3,4)G(4,2), \tag{2.33a}$$

$$\Sigma(1,2) = iG(1,2)W(1^+,2) \tag{2.33b}$$

$$W(1,2) = v(1,2) + \int d(3,4) v(1,3)\chi_0(3,4)W(4,2), \tag{2.33c}$$

$$\chi_0(1,2) = -iG(1,2)G(2,1), \tag{2.33d}$$

$$\Gamma(1,2,3) = \delta(1,2)\delta(1,3). \tag{2.33e}$$

The etymology of the GW formalism derives from the equation 2.33b. The advantage of GW framework is specifically this equation, which can be summarized in reduced form as $\Sigma = iGW$ [99]. We note that the irreducible independent paricle polarizability χ_0 in the absence of the vertex function Γ is known as the Random Phase Approximation (RPA) [106, 107]. The irreducible polarizability determines the frequency-dependent inverse dielectric function $\varepsilon^{-1}(\mathbf{r}, \mathbf{r}', \omega)$ which in turn screens the Coulomb interaction [99].

In principle, the exact way of solving equations 2.33a-2.33e is the full self-consist GW approach (*scGW*). Within this formalism, the GW quantities are computed iteratively, until the interacting Green's function from Dyson equation 2.33a is converged up to a predefined threshold value. In practice, the use of *scGW* approach is hampered by its extreme computational demands and some ongoing conceptual debates [99].

2.3.6. G_0W_0 approximation and beyond

The most common GW approximation is called G_0W_0 approximation, in which the single-particle Green's function G_0 is computed directly from the first iteration of Dyson's equation, starting from the Kohn-Sham eigenvalues ϵ_n and eigenfunctions $\phi_n(\mathbf{r})$ [99]:

$$G_0(\mathbf{r},\mathbf{r}',\omega) = \sum_n \frac{\phi_n(\mathbf{r})\phi_n^*(\mathbf{r}')}{\omega - \epsilon_n - i\eta\,\mathrm{sgn}(\epsilon_n - E_F)}. \tag{2.34}$$

We note that in equation 2.34, as well as in the following derivations, the spin dependence have been omitted for clarity. The equation 2.34 is subsequently used to compute the screened Coulomb interaction within RPA W_0 and the self-energy $\Sigma_0 = iG_0W_0$.

The Dyson's equation 2.31 can be written in terms of Kohn-Sham single-particle wave functions as

$$[H_0(\mathbf{r}) - V_H(\mathbf{r})]\,\phi_n(\mathbf{r}) + \int \Sigma_0(\mathbf{r},\mathbf{r}',E_n)\phi_n(\mathbf{r}')d\mathbf{r}' = E_n\phi_n(\mathbf{r}). \tag{2.35}$$

Comparing equations 2.35 and 2.11, it can be noticed that the Kohn-Sham Hamiltonian is similar with QP Hamiltonian, apart from the replacement of the exchange-correlation potential V_{xc} with the self-energy operator $\Sigma(E_n)$. Considering $(\Sigma(E_n) - V_{xc})$ as a first-order perturbation to the Kohn-Sham Hamiltonian [42, 44], one can rewrite the previous expression as [32, 105]:

$$E_n = \epsilon_n + Z(\epsilon_n)\,\langle\phi_n|\,\Sigma_0(\epsilon_n) - V_{xc}\,|\phi_n\rangle\,, \tag{2.36}$$

where the QP renormalization factor $Z(\epsilon_n) = \left(1 - \frac{\partial\Sigma}{\partial\omega}\Big|_{\omega=\epsilon_n}\right)^{-1}$ results from the approximation of the self-energy operator with the first term of a Taylor expansion around the Kohn-Sham eigenvalues ϵ_n. We note that all the QP energies reported throughout this thesis are computed using the expression 2.36.

The main problem of the G_0W_0 approximation is represented by its pronounced dependence on the Kohn-Sham eigenvalues and eigenstates used as starting point [108–111]. The strong starting point dependence of G_0W_0 approximation, by more than 2 eV for band gaps in solids [108], is caused by the underscreening which by being inverse proportional to the eigenvalue gap ϵ_n is in turn impacted by the band gap underestimation at DFT level. To mitigate this issue, other approximations that go beyond the one-shot G_0W_0 framework have been developed by including some level of self-consistency in Hedin's GW equations [99].

One such approximate self-consistent approach is to update only the single-particle eigenvalues and is referred to as *evGW*. Within this framework, the real part of the QP energies computed in the first G_0W_0 step from equation 2.36 are reintroduced in the Green's function expression 2.34 in the place of the Kohn-Sham eigenvalues ϵ_n. This procedure is applied until the input quantities equal the output ones [99]. We note that, despite the partial self-consistency, the dependence of the starting point is not totally eliminated, mainly because the QP wave functions are not iterated self-consistently [112].

Based solely on band gaps of molecular systems, $evGW$ have been proved to perform better than G_0W_0 leading to band gaps in good agreement with the experimental values [113, 114]. However, the overall $evGW$ QP spectra are different from the experimental ones, especially at lower energies [112]. Furthermore, $evGW$ significantly overestimates the band gaps in solids [115]. Another approximate self-consistent scheme is the so-called quasiparticle self-consistent GW ($QSGW$) where the QP eigenvalues and eigenfunctions used to create Green's function are updated from the variationally best mean-field potential to a given self-energy [99]. Several studies [116–119] reported that $QSGW$ performs better than G_0W_0 leading to more accurate band gaps.

Finally, we return to the fully self-consistent formalism discussed in the previous section. Due to its extensive memory and computation requirements the $scGW$ approach has been implemented only for finite systems such as 3D and 2D homogeneous electron gas [120, 121], very simple semiconductors [122, 123], atoms [124] and small molecules [112, 125–127]. While for finite systems $scGW$ improves the accuracy of the first ionization energies with respect to G_0W_0 [128], when analysing the entire spectrum it is usually outperformed by G_0W_0 approximation if a suitable starting point is employed [112, 119, 127]. Furthermore, $scGW$ approach is known to severely overestimates the band gap energies of simple semiconductors [99].

Although appealing due to its generally outstanding performance, even the simplest G_0W_0 approximation poses great technical challenges. For example performing GW calculations for core levels is notoriously difficult due to increased sensitivity of core states to the local environment [2, 99]. Taking into account spin dependence in GW calculation is another complication that is crucial for electronic structure of topological insulators and materials containing heavy atoms, highly influenced by the inclusion of SOC [99]. Recently, Aryasetiawan et al. introduced a generalization of Hedin's equations to allow the description spin-dependent interactions between particles [129, 130].

2.4. Bethe-Salpeter equation

The Green's function formalism is an extremely powerful framework that allows not only the calculation of particle addition and removal energies but also the analysis of optical properties such as photon absorption. To describe the optical properties, the two-particle correlated electron-hole amplitude L (also known as four-point polarizability) is needed [26]:

$$L(1,2;1',2') = -G_2(1,2;1',2') + G(1,1')G(2,2'), \tag{2.37}$$

where G_2 is the two-particle Green's function. Expressing the two-particle correlation function in terms of one-particle Green's function and its functional derivative with respect to the local potential, a Dyson-like equation is obtained for L [43]:

$$\begin{aligned} L(1,2;1',2') &= L_0(1,2;1',2')+ \\ &\int d(3,4,5,6) L_0(1,4;1',3) \frac{\delta\left[v(3)\delta(3,4)+\Sigma(3,4)\right]}{\delta G(5,6)} L(5,2;6,2'), \end{aligned} \tag{2.38}$$

where $L_0 = G(1,2')G(2,1')$. We further introduce the kernel functional defined as

$$K(3,5;4,6) = \frac{\delta\left[v(3)\delta(3,4)+\Sigma(3,4)\right]}{\delta G(5,6)}, \tag{2.39}$$

and representing an effective two-particle interaction. Introducing the expression of K into the Dyson-like equation 2.38, one get the Bethe-Salpeter equation (BSE):

$$\begin{aligned} L(1,2;1',2') &= G(1,2')G(2,1')+ \\ &\int d(3,4,5,6) L_0(1,4;1',3) K(3,5;4,6) L(5,2;6,2'). \end{aligned} \tag{2.40}$$

For studying the optical absorption process is sufficient to know the reducible polarizability $\tilde{P}(1,2) = -iL(1,2;1',2')$. However, since there is no known exact expression for the reducible polarizability, the BSE should be solved and then L function should be contracted into two-point polarizability.

To mitigate the difficulty in solving BSE, lying in the calculation of kernel function K, several approximations have been developed. Within the time-dependent Hartree approximation the the self-energy Σ is completely neglected and BSE reduces to a Dyson-like equation for irreducible polarizability defined in equation 2.32d:

$$P(1,2) = P_0(1,2) + \int d(3,4) P_0(1,3) v(3,4) P(4,2). \tag{2.41}$$

We note that this approximation is equivalent with RPA [106, 107]. Another approximation for the kernel function is time-dependent Hartree-Fock approximation in which $\Sigma(1,2) = iG(1,2)v(1^+,2)$. However, in practice this approximation is not valid because the attraction between the electrons and holes described by $v(1^+,2)$ is unphysically large due to the unscreened Coulomb interaction.

The most common approximation is the time-dependent screened Hartree-Fock, also known as GW+BSE due to its core assumption:

$$\Sigma(1,2) = iG(1,2)W(\mathbf{r}_1,\mathbf{r}_2,\omega=0). \tag{2.42}$$

In practical applications GW+BSE is solved in a product basis of occupied $\langle v\mathbf{k}|$ and unoccupied $\langle c\mathbf{k}|$ states, for a specific excited state S and using the QP energies [29]:

$$(E^{QP}_{c\boldsymbol{k}} - E^{QP}_{v\boldsymbol{k}}) A^S_{vc\boldsymbol{k}} + \sum_{v'c'\boldsymbol{k'}} \langle vc\boldsymbol{k}| K |v'c'\boldsymbol{k'}\rangle = \Omega^S A^S_{vc\boldsymbol{k}}, \tag{2.43}$$

where $A^S_{vc\boldsymbol{k}}$ are the coefficients of the exciton wave function written in the free electron and hole basis $|vc\boldsymbol{k}\rangle$, Ω^S is the excitation energy. The equation 2.43 is solved within the Tamm-Dancoff approximation (TDA)[45], which ignores backward propagating electron-hole pairs that are present in the exact BSE and assumes that the kernel consists of a direct screened interaction and repulsive exchange term [99].

When GW+BSE first emerged in literature the research focused on describing the excited state optical properties of simple semiconductors such as Si, GaAs and Li_2O and proved that optical absorption spectra and exciton binding energies obtained from BSE are in very good agreement with experiment [29, 131–133]. Recently, GW+BSE started to be extensively used for molecules [134–136] and complex 2D [137–142] and 3D [143–149] solids.

Chapter 3

Electronic properties of metal-halide perovskites

The mineral perovskite calcium titanium oxide ($CaTiO_3$) was initially discovered in 1839 by the German mineralogist Gustav Rose [150]. Since the first crystallographic study describing its crystal structure conducted in 1926 by Victor Goldschmidt [151], the meaning of 'perovskite' label has changed and now the term designates the class of materials with crystalline structure similar to that of $CaTiO_3$. The perovskite structure is one of the most abundant in nature, magnesium silicate perovskite ($MgSiO_3$) being the main mineral found in the earth's mantle [152, 153].

These materials are described by the generic chemical formula ABX_3, where A and B are cations of different sizes bounded by the X anion and can be classified based on the nature of the anion in two main categories, i.e. oxide and halide perovskites [154]. The oxide perovskites have been extensively examined since 1956 and soon after a breakthrough report proving the ferroelectricity of these materials [155] marked the beginning of numerous experimental and theoretical studies exploring their favorable optoelectronic properties for light-conversion applications [156–165]. Unlike their oxide analogues, the interest in halide perovskites has surge not earlier than in the last two decades. Despite their late disclosure, recently the number of studies has grown exponentially and revolutionized the knowledge on semiconductor materials. The extensive research on halide perovskites proved their exceptionally optoelectronic properties and revealed suitable candidates for photovoltaic applications such as solar cells, light-emitting devices, scintillators and many more [166–172].

This thesis focuses on metal-halide perovskites solely and analyses in detail the structural, electronic and optical properties of some archetypal examples, as well as the changes induced by modifications of traditional perovskite structure.

3.1. Chemical and structural diversity in metal-halide perovskites

Figure 3.1 shows a schematic representation of the ideal cubic structure of a metal-halide perovskite with the stoichiometric formula $AB^{II}X_3$, where A^{+1} is an atomic or molecular cation, B^{II} is a divalent metal and X^{-1} is a halide anion (F^-, Cl^-, Br^- or I^-). The metallic cation B^{II} is coordinated with six X^{-1} halide ions, forming a highly flexible framework constructed of corner-sharing metal-centered octahedra. The A^{+1} cations occupy the cuboctahedral cavities of this network. Thus, the cubic structure, belonging to the $Pm\bar{3}m$ space group, features octahedral symmetry [173–175]. In the following, the cubic perovskite phase will be referred to as an undistorted and untilted structure.

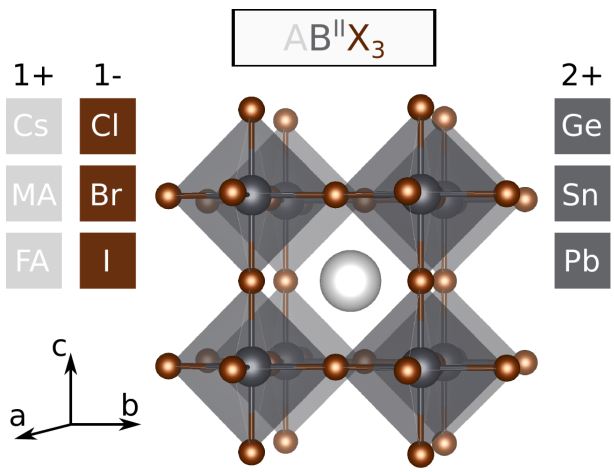

Figure 3.1: Schematic representation of cubic structure metal-halide perovskite.

The crystalline lattice of experimentally synthesised metal-halide perovskites is significantly distorted with respect to the ideal cubic structure [176]. These various distortions can be inflicted by displacement of A or B^{II} cation, leading to ferroelectric and antiferroelectric effects, or by octahedral tilting, leading to potential changes of the unit cell size and symmetry [173–175, 177]. In practice, the majority of the experimentally achievable structures exhibit both octahedral tilting and cation displacements [178].

Furthermore, the crystalline lattice of metal-halide perovskites is also impacted by the size of the component chemical elements, that can lead to 3D, 2D and even 1D compounds. The dimensionality of the perovskite structure is described by the tolerance factor. This empirical concept was introduced by Goldschmidt in Ref. [151] as

$$t = \frac{R_A + R_X}{\sqrt{2}(R_{B^{\mathrm{II}}} + R_X)}, \tag{3.1}$$

where R_A, $R_{B^{\mathrm{II}}}$ and R_X are the ionic radii of the elements in $AB^{\mathrm{II}}X_3$ metal-halide perovskites. The close-packed cubic structure is achieved when both A and $\mathrm{B^{II}}$ ions have ideal size, yielding a tolerance factor that ranges between 0.9 and 1.0 [151, 154, 179, 180]. However, a tolerance factor as low as 0.71, corresponding to the case when A ions are smaller and the $B^{\mathrm{II}}X_6$ octahedra tilt to fill the space, still ensure a perovskite crystal structure although distorted into orthorhombic symmetry [181, 182]. The compounds in which A and $\mathrm{B^{II}}$ cations have similar ions radii, leading to a tolerance factor lower than 0.71, tend to collapse into a 1D needle-like (ilmenite) structures. In contrast, the compounds featuring a mismatch between the ionic radii of the chemical elements (A ion too large or $\mathrm{B^{II}}$ ion too small) distort in stable hexagonal variants [183] or even form 2D analogues of the perovskite structure [184]. This classification illustrates the great diversity of metal-halide perovskites, ranging from conventional undistorted 3D to 1D systems, that can accommodate ions with very different sizes as long as they satisfy the global charge balance within the resulting compound.

One of the most studied class of materials is represented by the Pb-based hybrid organic-inorganic halide perovskites, where A is a molecular cation and $\mathrm{B^{II}}$ metal site is occupied by lead. Their exceptional photophysical properties render them to be optimal candidates for various optoelectronic applications, ranging from solar cells with power conversion efficiencies exceeding 28%[7, 8], to light-emitting diodes (LEDs) [185, 186] and radiation detectors [187, 188]. An example of such compound is the prototypical methylammonium lead iodide perovskite ($\mathrm{MAPbI_3}$) which was firstly reported as an absorber layer in a solar cell device by Kojima et al. in Ref. [170]. Hybrid Pb-halide perovskites feature outstanding properties such as suitable band gap and low trap-state densities [10, 11]. Recently, the all-inorganic Pb-based halide perovskites have also come into focus due to their improved stability [189] and have been successfully used in LEDs [190] and high photoluminescence quantum yields of colloidal crystals and quantum dots [191, 192]. However, similar to their hybrid organic-inorganic derivatives, strong electric fields tend to quickly degrade all-inorganic Pb-based perovskites [193]. Furthermore, ion segregation usually present in Pb-base halide perovskite leads to band gap instability [194]. Both hybrid and all-inorganic Pb-halide perovskites are easy to process from solutions forming soft structures prone to point defects. This local inhomogeneities negatively impact the structure, leading to increased instability against moisture, heat and light exposure [12].

In the effort to mitigate the stability issues of Pb-based 3D metal-halide perovskites [13], the interest in lower dimensional derivatives is currently on the rise . Dimensional reduction is one of the most used techniques to manipulate solid structures and introduce new functionalities by creating lower dimensional analogues [195]. Dimensional reduction of inorganic sublattice in hybrid organic–inorganic perovskites, achieved by incorporation of large organic molecules such as butylammonium (BA) or phenylethylammonium (PEA), leads to new materials that combine the exceptional optoelectronic properties of the 3D counterparts with improved structural stability. These lower-dimensional derivatives feature additional structural heterogeneity due to the symmetry breaking along the long axis of the organic molecules. One emerging class of such compounds is the family of two-dimensional (2D) Ruddlesden-Popper (RP) perovskites, with general chemical formula $A'_{n-1}A_2B_nX_{3n+1}$[196–201]. In hybrid organic-inorganic RP perovskites, A' is an aliphatic or aromatic alkylammonium cation separating the n-layer perovskite framework – a 2D network of corner-sharing BX_6 ($B=Pb^{+}2$, $X=I^-$, Br^-) octahedra with small monovalent organic cations A ($A=CH_3NH_3^+$, Cs^+). Generally, the perovskite slabs correspond to slices taken along the (001) lattice plane of the 3D perovskite and the dimensionality of this inorganic frame can vary from $n \to \infty$ representing the limit of 3D perovskite down to $n = 1$, representing a single monolayer. Figure 3.2 shows a schematically representation of a 2D RP perovskite.

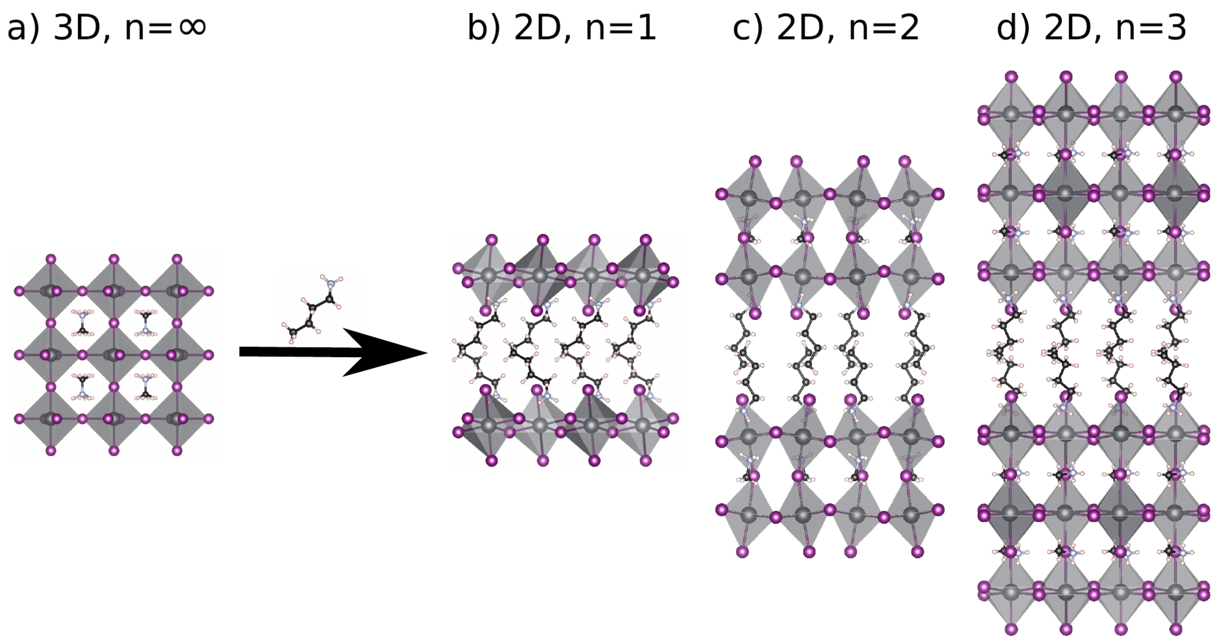

Figure 3.2: Schematic representation of the process of dimensional reduction via incorporation of BA long organic molecule into a) 3D $MAPbI_3$ bulk, resulting $(BA)_n(MA)_{n-1}Pb_nI_{3n+1}$ 2D RP hybrid organic-inorganic Pb-halide perovskites with b) $n = 1$, c) $n = 2$ and d) $n = 3$ inorganic layer thickness.

The 2D RP perovskites occupy a leading place among the intensively studied materials, due to their exceptionally optoelectronic properties such as tunable band gaps, high defect tolerance, long carrier lifetimes and high photoluminescence (PL) quantum efficiency [202–205], and improved structural stability towards moisture achieved by the hydrophobic organic molecules at the surface [196, 206, 207]. These materials feature natural multiple-quantum-well structures, in which the quantum wells are represented by the inorganic slabs, while the potential barriers are represented by the long organic linkers [208, 209]. Their relatively easy synthetic processing via mechanical exfoliation [210], solution processing [211] or colloidal engineering [212] methods renders the 2D RP hybrid perovskites as promising absorbers for photovoltaic applications [14].

Besides the instability of Pb-based halide perovskites under ambient conditions, these materials also pose questions of environmental safety, being considered hazardous because of the lead toxicity [213–215]. These drawbacks have prevented for years the large-scale commercialization of one of the most common application, namely perovskite-based solar cells, and driven the research to find new Pb-free metal-halide perovskites with similar desirable optoelectronic properties.

The straightforward approach to design Pb-free metal-halide perovskites, is the homovalent substitution of lead with isovalent cations from group-14 elements such as Ge^{2+} and Sn^{2+}. Although having good optoelectronic properties, they are not stable and easily oxidize to the oxidation state +4, leading to a rapid degradation of the halide perovskite [187, 216–218]. Furthermore, studies on ecotoxicity of halide perovskites showed that Sn may not fully solve the health hazards of Pb-based solar cells [214]. Furthermore, as showed in previous high-throughput computational studies [23, 219], they are also likely to negatively impact the electronic properties by decreasing the band gaps and increasing the effective masses. Another viable approach is the heterovalent substitution of Pb with a combination of different mono- and trivalent metals cations, resulting in a chemical heterogeneity consistently repeated throughout the entire crystal lattice. This process, schematically represented in Figure 3.3, gives rise to the double halide perovskites (elpasolites) class of materials, with the general formula $A_2B^IB^{III}X_6$ [220]. Even though these compounds have been known since the 1880s and crystallographically characterized since the 1930s, they saw a surge in interest much later, with the emergence of high throughput scanning studies such as the one in Ref. [15].

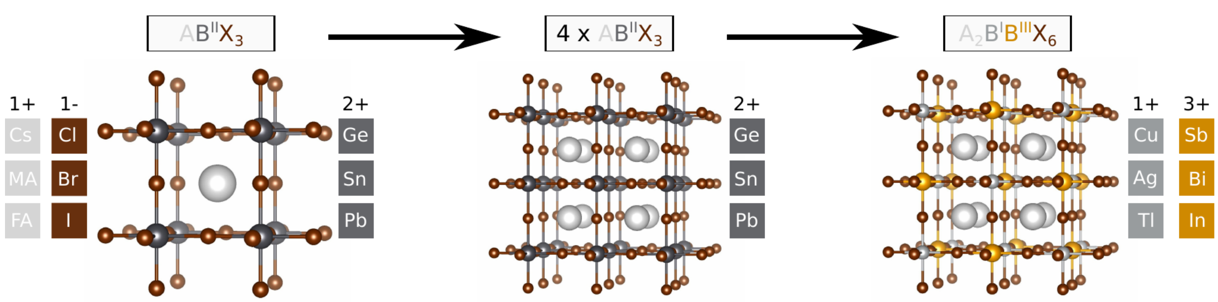

Figure 3.3: Schematic representation of the process of theoretical doubling the unit cell of a metal-halide perovskite.

Double perovkites crystallize in a 3D rock-salt ordered cubic structure, in which octahedrally coordinated B^{I} and B^{III} metal cations occupy alternating lattice sites and have an average nominal oxidation state allowing for the incorporation of metals with oxidation states from +1 to +4 [15, 221]. This tremendous chemical diversity hints to the possibility of obtaining a wide range of thermodynamically stable materials [222, 223]. Recently, the interest in double perovskites has been on the rise due to their considerable structural and electronic variety [221] and improved stability in terms of heat and moisture under ambient conditions, compared to lead-based halide perovskites [224–226]. Many of the possible candidates have been synthesized and studied as potential solar absorbers [227–230], X-ray detectors [230], and scintillators [231].

3.2. Pb-based Ruddlesden-Popper hybrid perovskites

The optical properties of 2D RP perovskites are governed by dielectric and quantum confinement [202, 232–237], which has been shown experimentally [210, 234] and by means of first principles and semiempirical electronic structure calculations [238, 239]. In contrast, much less is known about the effects of dimensional reduction and the A-site cation on the electronic properties of these materials. Ultraviolet (UV) and inverse photoemission spectroscopy combined with density functional theory (DFT) calculations have been reported for BA_2PbI_4 and BA_2PbBr_4, showing less band dispersion and a larger density of states (DOS) at the band edges than in their 3D counterparts [240]. DFT calculations by Gebhardt et al. [199] showed that the electronic structure of the layered bulk phase of PEA_2PbI_4 is almost unaffected by reducing the dimensionality to a monolayer, suggesting weak interactions between the molecular and perovskite sublattices along the stacking direction. Furthermore, the interaction between these sublattices was shown to be governed by steric effects in a study by Du et al. [241].

In this section we analyse the effect of dimensional reduction and the interplay between the metal-halide and molecular contributions governing the electronic properties of 2D RP Pb-based perovskites. To elucidate the effects of A-site organic cation to the electronic structure, we study the 3D prototype $CH_3NH_3PbI_3$ ($MAPbI_3$) and the hybrid organic-inorganic 2D perovkites A_2PbI_4, with A = $C_4H_{12}N$ (BA), $C_8H_{12}N$ (PEA). By comparing the computed density of states (DOS) with the experimentally obtained one via ultraviolet photoelectron spectroscopy (UPS), we reveal the electronic and structural contributions of the molecular and perovskite sublattices.

3.2.1. Crystal structures

Figure 3.4 a) and b) shows the crystal structure of the 2D RP perovskites BA_2PbI_4 and PEA_2PbI_4 as obtained from X-ray diffraction experiments under ambient conditions and reported in Ref. [242] and [241], respectively.

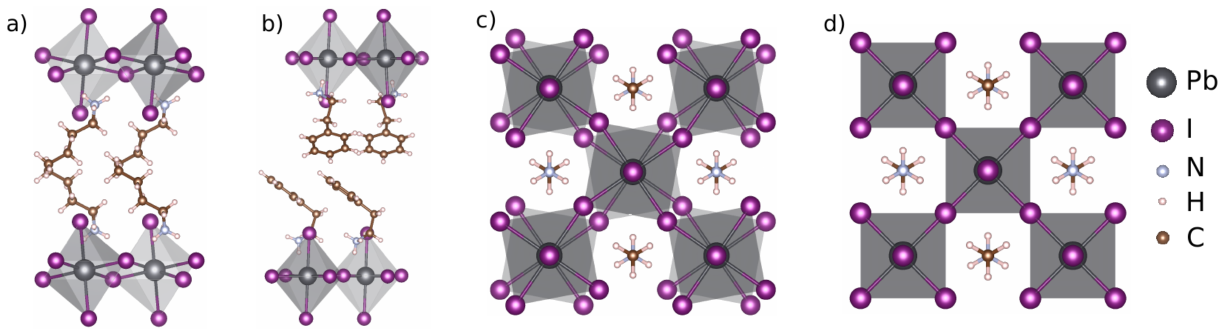

Figure 3.4: Schematic representation of the crystal structures of a) $Pbca$ phase of BA_2PbI_4, b) $P-1$ phase of PEA_2PbI_4, c) $I4/mcm$ phase of $MAPbI_3$ and d) $Pm\bar{3}m$ phase of $MAPbI_3$.

BA_2PbI_4 is orthorhombic with $Pbca$ symmetry at room temperature (RT). The perovskite layers consisting of halide octahedra with Pb centers are separated along the stacking direction by long organic BA molecules, resulting in a longer out-of-plane lattice parameter $c = 26.23\,\text{Å}$, and non-equal in-plane lattice parameters $a = 8.43\,\text{Å}$ and $b = 8.99\,\text{Å}$. PEA_2PbI_4, a more stable RP perovskite due to the longer PEA cation, is triclinic with $P-1$ symmetry, with in-plane lattice parameters $a = b = 8.74\,\text{Å}$ and an out-of-plane lattice parameter of $c = 32.99\,\text{Å}$. Contrary to its 2D RP counterparts, $MAPbI_3$ is known to occur in tetragonal phase, with $I4/mcm$ symmetry, at room temperature (RT) and undergo a phase transition at $T = 327\,\text{K}$. The crystal structure consists of a 3D lattice of corner sharing PbI_6 octahedra, with MA molecules in between. The high-temperature cubic ($Pm\bar{3}m$) and room-temperature tetragonal ($I4/mcm$) phases are shown in Figure 3.4 c) and d). All structural parameters are listed in Table 3.1.

3.2.2. Experimentally determined structures

Figure 3.5 shows the valence band maximum (VBM) region of 2D BA_2PbI_4 and PEA_2PbI_4 and 3D $MAPbI_3$ obtained from ultraviolet photoelectron spectroscopy (UPS), as well as the first principles DOS, calculated using DFT with the PBE [67] exchange-correlation functional. The UPS spectra presented in panel a) were achieved by our collaborators in the Department of Macromolecular Chemistry I at the University of Bayreuth. The comparison between our computed DOS and the experimental UPS spectra is known to be notoriously complicated by several factors. First, while the highest occupied molecular orbital eigenvalue should be equal to minus the ionization potential in exact Kohn-Sham DFT, it is generally overestimated by up to 2 eV by the standard semilocal approximations like PBE. Second, the calculated DOS is typically compressed with respect to experiment [243]. We therefore follow the approach by Tao et al. [244] in order to improve the agreement with the UPS measurements and stretch our calculated DOS by $\sim 2.6\,\%$. To match the onset and intensity of the experimentally determined spectra, the calculated

Table 3.1: Lattice parameters (a, b, c in Å and α, β, π in °), unit-cell volume per formula unit (Ω) in Å^3, octaheron volume (ω) in Å^3 and average Pb–I bond lengths for experimental structures of tetragonal $MAPbI_3$, BA_2PbI_4 and PEA_2PbI_4 as reported in Ref.[241, 242].

	$MAPbI_3$	**BA_2PbI_4**	**PEA_2PbI_4**
a (Å)	8.97	8.43	8.74
b (Å)	8.97	8.99	8.74
c (Å)	12.68	26.23	32.99
$\boldsymbol{\alpha}$(°)	90.00	90.00	84.65
$\boldsymbol{\beta}$(°)	90.00	90.00	84.66
$\boldsymbol{\pi}$(°)	90.00	90.00	89.64
$\boldsymbol{\Omega}$(Å^3)	254.84	496.68	624.57
$\boldsymbol{\omega}$(Å^3)	43.92	42.12	42.27
d^{ax}_{Pb-I}(Å)	3.17	3.17	3.22
d^{eq}_{Pb-I}(Å)	3.22	3.195	3.175

DOS are red-shifted and multiplied by a normalization factor.

As shown in right panel of Figure 3.5, the electronic states in the vicinity of the VBM remain unaffected by the A-site cation change due to their p-orbital character originating from the inorganic PbI_4 sublattice – a general trend of the Pb-based perovskites. In agreement with previous reports [245–248], the DFT calculations show that the VBM of all three systems consists of mainly I p with some Pb s orbital contributions, as depicted in Figure 3.6. Furthermore, a closer look at the orbital character of the electronic structure reveals a significantly larger contribution from the orbitals lying in the perovskite plane. However, at the onset of the DOS, the 3D $MAPbI_3$ is utterly different from the 2D RP perovskites. The VBM of $MAPbI_3$ is dictated by the equatorial halides, whereas in the case of the 2D perovskites BA_2PbI_4 and PEA_2PbI_4 the VBM is derived primarily from the axial ones.

Apart from the region close to the VBM, the overall electronic structure differs significantly across the three studied compounds. These differences are driven by the organic cation through direct and indirect effects. To probe the former, we analyse the global shape of both experimentally-determined and computed DOS and find that the electronic states localized on the molecular linkers dominate the electronic DOS at different energies. Moreover, by replacing BA molecules with PEA, the strong feature originating from the organic cation splits into two components and approaches the Fermi level. To explain this difference, we calculate the energies of highest occupied and lowest unoccupied molecular orbitals (HOMO and LUMO) of all organic linkers and show in Table 3.2 that the states dictated by the organic cations depend on the HOMO-LUMO gap of the free-standing molecule. PEA has the smallest HOMO-LUMO gap, therefore PEA-based states

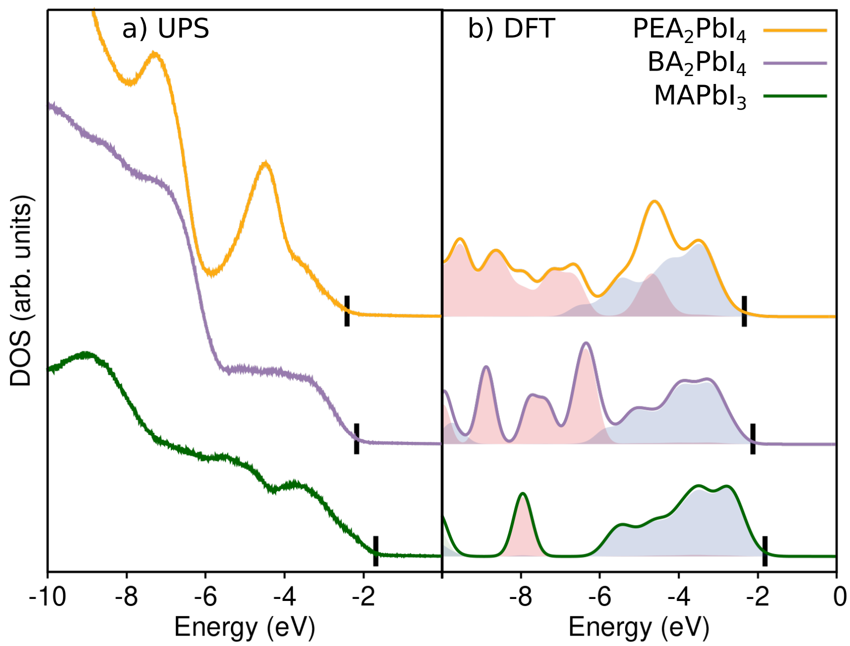

Figure 3.5: Total density of states (DOS) of valence band region as determined from a) ultraviolet photoelectron spectra (UPS) and b) PBE+SOC DFT calculations, for 3D $MAPbI_3$ (green), 2D BA_2PbI_4 (purple) and PEA_2PbI_4 (yellow), scaled with respect to the Fermi energy level. The black dash marks the valence band onset. The shaded areas in the computed DOS represent the projections onto molecular orbitals, as following: blue – states originating from the inorganic perovskite backbone, red – states originating from the organic molecules.

are found at energies relatively close to the band edges. Furthermore, the magnitude of interaction between the organic and inorganic sublattices is computed as the difference between the total energy of 2D perovskites and the sublattices energy. BA interacts more strongly with the PbI_2 monolayer, having a slightly larger interaction energy than the similar 2D perovskite PEA_2PbI_4. Notably, this interaction energy difference neither results in significant structural distortions nor seems to drastically influence the electronic structure of the corresponding perovskites at RT. This observation is supported by the computed total DOS represented in Figure 3.8 a), that show only minor changes in the spectral shape near the onset of the VBM.

The indirect effects of the organic cations are a consequence of the different structural distortions of the Pb-I cage induced by the molecules. These distortions influence the occupied DOS around the VBM and determine the position of the onset in the UPS spectra. The 2D RP perovskites feature an off-center displacement of the Pb ions in the PbI_6 octahedra, leading to alternating short and long $Pb - I$ equatorial bond lengths. Comparing the 3D $MAPbI_3$ with the 2D RP PEA_2PbI_4 perovskite, the latter feature distorted octahedra, with alternating tilt angles in the perovskite layer. Furthermore,

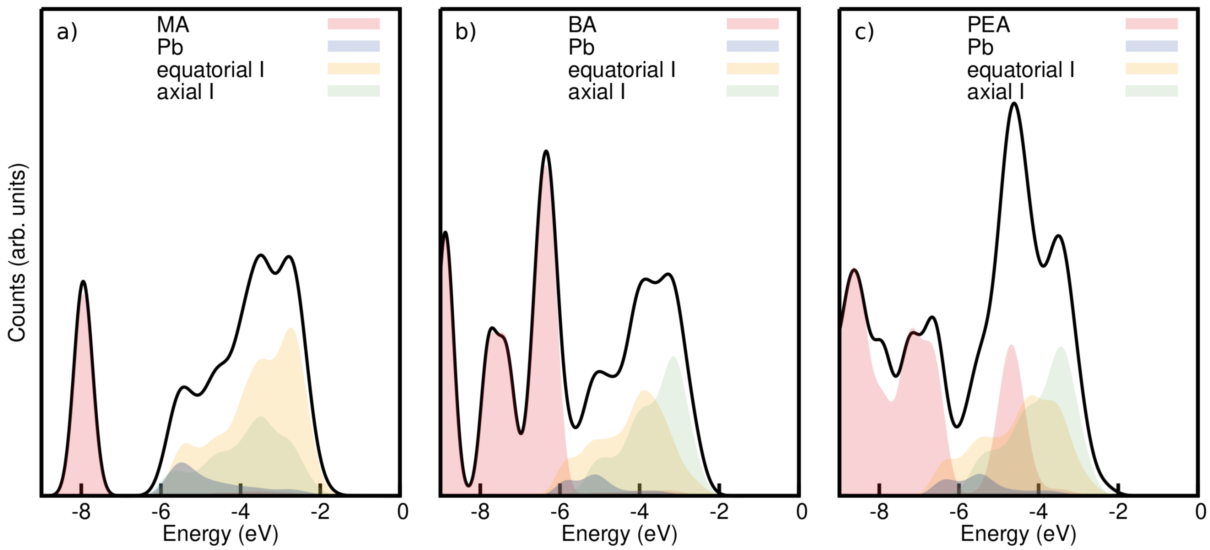

Figure 3.6: Computed PBE+SOC DOS spectra (of the valence band region) for experimentally determined structures of a) $MAPbI_3$; b) BA_2PbI_4 and c) PEA_2PbI_4. Individual projections of the constituents are represented in colors as follows: contributions from organic cation in red, contributions from Pb in blue, contributions from equatorial I in orange and contributions from axial I in green.

as shown in Figure 3.7 c), the PbI_6 octahedra are compressed in the perovskite plane and elongated along the stacking direction, yielding an axial Pb–I bond length of 3.22 Å. Figure 3.7 b) demonstrates that the more flexible (and small) BA molecule induces greater structural distortions than PEA and therefore leads to a significantly different DOS.

3.2.3. Theoretically designed model structures

To discriminate between the effects of structural distortions represented in Figure 3.7 and those of various organic molecules, we constructed a set of model monolayer systems, by replacing the organic cation with Cs, with the distortions found in the experimental structures. In the following these monolayer model systems are referred to as MA-, BA- and PEA-like distorted systems depending on the inherited distortions. A detailed description of the monolayer model systems can be found in section A.2.3 of the Appendix.

Figure 3.8 a) shows a comparison between the DOS of these distorted systems and the one of an undistorted model system with untilted and undistorted metal-halide octahedra as found on average in the 3D cubic phase of $MAPbI_3$, that highlight the large effect of the Pb-I cage distortions in the 2D RP BA_2PbI_4 perovskite on the onset of the spectrum. Moreover, although featuring a very similar overall shape, the DOS of the model systems with MA- and PEA-like distortions are different at the onset. To quantify this difference, we integrate the DOS up to $E = k_BT(\sim 30\,\text{meV})$ below the VBM for both

Table 3.2: Computed band edge energies, HOMO-LUMO gaps of organic cations MA^+, BA^+ and PEA^+, energy gap (E_{gap}) between the molecular states in the band structure and the interaction energy (E_{inter}) of $MAPbI_3$, BA_2PbI_4 and PEA_2PbI_4.

	MA$^+$	**BA$^+$**	**PEA$^+$**
HOMO (eV)	-15.74	-11.56	-9.94
LUMO (eV)	-6.29	-5.79	-5.37
HOMO-LUMO gap (eV)	9.45	5.77	4.57
E_{gap} (eV)	8.77	7.50	4.47
E_{inter} (meV/atom)	-40.05	-27.43	-18.25

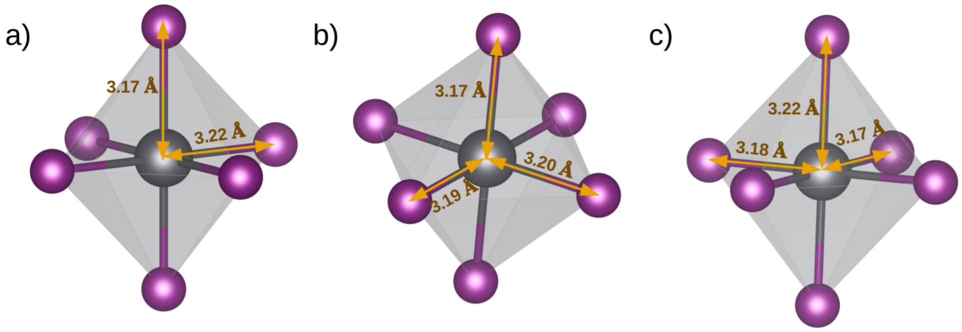

Figure 3.7: PbI_6 octahedron of a) 3D $MAPbI_3$, 2D RP b) BA_2PbI_4, c) PEA_2PbI_4. Yellow arrows mark $Pb-I$ bond lengths along the two in-plane directions (equatorial), as well as perpendicular to those (axial) and are accompanied by the corresponding values.

the experimental structures and the model systems. As shown in Figure 3.8 b), there is a stark dependence on the dimensionality, indicating a lower electronic conductivity for the 2D RP BA_2PbI_4 and PEA_2PbI_4 perovskites, in agreement with previous reports [246, 249]. Furthermore, the integrated DOS is correlated with the octahedron volume such that smaller volumes lead to larger distortions, yielding fewer states within the analysed energy range. Moreover, the trend is similar for both the experimentally-determined structures and monolayer model systems.

In summary, our first principles calculations demonstrated that while the direct contributions of the A-site cation on the total DOS are localized deep in the valence band region, the magnitude of the DOS close to the Fermi level, is related to structural distortions of the perovskite sublattice, which are due to steric interactions between the two sublattices.

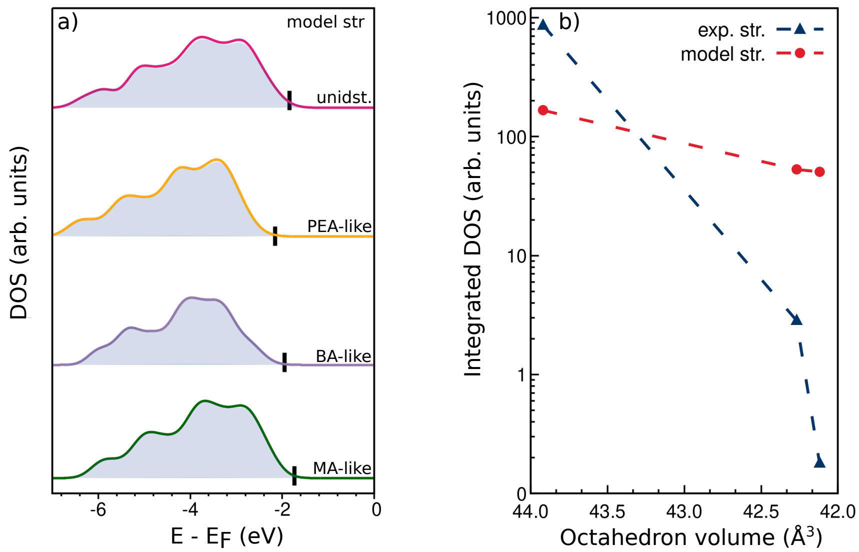

Figure 3.8: a) Computed PBE+SOC total DOS for distorted systems featuring MA-like (green), BA-like (purple) and PEA-like (yellow) distortions, as well as for the undistorted model system (magenta), scaled with respect to the Fermi energy level. b) Integrated DOS for all experimental and model systems from VBM (as computed with PBE+SOC) down to 30 meV below.

3.3. Computational screening of Pb-free double perovskites

With the aim to find new Pb-free compounds with promising electronic properties, in this section we scan a relatively wide range of double metal-halide perovskites by modifying both metal cations and halogen anions. We study how chemical composition impacts the electronic band structure and fundamental band gap of these materials, by performing first principles DFT calculations within the PBE approximation and including the effect of spin-orbin coupling (SOC) self-consistently.

Starting from the crystal structure of $Cs_2AgBiBr_6$, the most studied Pb-free double metal-halide perovskite reported for the first time in Ref. [224, 225], we design new theoretical compounds by varying the elements at both metal sites as well as at halide site, such that we form two groups of perovskites with B^{I}=Ag, B^{III}=Bi, In, Tl and B^{I}=Bi, K, Rb, Cs, B^{III}=In, respectively. For every combination in each of these groups we analyse three different possibilities for the halide site: X=Cl, Br, I. As previously stated in section 3.2, reducing dimensionality of simple and double metal-halide perovskites is a great strategy recently employed to improve the stability and tune optoelectronic properties of Pb-based perovskites. We therefore extend our study to the 2D RP phase of the double perovskites defined before, by replacing Cs with the longer BA organic molecule. The

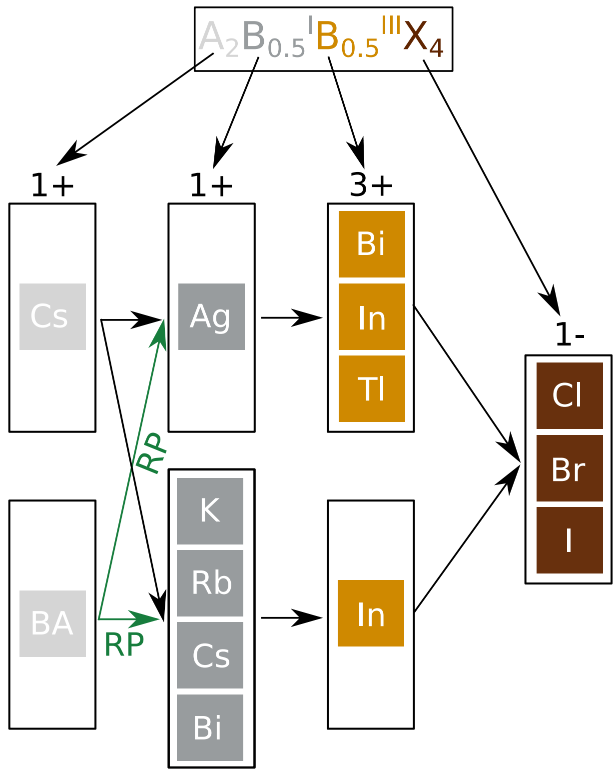

Figure 3.9: Schematic representation of the workflow used to design the theoretical 2D Ruddlesden-Popper systems analysed further.

schematic representation of the process used to design the range of theoretical double metal-halide perovskite structures is showed in Figure 3.9.

The workflow employed in this qualitative study consists of geometry optimizations of both the 3D and 2D RP phase of all theoretically designed double perovskites, followed by the computation of PBE fundamental band gaps of the relaxed systems. The results of both structural optimization and electronic structure calculation are reported in Table 3.3. We note that the use of PBE functional can yield band gaps by up to 2 eV lower than the experimental values and it can even lead to negative values of the band gaps, corresponding to a crossing of the valence and conduction bands at Fermi level. A similar behaviour has been previously observed of in Ref. [95], where the authors compute a ”negative” band gap for $Cs_2AgTlBr_6$ double perovskite using PBE. Despite the considerably underestimated absolute values of the band gaps, the overall trends are still trust worthy. Therefore, we conduct only a qualitative study whose results can narrow down the pool of Pb-free double perovskites featuring promising electronic properties to be further analysed in detail using improved methods.

Upon geometry optimization, we find that within the same combination of metal-sites, the unit cell volume increases with the increase of halide radius. Furthermore, Figure 3.10

Table 3.3: Unit cell volume (Ω in Å^3) and PBE+SOC fundamental band gaps (E_{gap}^{PBE} in eV) of 3D $Cs_2B^IB^{III}X_6$ and 2D RP $BA_2B^I_{0.5}B^{III}_{0.5}X_4$ with X=Cl, Br, I and B^I=Ag, B^{III}=Bi, In, Tl and B^I=Bi, K, Rb, Cs, B^{III}=In, respectively. The negative values are artifacts of using PBE and represent cases where a metallic character is predicted.

Metal-sites	**halide**	**all-inorganic 3D**		**RP 2D**	
		Ω (Å^3)	**E_{gap}^{PBE} (eV)**	**Ω (Å^3)**	**E_{gap}^{PBE} (eV)**
Ag-Bi	Cl	303.97	1.32	1623.120	2.69
	Br	351.34	0.96	1766.820	2.54
	I	425.21	0.47	1980.249	1.80
Ag-In	Cl	280.83	0.73	1597.687	2.34
	Br	325.82	0.01	1726.084	1.76
	I	401.90	-0.44	1958.674	1.19
Ag-Tl	Cl	290.23	-0.65	1590.267	0.80
	Br	336.29	-0.77	1731.537	0.60
	I	413.15	-0.52	1973.096	0.31
Bi-In	Cl	348.87	0.05	1689.268	1.89
	Br	393.79	-0.49	1837.604	1.16
	I	472.26	-0.70	2068.900	0.62
K-In	Cl	324.55	3.63	1621.863	3.38
	Br	377.69	2.42	1791.966	2.62
	I	471.01	1.20	2028.423	1.85
Rb-In	Cl	343.64	3.74	1652.173	3.45
	Br	398.57	2.56	1835.155	2.62
	I	493.96	1.36	2073.472	1.88
Cs-In	Cl	369.93	3.89	1705.954	3.47
	Br	426.14	2.78	1878.821	2.67
	I	524.00	1.60	2122.833	1.82

shows that the fundamental band gap of the analysed double metal-halide perovskites scales with the unit cell volume, independent of dimensionality. This result reinforces the speculation that fundamental band gaps are tunable over a wide range through halide substitution or hydrostatic pressure, as well as via chemical substitution at B^I and B^{III} metal sites.

Our results point towards Ag-Tl perovskites as one new family of low-gap 2D RP materials. Therefore, in the following structural and electronic properties of both Ag-Tl and the isoelectronic Ag-In RP double perovskites will be analysed using more accurate methodologies. However, we note that the high toxicity of Tl is expected to considerably

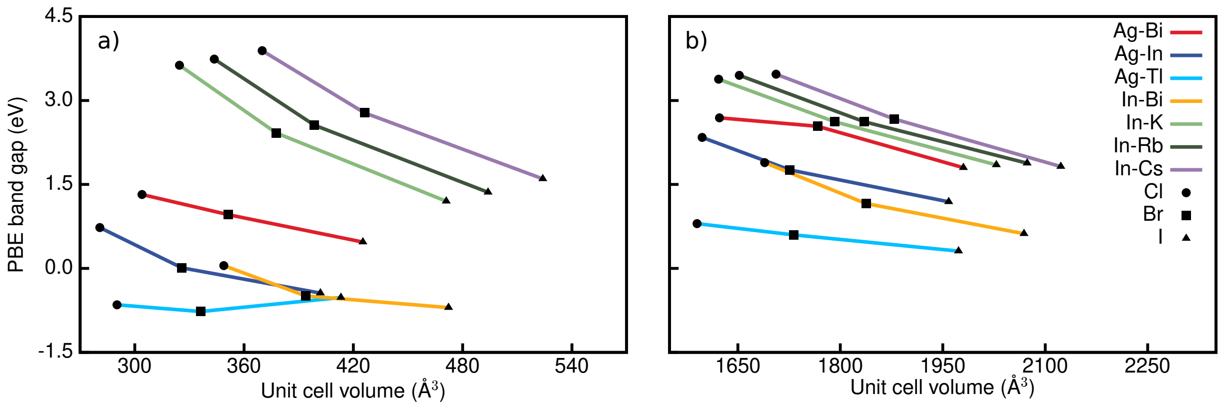

Figure 3.10: Fundamental band gap (in eV) as computed with PBE xc functional with respect to unit cell volume (in Å^3) for a) 3D and b) 2D double metal-halide perovskites. The different combinations of metal sites are represented in color, while the different halides are represented by different symbols as follows: Cl – dot, Br – square, I – triangle.

reduce their potential for optoelectronic applications. Furthermore, Ag-Bi and Ag-In 3D double perovskites exhibit promising band gaps for photovoltaic devices. Thus, we will employ advanced *ab initio* techniques to study both electronic and optical properties of these double metal-halide perovskites.

3.4. Electronic properties of $Cs_2AgB^{III}X_6$ halide double perovskites

In this section we analyse the effect of the chemical heterogeneity of double metal-halide perovskites on their electronic properties. Being one of the best electrical conductors, Ag is very promising for optoelectronic applications. Furthermore, in the octahedral environment, the ionic radii of Ag^+ (1.15 Å) is similar to those of Pb^{2+} (1.19 Å), and Bi^{3+} (1.03 Å), facilitating incorporation in the perovskite lattice [250]. Thus, by varying the chemical composition at B^{III}- and X-site, we study the electronic structure of $Cs_2AgB^{III}X_6$ double metal-halide perovskites, with B^{III}=Bi^{3+}, Sb^{3+}, In^{3+} and X=Cl^-, Br^-. The results on Ag-pnictogen family of double perovskites have been published in Ref. [149].

Ag-Bi double perovskites are the most studied Pb-free materials due to their exceptional semiconducting properties. The experimental synthesis of two members of this double perovskites family – $Cs_2AgBiCl_6$ [16, 225] and $Cs_2AgBiBr_6$ [16, 224, 225] – was successfully achieved, both via solid state reactions and via solution processing. Both $Cs_2AgBiBr_6$ and $Cs_2AgBiCl_6$ are indirect band gap semiconductors with cubic crystal structure (Fm$\bar{3}$m phase) at room temperature [225, 251]. Although the electronic structure of Ag-Bi double perovskites has been extensively studied, there is still disagreement regarding their experimental band gaps. The magnitude of the indirect band gap of $Cs_2AgBiCl_6$ has been reported to range between 2.20 eV [16] and 2.77 eV [225], while the indirect band gap of $Cs_2AgBiBr_6$ has been experimentally determined to lie between 1.83 eV [224] and 2.25 eV [252]. Among the possible causes for these significant dissimilarities are different methods of sample preparation and techniques used to determine the indirect band gap.

Concomitant with the successfully synthesis of $Cs_2AgB^{III}X_6$ (with B=Sb, Bi and X=Cl, Br, I) perovskites, the entire family of pnictogen noble-metal double-halide perovskites has been analysed via DFT computational screening [16]. Volonakis el al. demonstrated that the investigated perovskites exhibit small carrier effective masses and indirect band gaps below 2.7 eV, that decrease with the increase of the atomic radius of halogen or pnictogen. $Cs_2AgSbCl_6$ double perovskite has been successfully synthesized for the first time via solution-state reaction and experimentally characterized in Ref. [253]. More recently, Dahl et al. [254] synthesized colloidal $Cs_2AgSbCl_6$ nanocrystals and, with the use of Tauc plot, estimated an indirect band gap of 2.57 eV, in agreement with previous theoretical [16] and experimental [253, 255] reports.

In the past decade, $Cs_2AgInCl_6$, another Pb-free double perovskite, also drew the attention of the community due to its direct band gap character, long carrier lifetimes and easy solution processability [256]. Its first synthesis and characterization [257], many approaches have been explored to crystallize and modify its composition to yield suitable derivatives for various applications [230, 247, 258–260]. Pioneering work [255, 257, 258, 261] revealed that $Cs_2AgInCl_6$ exhibit a wide direct band gap at the center of Brillouin zone (Γ point). More recently, colloidal nanocrystals have also been synthesised [254, 262] and improved photoluminiscence quantum yield have been reported.

In the following we analyse the electronic structure of $Cs_2AgB^{III}X_6$ double perovskites with $B^{III}=Bi^{3+}$, Sb^{3+} and In^{3+} $X=Cl^-$, Br^- that crystallize in a cubic unit cell with $Fm\bar{3}m$ symmetry at RT and feature Ag- and B^{III}-centered alternating octahedra.

3.4.1. Electronic structure

The band structure of Ag-pnictogen family of halide double perovskite has been reported primarily based on density functional theory (DFT) calculations with the local density approximation (LDA) [16] and hybrid functionals [225], which are known to substantially underestimate QP or fundamental band gaps of many halide perovskites [95]. Accurate QP energies, and thus fundamental band gaps and band structures, can in principle be obtained using Green's function-based *ab initio* MBPT. The *GW* QP band gap of $Cs_2AgBiBr_6$ has been computed to be between 1.8 eV (G_0W_0@LDA) [23] and 2.2 eV (GW_0@PBE) [95], in good agreement with the range of experimental values. Furthermore, Ref. [23] reports an indirect band gap of 2.4 eV for the closely related $Cs_2AgBiCl_6$ double perovskite, as well as a direct gap ~0.7 eV larger.

The electronic band structure of $Cs_2AgInCl_6$ has also been broadly studied and the experimentally-determined direct band gap at Γ has been reported to lie between 2.1 eV [230] and 3.55 eV [259]. The fundamental direct gap has been computed within DFT to range between 0.93 eV [263] (using PBE functional) and 3.3 eV [257] (using PBE0 functional). Furthermore, Luo et al. reported the GW QP band gap to be 3.27 eV [230], in agreement with the experimental values. The large spread of the experimental band gap values has been attributed to the various preparation methods used in the synthesis of the perovskite crystals [256], whereas the variation of computed values can be explained based on the interplay between the different structural models and approximations for the exchange-correlation functional.

While both Ag-Bi and Ag-In double perovskite families have been extensively studied, to date there are only few reports on the electronic properties of Sb-based perovskites. The indirect band gap of $Cs_2AgSbCl_6$ compound is computed to range between 2.4 eV (HSE06) [253] and 2.6 eV (PBE0) [16].

Our workflow consists of computing the DFT Kohn-Sham eigenvalues E_{nk}^{DFT}, which are then perturbatively corrected to obtain the QP eigenvalues E_{nk}^{QP}, as previously defined by the equation 2.36 in Chapter 2. We find that Ag-pnictogen compounds show the characteristics of indirect band gap semiconductors, with the fundamental gap lying between the valence band maximum (VBM) at the X (0, $2\pi/a$, 0) point and the conduction band minimum (CBM) at the L (π/a, π/a, 0) point of the Brillouin zone. In contrast, $Cs_2AgInCl_6$ double perovskite exhibit a direct band gap at the Γ (0, 0, 0) point.

In agreement with previous reports[226, 264], the first conduction band of the Ag-pnictogen double perovskites is predominantly derived of Bi p and halide p states, while the first valence band features mainly Ag d_{z^2} and halide p states. Furthermore, small contributions from the B^{III}-metal s antibonding states and Ag s orbitals are observed at the VBM and CBM, respectively. All compounds exhibit a lowest direct transition at X with the exception of $Cs_2AgSbBr_6$, for which the the lowest energy direct band gap is located at L due to the pronounced Ag s orbital character of the CBM. The composition of the valence band of $Cs_2AgInCl_6$ double perovskite is somewhat similar to that of Ag-pnictogen double perovskites, featuring predominantly halide s and Ag d. However, the lack of pnictogen p states leads to a transition of the VBM from the X point to Γ. Furthermore, the orbital character of the conduction band is fundamentally different. The CBM is located at Γ and is made of mainly halide p and diffuse In s states, with sizeable contributions from the Ag s orbitals. Similar to lead-based perovskites, Cs-derived orbitals do not contribute to the states near band edges in none of the five studied double perovskites. Figure 3.11 shows the QP band structure of cubic $Cs_2AgBiBr_6$, $Cs_2AgSbBr_6$ and $Cs_2AgInCl_6$ double perovskites, calculated within the G_0W_0 approximation [265], overlayed with the orbital character of the energy bands. We note that the electronic band structures of $Cs_2AgBiCl_6$ and $Cs_2AgSbCl_6$ are very similar with that of $Cs_2AgBiBr_6$ double perovskites in terms of both positions of the indirect band gap and direct lowest transition, as well as orbital composition of the bands. Therefore, in Figure 3.11, we represented only the fundamentally different electronic structures.

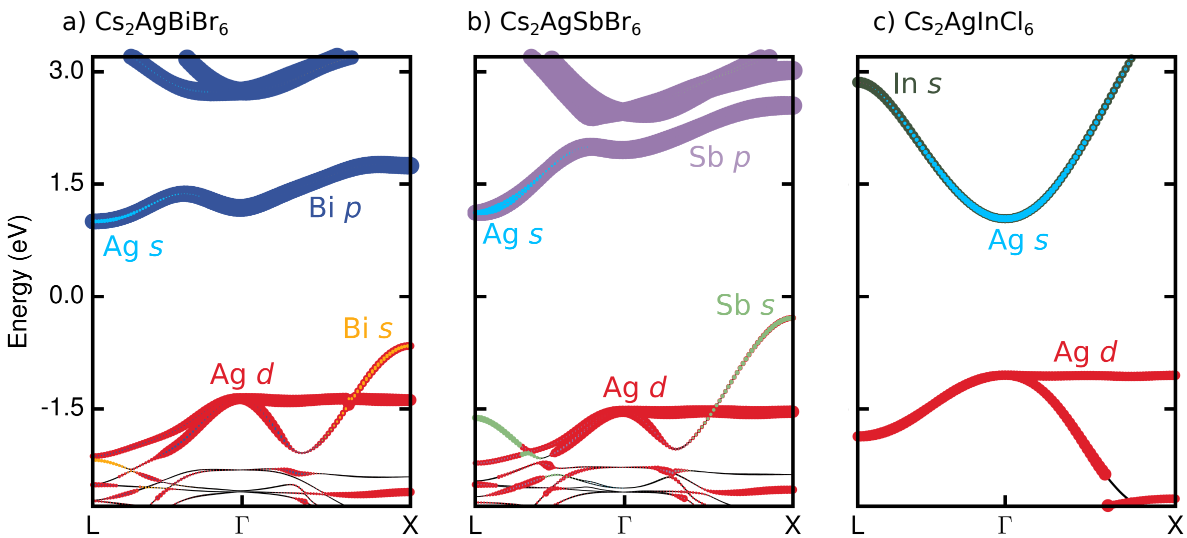

Figure 3.11: Quasiparticle band structure of cubic $Fm\bar{3}m$ a) $Cs_2AgBiBr_6$, b) $Cs_2AgSbBr_6$ and c) $Cs_2AgInCl_6$ along the L $[1/2, 1/2, 1/2]2\pi/a$ - Γ $[0, 0, 0]$ - X $[0, 1, 0]2\pi/a$ path, overlayed with the orbital character of the bands. The size of the colored dots is proportional to the percentage contribution of the orbital character to the electronic bands. Cs-derived orbitals do not contribute to the states near the band edges and halide character was omitted for clarity.

The magnitude of the band gaps (direct and indirect), computed within both DFT and G_0W_0 approximation, is reported in Table 3.4. The underestimation of the calculated QP indirect gap (between the VBM at X and the CBM at L) with respect to the experiments [16, 224, 225, 253] is a common feature of all Ag-pnictogen double perovskites studied. However, this discrepancy is consistent with previous GW calculations [23, 95] and can be explained based on the computational methodology employed, LDA approximation chosen for the mean-field calculations leading to a small DFT band gap [266]. Although a different starting point has been chosen to investigate the electronic properties of $Cs_2AgInCl_6$ double perovskite, we find a similar underestimation of the band gap with respect to previous reports [230], highlighting the similarities between the LDA and PBE exchange-correlation functionals.

As expected, the one-shot G_0W_0 approach leads to a rigid shift in the conduction band energies, as compared to the DFT eigenvalues. The QP corrections determine a change in both energy values and band dispersion in the valence band region, resulting in an opening of the band gap of at least 0.7 eV, while generally preserving the shape of the band edges.

Table 3.4: DFT and G_0W_0 lowest indirect and direct QP band gap of cubic $Cs_2AgB^{III}X_6$ (with B^{III}=Bi, Sb, In and X=Br, Cl).

		QP band gap (eV)	
		Indirect	**Direct**
		$\mathbf{X^{VBM} \rightarrow L^{CBM}}$	$\mathbf{X^{VBM} \rightarrow X^{CBM}}$
$Cs_2AgBiBr_6$	LDA	0.90	1.66
	G_0W_0	1.67	2.41
$Cs_2AgBiCl_6$	LDA	1.27	1.89
	G_0W_0	2.06	2.98
$Cs_2AgSbCl_6$	LDA	1.04	2.28
	G_0W_0	2.26	3.43
		$\mathbf{X^{VBM} \rightarrow L^{CBM}}$	$\mathbf{L^{VBM} \rightarrow L^{CBM}}$
$Cs_2AgSbBr_6$	LDA	0.58	1.79
	G_0W_0	1.41	2.74
			$\mathbf{\Gamma^{VBM} \rightarrow \Gamma^{CBM}}$
$Cs_2AgInCl_6$	PBE	—	0.91
	G_0W_0	—	2.09

3.4.2. Effective mass

In order to quantify the change in the band dispersion observed in the previous section, we compute the effective masses at the band edges corresponding to the lowest direct transition.

The effective mass tensor is evaluated by computing the second derivatives of the valence and conduction band edges with respect to the wave vector $\boldsymbol{k}$ along the three crystallographic directions, as

$$\frac{1}{m^*_{\alpha\beta}} = \frac{1}{\hbar^2}\frac{\partial^2 \varepsilon}{\partial k_\alpha \partial k_\beta} \tag{3.2}$$

for $\alpha, \beta = x, y, z$. The second-order partial derivatives are calculated numerically using finite differences in the first order, then the effective mass tensor is diagonalized for the conduction and valence band to obtain the electron and hole effective masses, respectively. The isotropic hole and electron effective masses are calculated as the harmonic mean

$$m^*_{h(e)} = \frac{3m_{h(e)_1}m_{h(e)_2}m_{h(e)_3}}{m_{h(e)_1}m_{h(e)_2} + m_{h(e)_2}m_{h(e)_3} + m_{h(e)_3}m_{h(e)_1}} \tag{3.3}$$

of the valence and conduction band effective masses, respectively, where the indices correspond to three orthogonal directions in a reference frame where the matrix of partial derivatives is diagonal. The longitudinal effective mass, $m_{h(e)_3}$, corresponds to the direction from X to Γ as represented in Figure 3.11, while the transverse effective masses, $m_{h(e)_1}$ and $m_{h(e)_2}$, correspond to the two directions perpendicular to that path.

The effective masses of $Cs_2AgB^{III}X_6$ (B^{III}=Bi, Sb and X=Br, Cl) at the point of the lowest direct transition calculated with DFT-LDA and G_0W_0@LDA, respectively, reported in Table 4.4, are in good agreement with the values obtained from DFT in Ref. [16]. As shown in Figure 3.11, the CBM at X of Bi-based and $Cs_2SbAgCl_6$ is almost dispersionless. Therefore, the reduced effective mass was approximated with the isotropic hole effective mass: $\frac{1}{\mu} = \frac{1}{m_h^*}$. In contrast, for $Cs_2AgSbBr_6$ the lowest direct transition is at L instead of at X (see Figure 3.11 c) and Table 3.4). Furthermore, at L the VBM changes its curvature along two of the three orthogonal directions, yielding an ill-defined hole effective mass and leading to the approximation of the reduced effective mass of $Cs_2AgSbBr_6$ with the isotropic electron effective mass: $\frac{1}{\mu} = \frac{1}{m_e^*}$.

Table 3.5: Effective masses of cubic $Cs_2AgB^{III}X_6$ (with B^{III}=Bi, Sb, In and X=Br, Cl) at the band edges corresponding to the lowest direct transition (in units of the electron rest mass m_0), as computed within DFT and G_0W_0. The indices correspond to principal axes of the effective mass tensor. $m^*_{h(e)}$ is computed as the harmonic mean of the masses along the three principal components. Hole effective mass of $Cs_3AgInCl_6$ double perovskite has been computed taking into account both valence bands having their maximum at Γ.

		Effective mass (m_0)							
		m_{h_1}	m_{h_2}	m_{h_3}	m_h^*	m_{e_1}	m_{e_2}	m_{e_3}	m_e^*
$Cs_2AgBiBr_6$	LDA	0.79	0.73	0.17	0.36	—	—	—	—
	G_0W_0	0.72	0.67	0.15	0.31	—	—	—	—
$Cs_2AgBiCl_6$	LDA	1.08	0.78	0.19	0.39	—	—	—	—
	G_0W_0	0.75	0.56	0.17	0.33	—	—	—	—
$Cs_2AgSbCl_6$	LDA	1.25	0.98	0.17	0.39	—	—	—	—
	G_0W_0	0.96	0.71	0.15	0.32	—	—	—	—
$Cs_2AgSbBr_6$	LDA	—	—	—	—	0.31	0.29	0.25	0.28
	G_0W_0	—	—	—	—	0.33	0.30	0.26	0.29
$Cs_2AgInCl_6$	PBE				0.70				0.28
	G_0W_0	0.62	0.60	0.57	0.59	0.30	0.29	0.29	0.29

We note that the effective mass tensor of Ag-pnictogen double perovskites is highly anisotropic, featuring an exceptionally low transverse effective mass along the direction from X to Γ, in line with previous reports correlating the rocksalt packing of Ag and Bi ions with noticeable anisotropic effects [221]. In contrast, as showed in Table 3.5, both electron and hole effective masses of $Cs_2AgInCl_6$ compound are isotropic. Along with the VBM shift to Γ, the absence of B^{III} p orbitals also leads to a distinction between a light hole originating from the disperse band and a heavy hole arising from the flat band. The effective mass of the light hole, obtained by neglecting the effect of the dispersionless band, is approximately half of that computed by taking into account both bands, suggesting that the hole effective mass is highly dependent on the inclusion of the flat valence band. Therefore, we report and hereafter employ only the hole effective mass computed as the average between the light and the heavy hole.

3.5. Dimensional reduction of Pb-free double metal-halide perovskites

As previously mentioned in section 3.1, the dimensional reduction of hybrid organic-inorganic perovskites has been increasingly used as a strategy to improve their structural stability [14]. While, the attention has been mainly focused on divalent cations-based perovskites such as Pb-, Cu-, Mn-, Cd- and Sn-based [267], recent efforts have been directed towards understanding the physical and optoelectronic consequences of dimensional reduction of double metal-halide perovskites [264, 268–270]. Connor et al. reported in Ref. [264] an indirect-to-direct conversion of the band gap in $Cs_2AgBiBr_6$ double perovskite as the inorganic lattice is thinned to a monolayer. The minimal effect of quantum confinement observed in the lower dimensional Ag-Bi perovskites raises the question if this is a general characteristic of dimensional reduction in double perovskites or its a particularity linked to the specific chemical composition of Ag-Bi materials. In one of the first studies on 2D double perovskites, Castro-Castro et al. reported that the interactions between the I^- ion and the inorganic lattice in 2D Au^{I}-Au^{III} double perovskites, absent in the 3D analogues, significantly perturb the electronic structure. Recently, Bi et al. [269] analysed the 2D RP Cu^{I}-Bi^{III} compound, but there is no 3D analogue for comparison. Thus, with just a few reports on a very limited range of double perovskites, little can be learned about the optoelectronic effects of dimensional reduction.

To probe the importance of the chemical heterogeneity in determining the effects of dimensional reduction, in this section we compare dimensional confinement of a 3D halide perovskite with essentially different electronic structure, i.e. the indirect gap semiconductor $Cs_2AgBiBr_6$ and the direct gap semiconductor, with a more delocalized electronic structure $Cs_2AgTlBr_6$. Recently, the Ag-Tl 3D double perovskite have been synthesized and characterised in a combined experimental and theoretical study [271]. Furthermore, it has been demonstrated that it features an unusually small band gap of $\sim$0.95 eV and large band dispersion. Here, we analyse the effects of dimensional reduction on the optoelectronic properties of $Cs_2AgTlBr_6$ in a family of double hybrid organic-inorganic perovskites: a 2D $n = 2$ perovskite ($(A)_2CsAgTlBr_7$; A = phenethylammonium (PEA), referred to as

2-Tl, a 2D $n = 1$ perovskite ($(3\text{-BPA})_4AgTlBr_8$; 3-BPA = 3-bromopropylammonium, referred to as **1-Tl**), and a quasi-one-dimensional (1D) $n = 1$ perovskite ($(HIS)_2AgTlBr_8$; HIS = histammonium, referred to as **1'-Tl**). Next, we study an isoelectronic and isostructural analogue of **1-Tl** – the $n = 1$ double perovskite ($(3\text{-BPA})_4AgInBr_8$, referred to as **1-In**. We explore the evolution of the band structure in these reduced dimensionality systems of the Ag-Tl and Ag-In perovskite families by means of *ab initio* DFT. Furthermore, we compare their electronic structure with that of $(BA)_4AgBiBr_8$ and $(BA)_2AgBiBr_7$ (referred to as **1-Bi** and **2-Bi**, respectively), that have been synthesised by Connor et al. in Ref. [264]. We published the results presented in this section in Ref. [270], where these various perovskite materials have also been experimentally synthesized and characterised.

3.5.1. Crystal structures

Figure 3.12 shows the single-crystal X-ray diffraction (SCXRD) lattice and structural details of Ag-Tl and Ag-In perovskites (3D and lower-dimensional) experimentally obtained by exfoliation of crystals synthesized from solutions of the precursors in concentrated hydrobromic acid as described in Ref. [270].

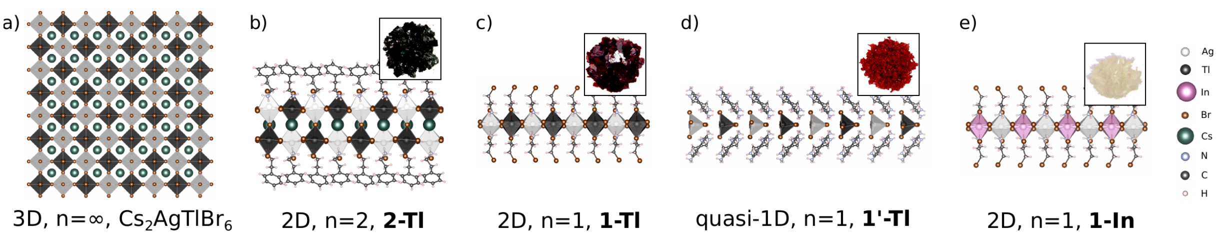

Figure 3.12: Experimental crystal structures of a) $Cs_2AgTlBr_6$ from Ref. [221] and lower-dimensional derivatives b) $(PEA)_2CsAgTlBr_7$ (**2-Tl**; PEA = phenethylammonium), c) $(3\text{-BPA})_4AgBiBr_8$ (**1-Tl**; 3-BPA = 3-bromopropylammonium), d) $(HIS)_2AgTlBr_8$ (**1'-Tl**; HIS = histammonium) and e) $(3\text{-BPA})_4AgInBr_8$ (**1-In**). Insets show the colors of the crystals and are reproduced from Ref. [270].

Dimensional reduction of $Cs_2AgTlBr_6$ halide double perovskite reported by Slavney et al. in Ref. [271] as having cubic $Fm\bar{3}m$ symmetry at RT and represented in Figure 3.12 a), leads to $PEA_2CsAgTlBr_7$ (**2-Tl**), a 2D RP perovskite with the thickness of inorganic layer of $n = 2$. The perovskite lattice is two octahedral layers thick and is formed by alternating Ag- and Tl-centered octahedra, with Cs cation inside the cavities between the inorganic slabs and longer organic molecules separating these sheets (see Figure 3.12 b)). Further dimensional reduction leads to $n = 1$ $(3\text{-BPA})_4AgTlBr_8$ (**1-Tl**), featuring the same perovskite framework with Ag and Tl cations alternating at B-sites and bilayers of 3-BPA cations separating the inorganic sheets (see Figure 3.12 c)).

Furthermore, as showed in Figure 3.12, the inorganic sheets in both 2D perovskites **2-Tl** and **1-Tl** are heavily distorted, particularly at the Ag site. The off-centering movement of the Ag atoms in **2-Tl** leads to the formation of a short bond of ∼2.67 Å with the terminal axial Br and a long bond of ∼3.08 Å with the bridging axial Br. Similar distortions have been previously observed in some 2D oxide perovskites [272, 273] and in the closely related 2D RP $(BA)_2CsAgBiBr_7$ perovskite [264]. In **1-Tl**, the Ag–Br octahedra show a tetragonal distortion with two extremely short bonds of ∼2.56 Å between Ag and the axial terminal Br and four long bonds of ∼3.06 Å and ∼3.14 Å between Ag and the bridging equatorial Br. Although larger in magnitude, these distortions are similar with the ones observed in analogous $(BA)_4AgBiBr_8$ [264]. The values of all $Ag - Br$ and $Tl - Br$ bond lengths are reported in Table 3.6.

Table 3.6: Structural details of $(HIS)_2AgTlBr_8$ (**1'-Tl**), $(3\text{-}BPA)_4AgTlBr_8$ (**1-Tl**), $(PEA)_2CsAgTlBr_7$ (**2-Tl**) and $(3\text{-}BPA)_4AgInBr_8$ (**1-In**).

	Structure			
	1'-Tl	**1-Tl**	**2-Tl**	**1-In**
Space group	$C2/c$	$P2/c$	$P-1$	$P2/c$
a (Å)	11.3098	8.4673	7.8618	8.4965
b (Å)	12.6075	7.8406	7.8618	7.8419
c (Å)	18.2064	26.1647	23.0185	26.1413
$\boldsymbol{\alpha}$**(°)**	90.000	90.000	83.703	90.000
$\boldsymbol{\beta}$**(°)**	95.713	90.312	85.727	90.318
$\boldsymbol{\pi}$**(°)**	90.000	90.000	89.819	90.000
$\boldsymbol{\Omega}$**(Å³)**	2583.11	1737.02	1411.41	1741.73
d^{ax}_{Ag-Br} (Å)	2.6430	2.5665	2.6699, 3.0826	2.5565
d^{eq}_{Ag-Br} (Å)	3.0628 3.7870	3.1421 3.0576	2.8420, 2.8451 2.9014, 2.8393	3.2060 3.1257
d^{ax}_{Tl-Br} (Å)	2.6552	2.7410	2.6985, 2.6818	2.6717
d^{eq}_{Tl-Br} (Å)	2.7005 3.3771	2.7452 2.7055	2.7332, 2.7342 2.7493, 2.7617	2.6872 2.6584

We further decreased the dimensionality of the inorganic lattice of **1-Tl**, using HIS – an even bulkier organic spacer cation, and obtained $(HIS)_2AgTlBr_8$ (**1'-Tl**), a similar perovskite featuring 2D $n = 1$ sheets of perovskite lattice separated by layers of HIS. However, due to the very large cation, the perovskite backbone is significantly distorted, resulting in a breaking of metal-halide octahedra. The inorganic layer features five metal-bromide bonds with a standard average length, and a sixth unusually long metal-bromide bond. Due to this long bond pointing in the same direction, the 2D inorganic lattice becomes a series of 1D in-plane chains (see Figure 3.12 d)). A detailed quantitative analysis of the bond lengths showed in Table 3.6 reveals that the bonds parallel with the chain axis are similar with the equatorial bonds found in **1-Tl** system, while the perpendicular bonds are at least 21 % longer than those of **1-Tl** system. Thus, the **1'-Tl** system is a quasi-1D structure.

To study the effect of the chemical composition at B^{III}-site, we replace thallium with indium in **1-Tl** and obtain the isostructural and isoelectronic system $(3\text{-BPA})_4AgInBr_8$ (**1-In**), which displays resembling distortions. Although similar, **1-In** exhibits a slightly larger axial compression of $Ag - Br$ bond lengths, as showed in Table 3.6. It has been reported that the $InBr_6$ octahedron features a tolerance factor slightly larger that the critical limit, suggesting an unstable 3D parent [257]. Indeed, although the crystallisation of $Cs_2AgInCl_6$ has been reported in Ref. [257], to date there is no report of successful experimental synthesis of the bromide analogues.

3.5.2. Electronic composition of layered perovskites

Although the Ag-Tl and Ag-In systems feature very similar distortions with the one observed in the Ag-Bi layered double perovskites reported in Ref. [264], suggesting similar structural consequences of dimensional reduction, the crystals showed in the insets of Figure 3.12 exhibit significant color difference. While the crystals of $n = 1$ and $n = 2$ Ag-Bi are known to be a nearly identical shade of yellow [264], dimensional reduction of Ag-Tl systems leads to a pronounced color change ranging from black for **2-Tl** to maroon for **1-Tl** to red for **1'-Tl**, suggesting a fundamental difference in the electronic structures of these materials. To explore these underlying electronic differences we compare the band structures of Ag-Tl systems with those of Ag-Bi systems, as computed with first principles DFT approach. While the band structures of **1-Bi** and **2-Bi** are computed within the PBE approximation, including spin-orbit coupling self-consistently, the band structures of the Ag-Tl and Ag-In families of layered double perovskites were computed within the HSE06 approximation, without taking into account the effect of spin-orbit coupling (see Appendix A.2.4 for extensive computational details). The results of our fundamental band gap calculations are reported in Table 3.7.

Figure 3.13 shows the crystal structures and the electronic band structures of $n = 1$ and $n = 2$ Ag-Tl and Ag-Bi 2D layered perovskites, overlaid with the orbital contributions. Although Ag d and Br p states are the main contributions to the VBM of all four materials, the **2-Bi** system feature the additional contributions from Bi s orbitals as well. While the valence band feature a remarkably similar orbital composition, the conduction band is essentially different. In the case of Ag-Bi layered perovskites, the CBM is primarily derived from Bi p and Br p orbitals, whereas the CBM of Ag-Tl perovskites is composed of Tl s and Br p states. However, both **2-Tl** and **2-Bi** feature minor contributions from Ag s orbitals. We hypothesize that this different composition of the conduction band is one of the causes of the significantly different optical behavior of the Ag-Bi and Ag-Tl perovskites reported in Ref. [270] and seen as the significant color difference. Furthermore, we see a reversed trend of the band gap with the thickness of the inorganic layer in these

2D layered perovskites. While the band gap of the Ag-Bi systems change from indirect to direct when the dimensionality decreases from $n = 2$ to $n = 1$, for the Ag-Tl systems we observe a direct-to-indirect gap transition as the perovskite lattice is thinned to a monolayer.

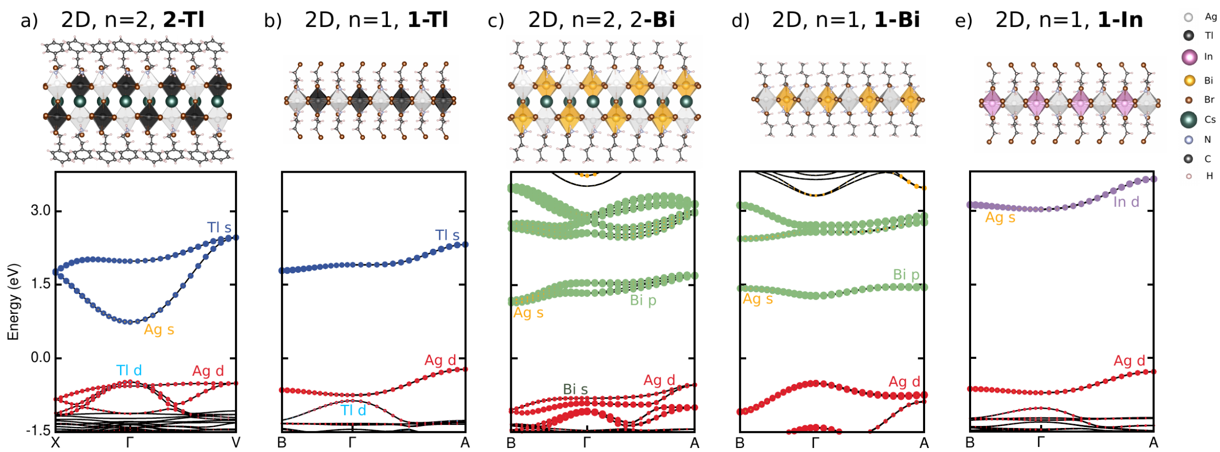

Figure 3.13: Crystal structures (top) and electronic band structures of a) **2-Tl**, b) **1-Tl**, c) **2-Bi**, d) **1-Bi** and e) **1-In** overlaid with the orbital character of the bands. The size of the colored dots is proportional to the percentage contribution of the orbital character to the electronic bands. The halide contributions are present throughout, but there were omitted for clarity.

As expected, the band structure of **1-In** showed in Figure 3.13 is similar to that of isoelectronic **1-Tl** perovskite. They both feature an indirect band gap and comparable overall band dispersion. Furthermore, the orbital composition of the valence and conduction regions is similar between the two perovskites, with the VBM of the **1-In** composed of Ad d and Br p contributions and the CBM made of In s and Br p. However, the significantly higher energy of the In 5s orbitals lead to a shift of the conduction band towards higher energies, yielding a much larger band gap for **1-In** as compared with that of **1-Tl**. This result is consistent with both experimental observations [264] and theoretical calculations for an analogous structure [274].

3.5.3. Electronic effects of dimensional reduction

Consistent with previous reports [264], we find that dimensional reduction of $Cs_2AgBiBr_6$ leads to a change in the nature of the band gap when the thickness of the perovskite layer decreases to $n = 1$. A similar indirect-to-direct gap transition has been observed while exfoliating bulk MoS_2 to individual layers [275, 276]. Upon dimensional reduction of $Cs_2AgTlBr_6$, despite the different orbital makeup, the calculations show a comparable intriguing band gap transition.

Figure 3.14 a) shows the crystal structure and electronic band structure of 3D double perovskite $Cs_2AgTlBr_6$. In line with previous results [271], we compute a direct band gap at Γ (0, 0, 0) point in the Brillouin zone. Although the absolute value of the band gap of 0.12 eV is significantly lower than the earlier reported values, our calculations correctly predict the semiconducting properties of the material. The severely underestimation of the band gap is explained in detail in Appendix A.2.4, based on the DFT approach used. The VBM is composed of Ag d and Br p orbital contributions and the CBM has Ag s, Tl s and Br p character. The pronounced dispersion of the conduction band is a consequence of the increased electronic delocalization, due to better overlap between the spherical, more diffuse Tl s orbitals with the halide p orbitals. The band structure of **2-Tl** depicted in Figure 3.14 c), is analogues to that of the 3D $Cs_2AgTlBr_6$ parent, with a computed direct band gap at Γ of 1.22 eV and similar orbital composition and dispersion of the bands, highlighting the correlation between the electronic structures of the 3D and 2D $n = 2$ Ag-Tl perovskites. To validate the hypothesis that the lower-dimensional derivatives of $Cs_2AgTlBr_6$ (with the inorganic layer thickness $n \geq 2$) inherit its electronic properties, we construct a theoretical model system by optimizing the geometry of an $n = 3$ slab cut from the 3D perovskite and referred to as **3M**. The band structure of **3M** showed in Figure 3.14 b), is completely analogous to those of 3D $Cs_2AgTlBr_6$ and **2-Tl**, reinforcing the result that all materials with $1 < n < \infty$ have similar band structures.

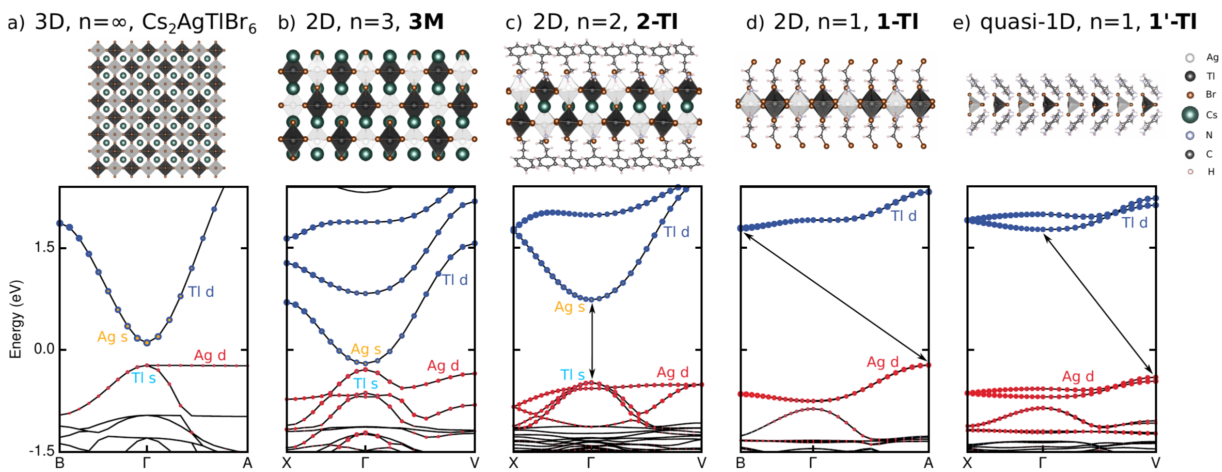

Figure 3.14: Crystal structures (top) and electronic band structures of a) 3D $Fm\bar{3}m$ $Cs_2AgTlBr_6$, b) **3M**, c) **2-Tl**, d) **1-Tl** and e) **1'-Tl**. Orbital contributions to the band structures are showed in colors. The size of the colored dots is proportional to the percentage contribution of the orbital character to the electronic bands. The halide contributions are present throughout, but there were omitted for clarity. Analogous k-paths are plotted in all panels to demonstrate the decrease in band dispersion with dimensional reduction and to highlight the abrupt change in band structure at the $n = 1$ limit.

Dimensional reduction of the Ag-Tl perovskite lattice to a monolayer ($n = 1$) in **1-Tl** leads to a striking change in the electronic band structure. Most notably, as showed in Figure 3.14 d) and Table 3.7, the band structure of **1-Tl** exhibits an indirect band gap of 2.00 eV between the VBM at A (π/a, π/b, 0) and the CBM at B (π/a, 0, 0). Another considerable difference with respect to the $n \geq 1$ derivatives, is the reduced Ag s orbital character of the conduction band in **1-Tl** perovskite, leading to an almost pure Ag-to-Tl transition between the band edges. Furthermore, similar to **2-Tl**, the electronically 2D nature of **1-Tl** is highlighted by the lack of dispersion along the layer stacking direction.

Table 3.7: Calculated fundamental band gap of experimental and theoretical model structures.

System	xc functional	k-points	Band gap (eV)
$Cs_2AgTlBr_6$	HSE06	Γ	0.12
2-Tl		Γ	1.22
1-Tl		$A^{VBM} \rightarrow B^{CBM}$	2.00
1'-Tl		$V^{VBM} \rightarrow \Gamma^{CBM}$	2.17
1-In	HSE06	$A^{VBM} \rightarrow B^{CBM}$	3.30
2-Bi	PBE	$A^{VBM} \rightarrow B^{CBM}$	1.66
1-Bi		Γ	1.7

As previously demonstrated in Ref. [264], dimensional reduction impacts the electronic structure both directly by reducing the thickness of the perovskite lattice and indirectly by structural distortions. To discriminate between the direct effects inflicted by the reduced dimensionality and those induced by the structural distortions on the electronic structure, we construct model systems with inorganic layer thickness $n = 1$ and $n = 2$, referred to as **1M** and **2M**, featuring untilted and undistorted metal-halide octahedra as found in the 3D cubic $Cs_2AgTlBr_6$ parent (see Appendix A.2.4 for detailed description of the model systems). The nature of the band gap in the model systems **1M** and **2M** is similar to that of the gap in the analogues hybrid organic-inorganic layered perovskites **1-Tl** and **2-Tl**, respectively. Although as reported in Table 3.8 the CBM shifts to Γ for **1-Tl**, the nature of the lowest energy direct transition remains indirect, suggesting that the direct-to-indirect gap transition is a direct consequence of dimensional reduction.

We validate our observation of the direct-to-indirect gap transition when the thickness of the inorganic lattice is reduced to a monolayer by comparing the electronic structure of **1-In** with that of $Cs_2AgInCl_6$, the only related 3D perovskite available. While the 3D parent has been reported to have a direct band gap at Γ [257], **1-In** features an indirect band gap of 3.30 eV between the VBM at A and the CBM at Γ. This additional confirmation of the direct-to-indirect band gap transition highlights the significance of orbital symmetry in dictating the nature of the gap in both 3D double perovskites and their layered derivatives [221, 255].

It is also worth noting that, although the quasi-1D system **1'-Tl** features significant

Table 3.8: Lowest energy transitions of experimental and theoretical model structures of Ag-Tl layered perovskites as computed with HSE06.

	k-points	**Energy gap (eV)**
1-Tl	$A^{VBM} \rightarrow B^{CBM}$	2.00
	$A^{VBM} \rightarrow \Gamma^{CB}$	2.13
	Γ	2.65
1M	$A^{VBM} \rightarrow B^{CB}$	1.84
	$A^{VBM} \rightarrow \Gamma^{CBM}$	1.65
	Γ	1.72
2-Tl	Γ	1.22
	$V^{VB} \rightarrow \Gamma^{CBM}$	1.24
2M	Γ	0.98
	$V^{VB} \rightarrow \Gamma^{CBM}$	1.04

structural distortions, it still exhibits an indirect band gap of 2.17 eV, between the VBM at V (π/a, π/b, 0) and the CBM at Γ. Furthermore, the orbital character of the bands is similar with that of **1-Tl** system, with the VBM composed of Ag d and Br p states and Tl s and Br p orbitals dictating the character of the CBM. However, as showed in Figure 3.14 e), the lower dimensionality of the system is apparent in the considerably lower dispersion of the bands.

In summary, in this section we analysed the Ag-Tl layered double perovskites family by means of *ab initio* first principles calculations and showed that while the electronic structure of 2D $n \geq 2$ derivatives is remarkably similar to that of the 3D parent $Cs_2AgTlBr_6$ retaining the direct band gap, in the limit $n = 1$ the 2D layered perovskite **1-Tl** has a strikingly different electronic structure, featuring an indirect band gap. This indirect gap is retained in the quasi-1D **1'-Tl** material, despite the significant distortions of the inorganic lattice. We demonstrated that the direct-to-indirect band gap transition is a robust result by computing a similar transition for the isoelectronic **1-In** layered perovskite. Importantly, using calculations on undistorted model structures, we find that this direct-to-indirect band gap transition is driven by dimensional reduction rather than by the structural distortions of the perovskite lattice observed in the lower dimensional materials. Furthermore, by comparing the effects of the dimensional reduction on Ag-Tl and Ag-In families with those on the electronically distinct Ag-Bi family of layered double perovskites, we showed that the intriguing transition of the band gap is dictated by the symmetry of the orbitals governing the band edges.

Chapter 4

Optical properties of 3D halide double-perovskites

This chapter presents a detailed analysis of the optical absorption spectrum of cubic $Cs_2AgBiBr_6$ double perovskite, as computed within the G_0W_0+BSE approach. Furthermore, the non-hydrogenic nature of strongly localized resonant excitons in the double perovskite series $Cs_2AgB^{III}X_6$ (B^{III}=Bi, Sb and X = Br, Cl) is explained. The limitations of Elliott theory and the Wannier-Mott model to describe the optical excitations in these materials is discussed in detail, as well as the impact of the anisotropy of effective masses and local field effects. We published the results presented in this chapter in Ref. [149]. The last section gives an overview on the particular optical properties of $Cs_2AgInCl_6$ double perovskite, discussing the effect of band edges orbital character on the excited states.

4.1. Exictonic properties of $Cs_2AgBiBr_6$ double perovskite

Despite recent studies [277–280] on excitonic properties of $Cs_2AgBiBr_6$ double perovskite, the origin of the experimental peak observed at 2.8 eV measured in thin films is still controversial as pointed out in Ref. [280]. In experiments performed on powder samples [224, 278], which report optical spectra for energies up to 2.7 eV, such a peak is absent and a peak at lower energy is found. Furthermore, reported exciton binding energies differ by almost a factor of 4. Based on temperature-dependent steady-state photoluminiscence experiments, Steele et al. [278] estimated the exciton binding energy of $Cs_2AgBiBr_6$ to be 70 meV. Kentsch et al. [277] used femtosecond transient absorption measurements and found an exciton binding energy of 268 meV by fitting the region of the direct transition using the Elliott model [281]. Moreover, Ref. [148] reports an even larger exciton binding energy (340 meV) from first principles calculations. This wide spread of exciton binding energies calls for a systematic study.

Figure 4.1 a) shows the linear optical absorption spectrum of cubic $Fm\bar{3}m$ phase of $Cs_2AgBiBr_6$, computed by means of *ab initio* many body perturbation theory. By comparing the absorption spectrum within the RPA with the one calculated within the G_0W_0+BSE approach, one can observe that the inclusion of electron-hole interactions red-shift the absorption spectrum. Furthermore, the electron-hole interactions give rise to a

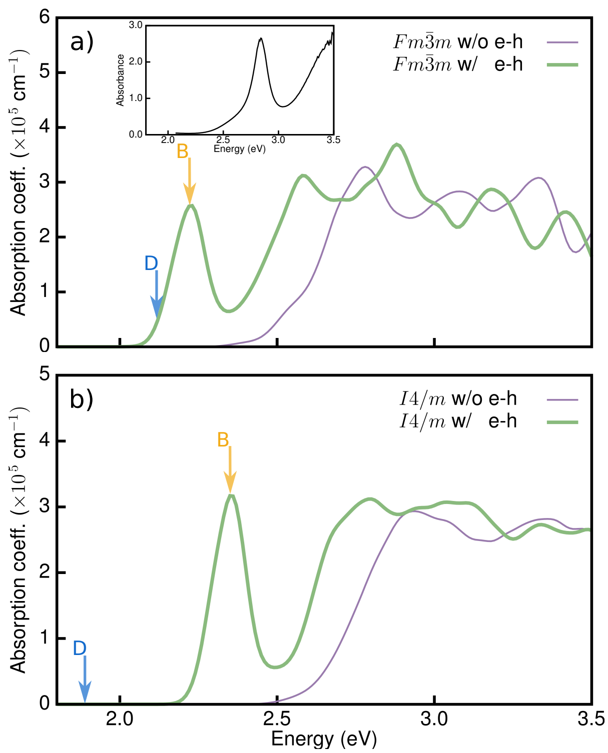

Figure 4.1: a) Calculated optical absorption spectrum of cubic $Fm\bar{3}m$ phase of $Cs_2AgBiBr_6$, experimental optical absorption spectrum (inset). b) Calculated optical absorption spectrum of tetragonal $I4/m$ phase of $Cs_2AgBiBr_6$. The spectra calculated using the random phase approximation (RPA) without local field effects are represented in purple and the ones computed within G_0W_0+BSE approach are represented in green. The first dark and first bright excitonic states are marked by a blue arrow labeled D and an orange arrow labeled B, respectively. The experimental absorption spectrum from inset was adapted with permission from [280]. Copyright 2020 American Chemical Society.

new well-defined peak below the lowest direct band gap, indicative of a strongly bound exciton. This peak is centered at an energy 570 meV larger than the indirect band gap, revealing the signature of a resonant exciton. Analysing the fine structure of this excitonic feature we find a group of three degenerate bright states (marked as B in Figure 4.1 a)) and an optically inactive (dark) state (marked as D) 80 meV below the excitonic peak.

In order to facilitate the comparison with experiments, in which only signals from bright states can be observed, we will focus on the description of *first bright* excitons only, unless stated otherwise. Limitations of the DFT starting point previously reported in both halide double perovskites and lead-based perovskites [95, 282] lead to a noticeable underestimation of the QP band gap which results in a red-shift of ∼0.6 eV of our BSE computed optical absorption spectrum with respect to the experimental spectrum reported by Longo et al. in Ref. [280]. However, the lineshapes of the computed and experimental absorption spectra are very similar and both feature a well-defined peak before the onset of a broader continuum, albeit centered at different energies.

Furthermore, the excitonic feature at the onset of the optical absorption spectrum persists for the low-temperature tetragonal $I4/m$ phase [251], but the entire spectrum is blue-shifted with respect to the cubic $Fm\bar{3}m$ phase by ∼150 meV, as shown in Figure 4.1. This shift of the BSE absorption spectrum is consistent with the slightly larger QP direct band gap computed to be 2.54 eV. The band folding in the $I4/m$ phase leads to the formation of a range of dark excitonic states up to 414 meV below the first bright state (marked as D and B, respectively, in Figure 4.1 b)).

We define the exciton binding energy as the difference between the G_0W_0 lowest direct transition and the computed excitation energy of the resonant bright exciton and report a binding energy of 170 meV that falls within the range of experimentally determined values, but is half the value computed by Palummo et al. [148].

One of the causes for this discrepancy is the choice of the DFT starting point: LDA [61, 62] in our calculations vs. PBE [67] in Ref. [148]. Even though LDA and PBE are qualitatively similar starting points for the GW approach, they lead to slightly different results. The effect of using PBE as xc functional in the DFT calculations has been tested and Table 4.1 shows that the while the DFT starting point does not modify the value of the QP indirect band gap, it slightly lowers the lowest direct transition at the X point.

Table 4.1: Comparison between QP band gaps and computed exciton binding energy obtained using *evGW* in Ref. [148] and using G_0W_0 in our calculations.

	xc functional	**QP band gaps (eV)**		**Binding energy (meV)**	
		$X^{VBM} \rightarrow L^{CBM}$	$X^{VBM} \rightarrow X^{CBM}$	dark	bright
evGW [**148**]	PBE	2.1	2.7	480	340
G_0W_0	PBE	1.66	2.34	346	242
	LDA	1.66	2.40	253	170

Despite the similarity of the band gaps, Figure 4.2 shows that the excitonic peak in the absorption spectrum computed with a DFT-PBE starting point is red-shifted ∼50 meV and the exciton binding energy is increased by approximately 42 %. Even though there are large variations in the exciton binding energy depending on the DFT starting point, the presence of a well-defined peak due to electron-hole interactions is a robust result of our calculations. Overall, we find that the choice of structure and exchange-correlation functional can lead to a range of calculated exciton binding energies from 170 meV to 240 meV, which overlaps broadly with the range of experimental binding energies reported in the literature.

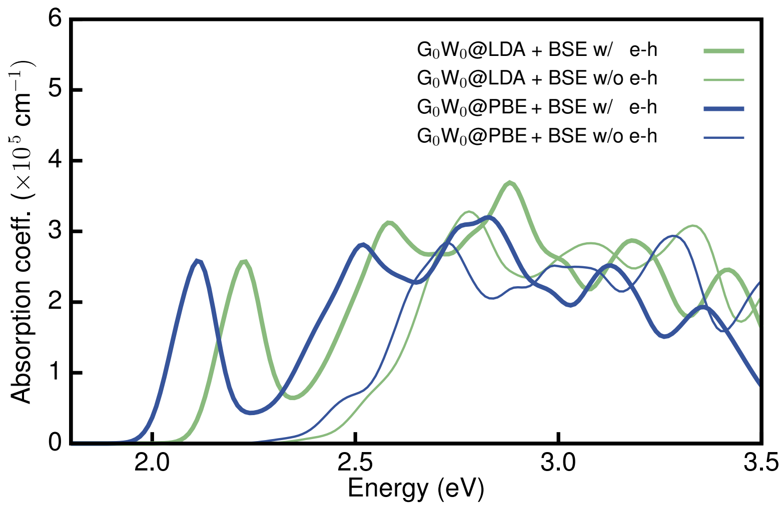

Figure 4.2: Optical absorption specta of $Cs_2AgBiBr_6$ computed with G_0W_0+BSE, using DFT-LDA (green) and DFT-PBE (blue) starting point.

Another important difference between the setup of the calculations is the density of the k-point mesh. We used a 2.5-times denser grid in order to compute the BSE binding energies, but also tested the same $4 \times 4 \times 4$ k-point grid as employed in Ref. [148]. With this new setting we obtain an exciton binding energy of 301 meV for the first bright state.

Other sources for the remaining difference of $\sim$40 meV between our exciton binding energy and the one reported in Ref. [148] are slightly different lattice parameters of the cubic $Cs_2AgBiBr_6$ and the use of partially self-consistent GW in Ref. [148], that is known to open up the QP band gaps by $\sim$0.3 eV for $Cs_2AgBiBr_6$ [95] and is likely also affecting the static dielectric constant.

4.2. Excitonic properties of Ag-pnictogen double perovskite family

As previously described in section 3.1, the heterovalent substitution at metal sites B^{I} and B^{III} is a broadly used approach for designing new materials with desired optoelectronic properties. In order to understand the effect of chemical composition at B^{III} site on the excitonic properties of halide double perovskites, we analyse other members of the Ag-pnictogen perovskite family as well. Following the same procedure and replacing Bi with Sb and Br with Cl, we compute the BSE optical absorption spectrum of cubic $Cs_2AgBiCl_6$, $Cs_2AgSbBr_6$, and $Cs_2AgSbCl_6$ and find that the high exciton binding energy is a common feature of all four compounds in the series. As shown in Table 4.2, the binding energies of the first bright state in $Cs_2AgB^{III}X_6$ compounds (B^{III}=Bi, Sb and X=Br, Cl) range between 170 and 434 meV and scale linearly with the G_0W_0 lowest direct band gap. The binding energies of the strongly-bound excitons in these compounds are significantly larger than those observed in the related 3D lead-halide perovskites [283], and similar with the ones typically reported in quantum confined systems like $Cs_3Bi_2I_9$ [147, 236].

Table 4.2: G_0W_0@LDA lowest direct transition (in eV), exciton binding energy (in meV), static dielectric constant as computed within the random phase approximation, and average electron-hole separation (in Å).

	Direct gap (eV) G_0W_0**@LDA**	ε_∞	**Exciton binding energy (meV)**	**Average e-h separation (Å)**
$Cs_2AgBiBr_6$	2.41	5.92	170	6.3
$Cs_2AgSbBr_6$	2.74	5.96	247	7.6
$Cs_2AgBiCl_6$	2.98	4.68	333	5.3
$Cs_2AgSbCl_6$	3.43	4.77	434	5.6

To probe the expectation that such strongly-bound excitons are likely to be highly-localized within the crystal lattice, we compute the probability distribution of the exciton wave function

$$\Psi_S(\mathbf{r}_e, \mathbf{r}_h) = \sum_{vc\mathbf{k}} A^S_{vc\mathbf{k}} \psi_{c\mathbf{k}}(\mathbf{r}_e) \psi^*_{v\mathbf{k}}(\mathbf{r}_h), \tag{4.1}$$

where $\psi_{v(c)\mathbf{k}}(\mathbf{r}_{h(e)})$ are single-particle DFT Kohn-Sham wave functions for the electrons and holes, and $A^S_{vc\mathbf{k}}$ are coefficients corresponding to the excitonic state S, calculated directly from the BSE. The excitonic wave function defined by equation 4.1 is computed on an $8 \times 8 \times 8$ supercell, a sufficiently large real-space supercell to accommodate the entire wave function and ensure convergence. To visualize the excitonic wave function in real-space, one needs to fix the position of the hole. For $Cs_2AgSbBr_6$, $\Psi_S(\mathbf{r}_e, \mathbf{r}_h = \mathbf{r}(\mathrm{Sb})) \simeq \Psi_S(\mathbf{r}_e, \mathbf{r}_h = \mathbf{r}(\mathrm{Ag}))$, so Figure 4.3 c) shows the resulting excitonic wave function by summing over these two hole positions, while for all the other systems, $\Psi_S(\mathbf{r}_e, \mathbf{r}_h = \mathbf{r}(\mathrm{B^{III}})) \gg \Psi_S(\mathbf{r}_e, \mathbf{r}_h = \mathbf{r}(\mathrm{Ag}))$, and Figure 4.3 a), b) and d) shows the excitonic wave function when the hole is fixed on a B^{III} ion site. The extent of the excitonic wave function can be qualitatively approximated by analysing the coefficients $A^S_{vc\mathbf{k}}$ from equation 4.1. More than 85% of the excitonic wave function is confined within only one B^{III}-centered octahedron and comprised of VBM → CBM transitions at the lowest direct gap with anisotropic orbital character, highlighting the heterogeneous nature of these excitons. Note that, $Cs_2AgSbBr_6$ does not follow the same trend, featuring an exciton extended at over at least three octahedra.

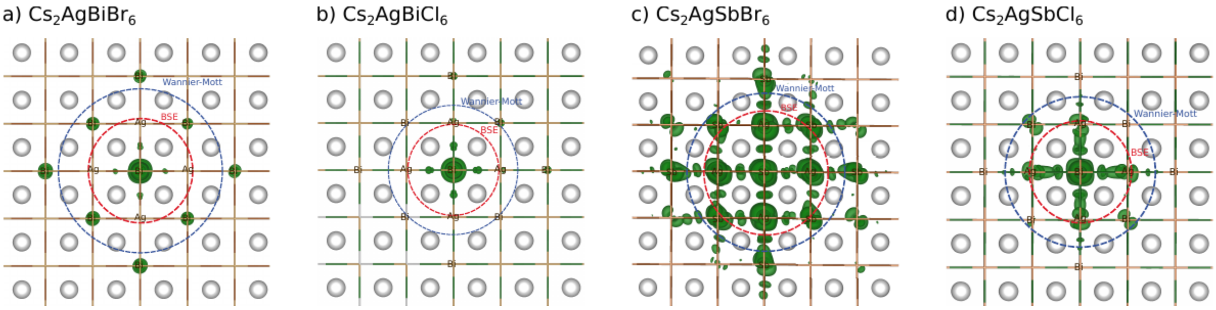

Figure 4.3: 3D representation of the probability density of the exciton wave function in real-space for a) $Cs_2AgBiBr_6$; b) $Cs_2AgBiCl_6$; c) $Cs_2AgSbBr_6$ and d) $Cs_2AgSbCl_6$. An isosurface containing 95% of the excitonic wave function is plotted. The red circles represent the average electron-hole separation as computed with BSE, while the blue circles show the average electron-hole separation if the exciton nature would have been hydrogenic. The silver spheres are Cs.

In order to quantitatively describe the spatial extent of the exciton, we employ a similar approach as in Ref. [35] and define the electron–hole correlation function

$$F_S(\mathbf{r}) = \int_\Omega d^3\mathbf{r}_h |\Psi_S(\mathbf{r}_e = \mathbf{r}_h + \mathbf{r}, \mathbf{r}_h)|^2, \tag{4.2}$$

which renders the probability of finding the electron-hole pair separated by the vector $\mathbf{r} = \mathbf{r}_e - \mathbf{r}_h$. We compute the integral as a discrete sum over three different hole positions $\mathbf{r}_h$ (hole fixed on a B^{III} ion site – $\mathbf{r}_h = \mathbf{r}(B^{III})$, hole fixed on a Ag ion site – $\mathbf{r}_h = \mathbf{r}(Ag)$ and hole fixed on a halide ion site – $\mathbf{r}_h = \mathbf{r}(X)$) and over the first bright transition. To approximately account for the symmetry and finite number of hole positions, we introduce the weight w_h and normalize $F_S(\mathbf{r})$ with respect to its cumulative sum

$$F_S(\mathbf{r}) = \frac{\sum_h \left(|\Psi_S(\mathbf{r}_e = \mathbf{r}_h + \mathbf{r}, \mathbf{r}_h)|^2 \cdot w_h\right)}{\sum_{e,h} \left(|\Psi_S(\mathbf{r}_e, \mathbf{r}_h)|^2 \cdot w_h\right)}, \tag{4.3}$$

where $w_h = \begin{cases} 6 & \text{for } \mathbf{r}_e = \mathbf{r}(X) \\ 1 & \text{otherwise} \end{cases}$. Using the distribution function defined by the expression 4.3, we compute the average electron-hole separation

$$\sigma_\mathbf{r} = \sqrt{\langle|\mathbf{r}|^2\rangle - \langle|\mathbf{r}|\rangle^2}, \tag{4.4}$$

where $\langle|\mathbf{r}|^n\rangle = \int_\Omega d^3\mathbf{r}|\mathbf{r}|^n F_S(\mathbf{r})$ is the n-th moment of the electron-hole correlation function $F_S(\mathbf{r})$ and Ω the volume of the supercell, and use it to quantify the degree of localization of the excitonic wave function. As showed in Table 4.2, the high localization of the excitonic wave function is another common feature of the studied compounds, but surprisingly, the average electron-hole separation does not follow the linear trend described by the binding energies. Precisely, as showed in Figure 4.7, the Cl-based double perovskites exhibit the strongest localization, while $Cs_2AgSbBr_6$ exhibits the most delocalized exciton, although its exciton binding energy is significantly higher than that of $Cs_2AgBiBr_6$ (247 meV vs 170 meV). This finding can be explained based on the spatial extent of the electronic states from which the CBM is derived. Figure 4.4 shows that the average electron-hole separation scales with the fractional contribution of the B^{III} p character of the CBM and demonstrates that the reduced Sb p character of the CBM of $Cs_2AgSbBr_6$ (see Figure 3.11 b)) leads to the delocalization of the excitonic wave function.

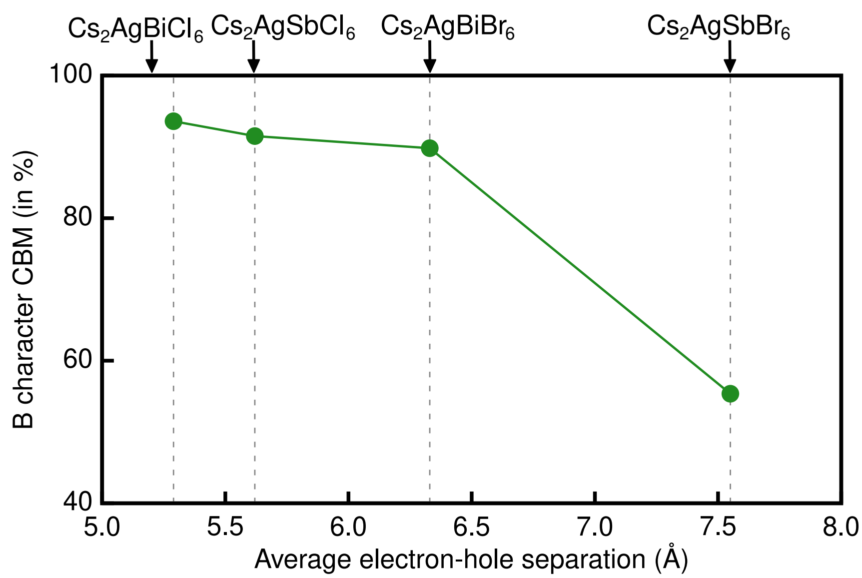

Figure 4.4: Percentage B^{III} orbital character of the CBM with respect to average electron-hole separation as computed by solving the BSE.

4.3. Elliott Theory

Experimental analysis of optical absorption spectra with excitonic features often relies on Elliott theory [281], a standard phenomenological theory of hydrogenic excitons in solids, typically used to extract exciton binding energies and band gaps from experimental optical absorption spectra. Within this theory, the absorption coefficient is given as the sum of contributions from bound excitonic states and continuum states:

$$\alpha(E) = \alpha_x(E) + \alpha_C(E). \tag{4.5}$$

The contribution from bound excitonic states $\alpha_x(E)$ has the form of a line series at energies E_x/n^2 below the band gap E_{gap}, with the magnitude inverse proportional with n^3

$$\alpha_x(E) = b_0 \frac{|\langle\Psi_c| P |\Psi_v\rangle|^2}{E} \sum_{n=1}^{\infty} \frac{4\pi E_x^{3/2}}{n^3} \delta\left(E - \left(E_{gap} - \frac{E_x}{n^2}\right)\right), \tag{4.6}$$

while the absorption associated with continuum states has the form

$$\alpha_C(E) = \xi(E)\alpha_{Free}(E), \tag{4.7}$$

where ξ is the Coulombic enhancement factor, due to the Coulombic attraction between the unbound electrons and holes in the continuum and it is given by

$$\xi = \frac{2\pi\sqrt{\frac{E_x}{E-E_{gap}}}}{1 - \exp\left(-2\pi\sqrt{\frac{E_x}{E-E_{gap}}}\right)}. \tag{4.8}$$

When the Coulombic interactions are fully screened, the exciton binding energy tends towards zero and the free electron-hole absorption reads

$$\alpha_{Free}(E) = b_0 \frac{|\langle\Psi_c| P |\Psi_v\rangle|^2}{E} c_0^{-1} JDoS(E), \tag{4.9}$$

where b_0 is a proportionality constant and the joint density of states (JDoS) is given by JDoS(E) $= \begin{cases} c_0\sqrt{E - E_{gap}} & \text{if } E > E_{gap} \\ 0 & \text{otherwise} \end{cases}$ with the constant $c_0 = \frac{1}{(2\pi)^2}\left(\frac{2\mu}{\hbar^2}\right)^{3/2} \times 2$. With these expressions, the total absorption coefficient can be written as the sum of bound excitonic (below gap) absorption and free (screened) electron-hole absorption, multiplied by the Coulombic enhancement factor

$$\begin{aligned} \alpha(E) = b_0 \frac{|\langle\Psi_c| P |\Psi_v\rangle|^2}{E} \Bigg(&\sum_{n=1}^{\infty} \frac{4\pi E_x^{3/2}}{n^3} \delta\left(E - \left(E_{gap} - \frac{E_x}{n^2}\right)\right) \\ &+ \frac{2\pi\sqrt{\frac{E_x}{E-E_{gap}}}}{1 - \exp\left(-2\pi\sqrt{\frac{E_x}{E-E_{gap}}}\right)} c_0^{-1} JDoS(E)\Bigg). \end{aligned} \tag{4.10}$$

In order to analyse the computed absorption spectra with the Elliott theory, the BSE optical absorption spectra of the $Cs_2AgB^{III}X_6$ (B^{III}=Bi, Sb; X=Br, Cl) perovskites have been fitted with the Elliott formula from equation 4.10, from 0.2 eV below the onset, up to 1.2 eV above the onset via the fitting parameters b_0, $|\langle\Psi_c| P |\Psi_v\rangle|^2$, E_{gap}, E_x. In order

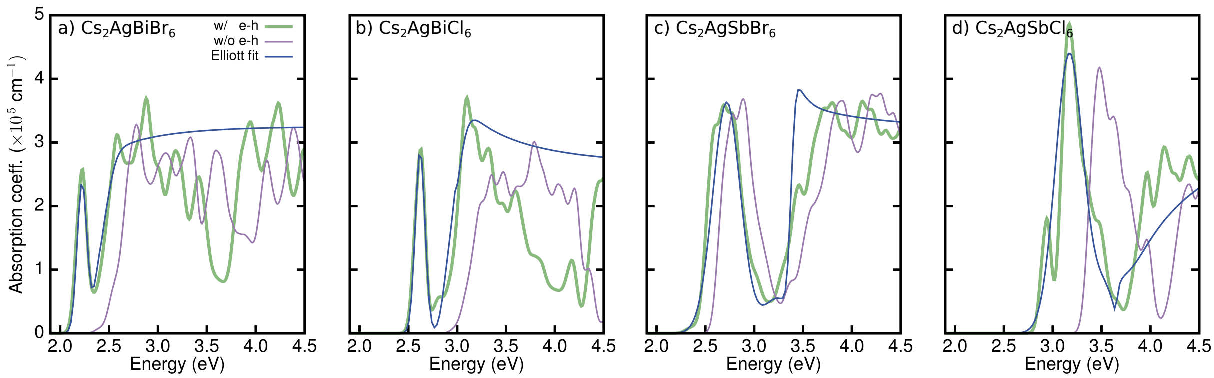

Figure 4.5: Optical absorption spectrum of a) $Cs_2AgBiBr_6$; b) $Cs_2AgBiCl_6$; c) $Cs_2AgSbBr_6$ and d) $Cs_2AgSbCl_6$, where the RPA spectrum is represented in purple, the BSE spectrum in green and the Elliott fit in blue.

to obtain a smooth spectrum, the absorption coefficient $\alpha(E)$ has been convoluted with a Gaussian function $g(x) = \dfrac{1}{\sigma\sqrt{2\pi}} \exp\left(-\dfrac{x^2}{2\sigma^2}\right)$, with line broadening σ.

As shown in Figure 4.5, the Elliott model fails to describe optical absorption lineshapes for this entire family of double perovskites. More precisely, for the Sb-based perovskites, Elliott theory does not predict the correct onset of the continuum region (see Figure 4.5 c) and d)), while for the Bi-based perovskites the exciton binding energy estimated with Elliott model falls within the same order of magnitude, but is at least 35 % higher than the BSE results. This observation is not unexpected, given that the Elliott formula for optical absorption coefficient in the presence of bound electron-hole states is derived for a direct band gap semiconductor with parabolic band edges, and weakly Wannier-Mott-like excitons. Furthermore, this overestimation of the computed binding energy illustrates that Elliott theory does not fully capture the nature of electron-hole interactions in this system, and that the excitons do not obey the hydrogenic Wannier-Mott model [284].

4.4. Wannier-Mott model

The hydrogenic model of Wannier and Mott [284] is a conventional model typically employed for the description of hydrogenic excitons in inorganic semiconductor crystals with small energy direct gaps, parabolic band edges, isotropic effective masses and high dielectric constant [285]. We assess the nature of the excitons in the $Cs_2AgB^{III}X_6$ (B^{III}=Bi, Sb and X=Br, Cl) double perovskites by comparing the first principles results with the exciton binding energy predicted by the Wannier-Mott model.

Within the hydrogenic model, the exciton binding energy is defined as

$$E_x = \frac{1}{n^2}\frac{\mu}{m_e \varepsilon_\infty^2} R_H, \tag{4.11}$$

where R_H is the Rydberg constant, m_0 is the electron rest mass and the values of the reduced effective mass of the exciton μ and the static dielectric constant ϵ_∞ are obtained from the G_0W_0 calculations. As previously showed in section 3.4.2, extremely low dispersion of the VBM at L (CBM at X) introduces a large uncertainty in the calculation of the hole (electron) effective mass of $Cs_2AgSbCl_6$ ($Cs_2AgBiBr_6$, $Cs_2AgBiCl_6$ and $Cs_2AgSbCl_6$). As consequence, for $Cs_2AgBiBr_6$, $Cs_2AgBiCl_6$ and $Cs_2AgSbCl_6$, μ is approximated with the orientationally-averaged hole effective mass, while in the case of $Cs_2AgSbBr_6$, the reduced mass is computed as the averaged electron effective mass.

Table 4.3: Exciton binding energies (in meV) of the two lowest energy bright states as calculated with G_0W_0@LDA+BSE (E_x^{BSE}) and the Wannier-Mott model (E_x^{WM}), and the deviation (in %) of the Wannier-Mott predicted binding energy with respect to the BSE value.

	n	E_x^{BSE} **(meV)**	E_x^{WM} **(meV)**	**Deviation**
$Cs_2AgBiBr_6$	1	170	120	29 %
	2	93	30	68 %
$Cs_2AgSbBr_6$	1	247	112	55 %
	2	145	28	81 %
$Cs_2AgBiCl_6$	1	333	205	38 %
	2	141	51	64 %
$Cs_2AgSbCl_6$	1	434	193	55 %
	2	243	48	80 %

Table 4.3 reports exciton binding energies of the two lowest energy bright states as calculated with G_0W_0+BSE and the Wannier-Mott model and demonstrates the non-hydrogenic nature of the exciton in the studied double perovskites. The Wannier-Mott model predicts, for the first bright excited state, a binding energy at least 30 % lower than the first principles result. Furthermore, the energy of the second excited state as computed with G_0W_0+BSE deviates significantly from the hydrogenic Rydberg series, being at least three times larger than the Wannier-Mott binding energy.

Figure 4.6 further demonstrates the non-hydrogeneity of excitons in these compounds by showing the large underestimation of the Wannier-Mott model with respect to the first principles binding energies. Similar with the G_0W_0+BSE calculations, the Wannier-Mott model predicts a linear dependence of the binding energy on the lowest direct band gap. However, the slope is significantly different and the deviation from the BSE results increases with the increase of the absolute value of the binding energy.

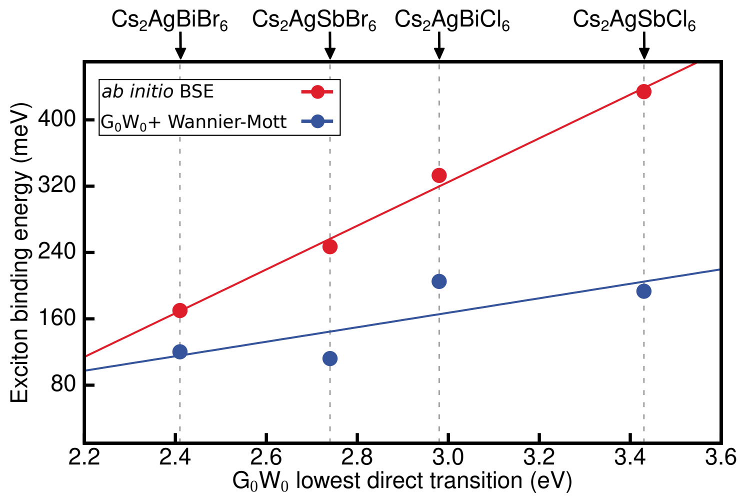

Figure 4.6: Variation of the exciton binding energy as computed within the BSE approach (red) and the Wannier-Mott model (blue) with respect to the G_0W_0 lowest direct band gap. The computed values are represented by solid points, while the solid lines are a guide to the eye, representing the linear fit of the points.

As described in section 4.2 and expected in the case of excitons with large binding energy, they are highly-localized within the crystal structure (see Figure 4.7). Moreover, the Wannier-Mott model systematically overestimates the average electron-hole separation by more than 20 % ($\sigma_{\mathbf{r}}^{\mathrm{WM}} = \frac{\sqrt{3}}{2} a_H$, where a_H is the Bohr radius). However, as showed in Figure 4.7 and discussed in section 4.2, the degree of localization does not follow the linear trends expected from the calculations of the binding energies, with $Cs_2AgSbBr_6$ featuring the most delocalized exciton.

The disagreement between the Wannier-Mott model and the first principles results is due to the localization of electrons and holes in chemically distinct octahedra, resulting in an anisotropic QP band structure of these halide double perovskites, that give rise to an anisotropy of the reduced mass and noticeable local field effects in the dielectric function. In the following these effects will be analysed in detail.

4.4.1. Anisotropy of the reduced masses

The anisotropy of the effective mass tensor is quantified by the anisotropy factor λ as defined in Ref. [286]:

$$\lambda = \left(\frac{m_\perp}{m_\parallel}\right)^{1/3} = \begin{cases} \to 1 & m_\perp = m_\parallel, \text{ i.e. fully isotropic effective mass} \\ > 1 & m_\parallel < m_\perp \\ < 1 & m_\parallel > m_\perp \end{cases} \tag{4.12}$$

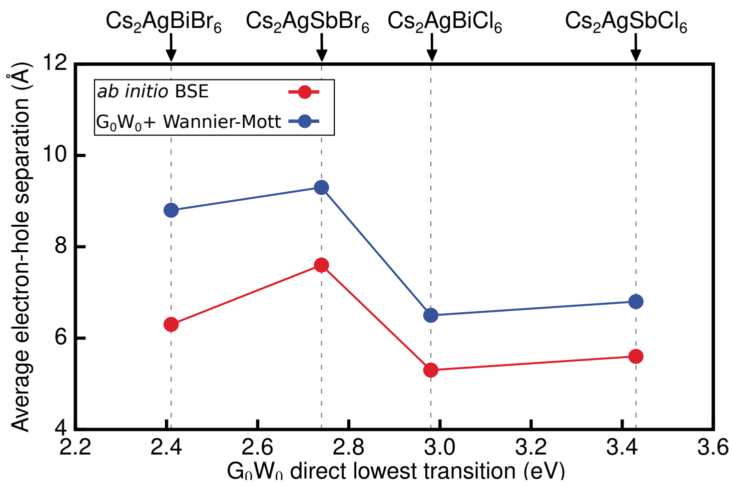

Figure 4.7: Average electron-hole separation as computed with BSE (red) and as predicted by the Wannier-Mott model (blue) with respect to the G_0W_0 lowest direct band gap.

where $m_{\perp} = \dfrac{2m_{h_1}m_{h_2}}{m_{h_1}+m_{h_2}}$ is the harmonic mean of the transverse hole effective masses and $m_{\parallel} = m_{h_3}$ is the longitudinal hole effective mass.

Table 4.4 shows that the hole effective mass is highly anisotropic, with the longitudinal component at least 4 times smaller than the transverse components. The light longitu-

Table 4.4: Hole effective masses of $Cs_2AgBiBr_6$, $Cs_2AgBiCl_6$, $Cs_2AgSbCl_6$ and electron effective mass of $Cs_2AgSbBr_6$ at the band edges corresponding to the lowest direct transition (in units of the electron rest mass m_0, expressed in a reference frame where the effective mass tensor is diagonal), the anisotropy factor λ, as computed with G_0W_0@LDA and exciton binding energy (in meV) as computed within the G_0W_0+BSE approach (E_x^{BSE}), the Wannier-Mott model (E_x^{WM}) and the Wannier-Mott model corrected for the effective mass anisotropy $E_x(\lambda)$.

	$\mathbf{m}_{h_1}$	$\mathbf{m}_{h_2}$	$\mathbf{m}_{h_3}$	$\mathbf{m}_h^*$	λ	$\mathbf{E}_x^{BSE}$	E_x^{WM}	$\mathbf{E}_x(\lambda)$
$Cs_2AgBiBr_6$	0.72	0.67	0.15	0.31	1.67	170	120	148
$Cs_2AgBiCl_6$	0.75	0.56	0.17	0.33	1.57	333	205	240
$Cs_2AgSbCl_6$	0.96	0.71	0.15	0.32	1.77	434	193	250
	$\mathbf{m}_{e_1}$	$\mathbf{m}_{e_2}$	$\mathbf{m}_{e_3}$	$\mathbf{m}_e^*$				
$Cs_2AgSbBr_6$	0.33	0.30	0.26	0.29	1.07	247	112	113

dinal hole effective mass originates from the very disperse valence band along X to Γ. Qualitatively, we find that the deviation between the exciton binding energy computed with first principles and the one predicted by the Wannier-Mott model is direct proportional with the anisotropy of the hole effective mass. However, this observation is not valid for $Cs_2AgSbBr_6$, for which the Wannier-Mott exciton binding energy is dictated by the almost isotropic electron effective mass, corresponding to the lowest direct transition at L.

Following the approach described by Schindlmayr in Ref. [286], namely taking into account the effect of the effective mass anisotropy the corrected Wannier-Mott binding energy becomes

$$E_x(\lambda) = -3\left(\frac{1}{\varepsilon_\infty}\right)^2 \left(\frac{2}{m_\perp} + \frac{1}{\lambda^2 m_\parallel}\right)^{-1} \left(\frac{\operatorname{arcsinh}\sqrt{\lambda^2-1}}{\sqrt{\lambda^2-1}}\right)^2 R_H. \tag{4.13}$$

As shown in Table 4.4, the inclusion of the effective mass anisotropy in the hydrogenic model reduces the discrepancy between the first principles results and the Wannier-Mott exciton binding energy. Furthermore, the correction to the isotropic Wannier-Mott model increases with increasing anisotropy factor and the remaining difference can be attributed to the local field effects and the non-parabolicity of the band edges.

4.4.2. Local field effects in the dielectric function

The first principles approach allow us to further disentangle the limitations of the Wannier-Mott model, by transforming the full dielectric matrix in a simplified isotropic dielectric matrix with static dielectric constant on the diagonal, i.e. $\epsilon(\mathbf{r}, \mathbf{r}'; \omega) = \varepsilon_\infty$. This change not only suppresses the local field effects, but also leads to a uniform dielectric matrix. This modification results in a red-shift of the absorption spectrum with electron-hole interactions, leading to an underestimation of the exciton binding energy with respect to the first principles result by at least $\sim$20 % (see Table 4.5). Furthermore, we note that the stronger the exciton is bound, the larger the local field effects are.

Table 4.5: BSE exciton binding energies (in meV) as computed with the full and uniform (ε_∞) dielectric matrix and the deviation (in %) of the former with respect to the latter.

	$\mathbf{E}_x^{BSE}$ (meV)		Deviation
	$\epsilon(\mathbf{r}, \mathbf{r}'; \omega)$	$\epsilon(\mathbf{r}, \mathbf{r}'; \omega) \to \varepsilon_\infty$	
$Cs_2AgBiBr_6$	170	99	42 %
$Cs_2AgSbBr_6$	247	158	36 %
$Cs_2AgBiCl_6$	333	231	31 %
$Cs_2AgSbCl_6$	434	348	20 %

Figure 4.8 shows the imaginary part of the dielectric function computed with and without local field effects. The inclusion of local field effects leads to a significant suppression of the spectrum without electron-hole interactions, behaviour also reported in previous studies [287, 288].

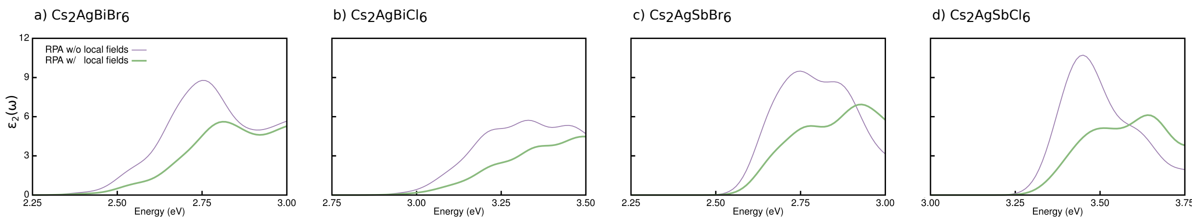

Figure 4.8: Imaginary part of the dielectric function as calculated within RPA with (green) and without (purple) local field effects for a) $Cs_2AgBiBr_6$, b) $Cs_2AgBiCl_6$, c) $Cs_2AgSbBr_6$ and d) $Cs_2AgSbCl_6$.

4.5. Excitonic properties of $Cs_2AgInCl_6$ double perovskite

Optical properties of $Cs_2AgInCl_6$ double perovskite have been studied both experimentally [254, 258, 262, 289] and theoretically [230, 258]. Han et al. showed in Ref. [289] that the weak absorption peak at the onset of the optical spectrum is a consequence of the parity-forbidden direct transition at Γ. This finding is in line with the pioneering computational work by Luo et al. that reported the existence of an optically inactive feature with an exciton binding energy of 250 meV [230]. However, to the best of our knowledge, there is no quantitative information about the binding energy of the bright excitonic state originating from near Γ allowed transitions. Motivated by this lack of detailed analysis, as well as intrigued by the more delocalized electronic structure of the $Cs_2AgInCl_6$ double perovskite discussed in section 3.4, we employ the previously described G_0W_0+BSE approach to compute exciton binding energies and assess the nature of excitonic features.

Figure 4.9 shows that, similar with the case of Ag-pnictogen double perovskite family, including electron-hole interactions leads to a red-shift of the optical absorption G_0W_0+BSE spectrum with respect to the RPA spectrum, but contrary to the Ag-pnictogen family, $Cs_2AgInCl_6$ does not exhibit any pronounced excitonic feature. In line with previous results [230, 258], we find several optically inactive excitonic states (marked with D) originating from parity-forbidden direct transitions at Γ point in the Brillouin zone. However, our computed exciton binding energy of 180 meV for the dark state is 70 meV smaller than that reported by Luo et al. in Ref. [230] and can be explained based on the different structures and methodologies adopted: Ref. [230] employs a partial GW_0 self consistent scheme that is known to open up the QP band gap and as a consequence it might also affect the static dielectric constant, and reports extrapolated binding energies. We find that the group of dark excitonic states is followed by three degenerate bright states (marked with B), centered at 48 meV lower than the direct band gap. Our calculations show that these bright excitons originate from allowed transitions at points around Γ, that are only 8 meV larger, suggesting that, even though parity-forbidden, the fundamental band gap of $Cs_2AgInCl_6$ could still be defined as the optical gap. This result, along with the low exciton binding energy, the direct band gap and improved stability under ambient conditions render $Cs_2AgInCl_6$ double perovskite as a potential contender for optoelectronic applications.

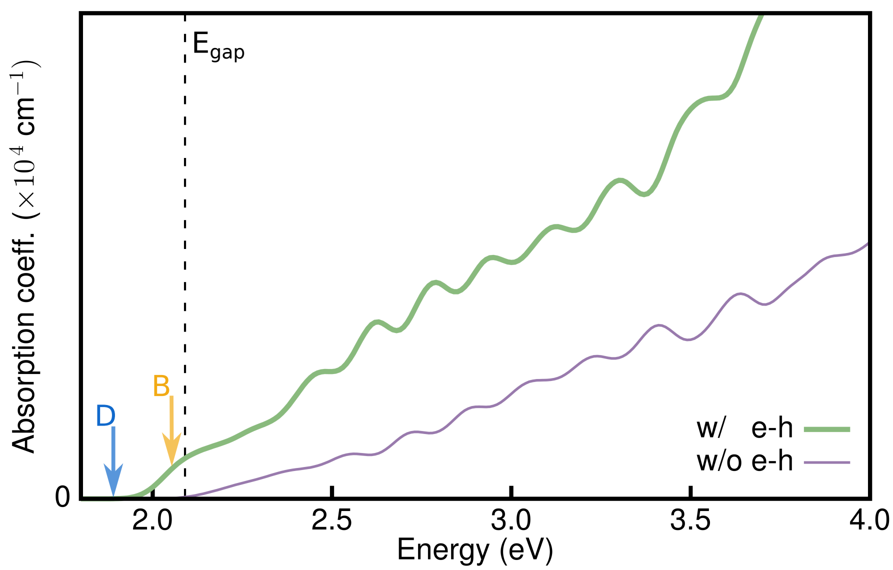

Figure 4.9: Optical absorption spectra of cubic $Fm\bar{3}m$ phase of $Cs_2AgInCl_6$ calculated using RPA without local field effects (purple) and the G_0W_0+BSE approach (green). The first dark and first bright excitonic states are marked by a blue arrow labeled D and an orange arrow labeled B, respectively.

To assess the effect of the B^{III}-site chemical composition on the nature of the excitonic states, we compare our computed BSE exciton binding energy with the one predicted by the Wannier-Mott model using the formula 4.11. Contrary to the case of Ag-pnictogen double perovskites, where one of the effective masses was ill-defined due to the lack of band dispersion, in the case of $Cs_2AgInCl_6$ both electron and hole effective masses at the band edges corresponding to lowest energy direct transition are well-defined. Therefore, the reduced mass μ of $Cs_2AgInCl_6$ was computed as the average between the hole and electron effective masses at the Γ point:

$$\frac{1}{\mu} = \frac{1}{m_e^*} + \frac{1}{m_h^*}, \tag{4.14}$$

where the hole effective mass m_h^* was calculated as described in section 3.4.2. Table 4.6 shows that the Wannier-Mott predicted binding energy of the first optically inactive excited state is in exceptionally good agreement with the G_0W_0+BSE computed energy, revealing an underestimation of only 5 % . However, the Wannier-Mott prediction for the second excited state deviates significantly from our computed binding energy, highlighting the deviations from the Wannier-Mott model.

Table 4.6: Exciton binding energies (in meV) of the first two lowest energy dark states as calculated with G_0W_0+BSE (E_x^{BSE}) and the Wannier-Mott model (E_x^{WM}) and the deviation (in %) of the Wannier-Mott predicted binding energy with respect to the BSE value.

	n	E_x^{BSE} (meV)	E_x^{WM} (meV)	Deviation
$Cs_2AgInCl_6$	1	180	189	5 %
	2	75	47	37 %

While the non-hydrogenic character of the excitonic features in the Ag-pnictogen family was linked to anisotropy of the reduced mass and sizeable local field effects in the dielectric function (see section 4.4), our studies reveal that none of those play a significant role in the case of $Cs_2AgInCl_6$ double perovskite. As previously demonstrated in section 3.4.2, despite the rock-salt packing of the crystal, with alternating Ag- and In-centered octahedra, both electron and hole effective masses are highly isotropic. Furthermore, repeating G_0W_0+BSE calculations with uniform dielectric matrix $\varepsilon(\mathbf{r}, \mathbf{r}'; \omega) = \varepsilon_\infty$, we find that the excitonic transitions are almost unaffected, with the energy of the first dark excited state decreasing by ~10 meV and that of higher excitonic states by less than 1 meV. We attribute this particular behaviour to the fundamentally different orbital character at the band edges of $Cs_2AgInCl_6$ direct band gap double perovskite, in particular to the diffuse s orbitals making up the CBM at and around Γ point.

Chapter 5

Halogen migration in all-inorganic $CsPbBr_3$ perovskite

Lead-halide perovskites have been one of the main focuses of the photovoltaics community for over a decade due to their exceptional semiconducting properties, facile tunabiliy through compositional engineering and power conversion efficiency exceeding 25 % [8]. This class of materials have been extensively used as active layers in photovoltaic solar cells [170, 290, 291], light-emitting diodes (LEDs) [292, 293], photo-detectors [294–296] and X-ray scintillators [297]. In recent years, remarkable efforts have been made to improve the perovskite-based optoelectronic devices via encapsulation [298] and passivation of the perovskite layer [299], as well as (partial) replacement of the A-site cation [189]. However, lead-halide perovskites continue to be unstable towards moisture, oxygen, light, heat, and electric fields [13], leading to a halt in commercialisation. Although believed to be more stable, even all-inorganic halide perovskites are unstable under strong electric fields [193].These poor characteristics of both organic-inorganic and all-inorganic halide perovskites are presumably a result of point defects [11, 300–302], which facilitate migration of mobile ionic species, especially at the grain boundaries and surfaces of single crystals [303], leading to material degradation and phase separation [304].

The mechanism of the defect-mediated ion migration has been extensively studied both theoretically, using first principles calculations [88–90, 305–308], and experimentally [88, 185, 309–312]. Furthermore, various reports showed that the halide ions are the most mobile species [89, 261, 313, 314]. For example, Eames et al. [88] and Meloni et al. [89] experimentally determined the migration barriers in $MAPbI_3$-based solar cell and proved that halides are the main migration species in halide perovskite devices. Despite the large number of studies, the activation energy for these migration processes is still under debate, with computed values spanning about one order of magnitude. However, they consistently predict the halogen migration as the primary channel for the ionic conductivity observed in halide perovskites [88–90, 306, 307, 313, 315].

While the majority of the mentioned studies focused on hybrid organic-inorganic perovskites [88, 89, 91], recently the interest in all-inorganic $CsPbX_3$ halide perovskites was on the rise due to their very high photoluminescence quantum yields, with band gap energies and emission spectra tunable over the entire visible spectral region [191]. Kang et al. conducted a theoretically study of intrinsic point defects in $CsPbBr_3$ and predicted that the halides are the most mobile species among the 12 point defects analysed [316]. Zhang et al. [186] demonstrated by means of *ab initio* calculations that the migration path of halide atoms presents small deviation from the linear route and observed good agreement with activation energy determined by temperature dependent conductivity measurements [309, 310].

Even though all the studies mentioned above have focused on ion migration in the bulk, the importance of the surfaces in the ion migration process is expected to increase with the decrease in the size of perovskite nanocrystals. Furthermore, Xing et al. demonstrated in Ref [317] that measured activation energies obtained by Arrhenius fitting of conductivity data in the dark significantly increases with grain size, leading to an increasingly difficult ion migration in large crystals, while Yun et al. showed that the ion migration process is dominant at grain boundaries, using Kelvin probe force microscopy [318].

Recently, the effect of both surfaces and grain boundaries have been analysed using theoretically approaches as first principles calculations [90, 91]. And while Meggiolaro et al. showed in Ref. [91] that the migration barriers of interstitial halide vacancies are almost unaffected by the presence of surfaces, Oranskaia et al. [90] demonstrated that the surface decrease the migration barrier of Br both vacancies and interstitials in $MAPbBr_3$ and $FAPbBr_3$ by at least 0.2 eV. Furthermore, as shown in Ref. [90], the migration barriers in hybrid organic-inorganic perovskites are additionally influenced by the orientation of the organic cation. However, DFT studies analyse ion migration process in fixed structural models. The neglect of the rotations of the organic cation at room and higher temperatures leads to significant differences in the potential energy landscape depending on the choice of molecular orientation [319]. Motivated by this uncertainty in constructing a suitable structural model of the hybrid organic-inorganic perovskites, corroborated with the increasingly important role of surfaces in all-inorganic halide perovskite nanocrystals, we focus on the ion migration process in the bulk and at the surface of $CsPbBr_3$.

In this chapter we analyse the vacancy-mediated bromine migration process in fully inorganic lead-halide perovskite $CsPbBr_3$, by means of first principles DFT calculations. Even though $CsPbBr_3$ is orthorhombic with $Pbnm$ symmetry at RT, we focus on the highly symmetric cubic high temperature crystal structure with $Pm\bar{3}m$ symmetry [187] and assess the open question of the influence of the surface on the vacancy-related bromine migration process. Moreover, we study the impact of surface passivation with alkali-halide monolayers on the migration barrier. We published the results presented in this chapter in Ref. [320].

5.1. Surface slab construction

To study how the presence of a surface impacts the halide migration process we constructed three systems with different dimensionality, i.e. a bulk and two (001) surface slab supercells featuring different terminations – surface A is $PbBr_2$-terminated, while surface B is CsBr-terminated. Figure 5.1 shows a schematic representation of our computational setup.

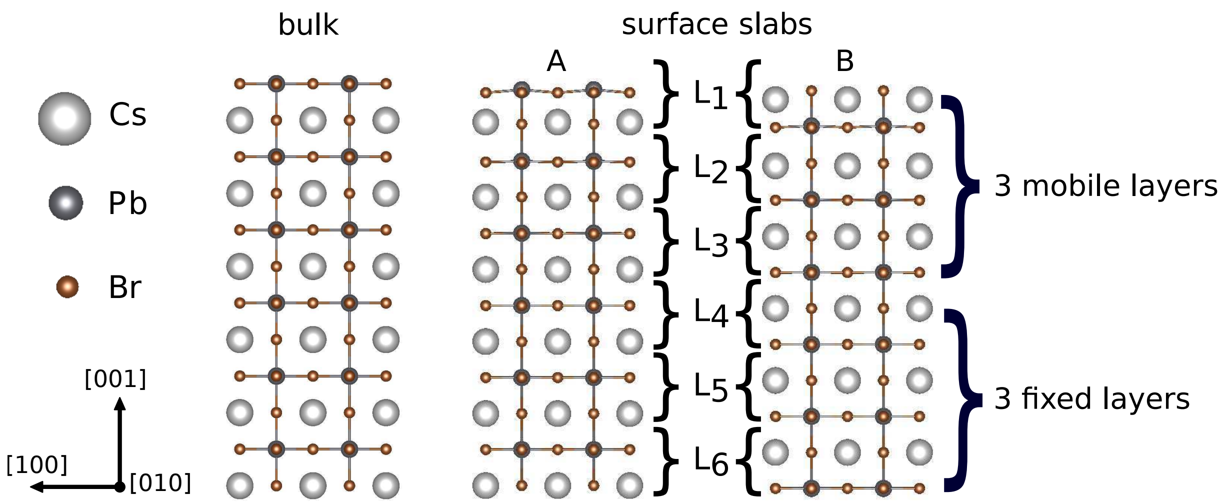

Figure 5.1: Bulk and slab supercells with A ($PbBr_2$) and B (CsBr) terminations. The label L_i ($i = 1 - 6$) enumerates layers in the slab structure. Surface slabs are separated by 30 Å of vacuum along the [001] direction.

The surface slab supercells are constructed by repeating the PBEsol-optimized primitive unit cell of $Pm\bar{3}m$ $CsPbBr_3$ twice along [100] direction, once along the [010] direction and six times along the out-of-plane [001] direction, yielding $2 \times 1 \times 6$ slab unit cells. A vacuum layer of 30 Å has been introduced along [001] direction and the bottom three layers fixed to the bulk positions, while the top three remained fully mobile. We construct a bulk system with the same number of layers (without vacuum) to facilitates the comparison with the slab supercells, having the same defect concentrations and in-plane boundary conditions. However, this specific setup (with asymmetric unit cells) is not suitable for direct comparison with neither experimental results nor bulk calculations of halide migration in symmetric structural models presented in Ref. [186, 308]. Therefore, we extend our study to a $2 \times 2 \times 6$ A-terminated surface slab and the corresponding bulk model. A detailed description of the bulk geometry optimization, slab construction and various tests showing the validity of the results can be found in Appendix A.4.

5.2. Structural changes upon vacancy formation

As a first step towards computing the migration barrier, we perform structural optimization for all structures shown in Figure 5.1. While the bulk system remains unaffected by further geometry optimization, the slab structure is compressed at the surface, with shorter axial (out-of-plane) $Pb - Br$ bonds and almost unchanged equatorial (in-plane) bonds. This effect is clearly visible in Figure 5.3 a) that shows the average relative variation of $Pb - Br$ bonds per layer as compared to the bulk $Pb - Br$ bond length of 2.93 Å.

Kang et al. showed in Ref. [316] that under Br-poor conditions, the formation of a halide related vacancy is favoured over all possible point defects. Therefore, in the next step, we analyse the effect of the creation of a bromine vacancy in each layer of the slab system. Generally, a Br vacancy can occupy two symmetry-inequivalent positions in a surface slab: axial and equatorial. However, due to the asymmetry of the $2 \times 1 \times 6$ unit cell, the equatorial positions are not equivalent in our setup. Figure 5.2 illustrates that the creation of a vacancy leads to slightly different bond lengths depending on whether the vacancy is introduced along [100] or [010] direction. Furthermore, these three inequivalent vacancy positions have different energies in the bulk model as well, which is also an artifact of the asymmetric unit cell.

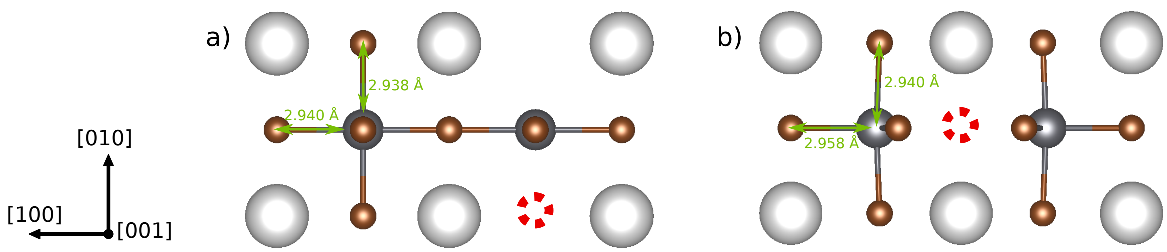

Figure 5.2: Top view of the A-terminated surface with the equatorial Br vacancy highlighted in red. The green arrows mark $Pb - Br$ bond lengths and are labeled with the respective values.

To qualitative analyse of the energetic ordering of these possibilities, we compute the binding energy

$$E_B = E_f^{bulk} - E_f^{slab}, \tag{5.1}$$

where E_f^{bulk} and E_f^{slab} are the formation energies of a vacancy in the bulk and slab, respectively and are defined as the energy difference between the pristine and the defective system. The binding energy defined by the equation 5.1 quantifies by how much a vacancy prefers to bind to the surface as compared to the bulk, such that positive values represent favorable vacancy formation conditions. In agreement with findings for $MAPbI_3$ reported in Ref. [91], the results listed in Table 5.1 indicate that the surface is more prone to defects, with L_1 featuring the largest binding energy that converges towards zero in the subsurface layers. Assessing the differences between the two surface terminations, we find that the binding energy of the Br vacancy at A-terminated surface is ∼190 meV higher than at B-terminated surface, suggesting favorable vacancy formation at surface B. Moreover, the creation of a Br vacancy at the B surface is achieved by breaking one $Pb-Br$ bond, while the creation of a similar vacancy at the A surface implies the breaking of two $Pb-Br$ bonds. Considering this structural difference, we analyse the two different surface terminations separately in the following. The significantly larger binding energy of the vacancy along [010] as compared with the one for the other equatorial position is an artifact of the asymmetric $2 \times 1 \times 6$ unit cell setup. We note that migration between an axial and an equatorial position is the shortest possible migration path in the bulk and in subsurface layers. However, since our goal is to compare migration barriers in the bulk with those at the surface and elucidate trends, in the following we will only focus on the specific case of halide migration between two adjacent axial positions. Furthermore, the axial-to-axial migration allows for a straightforward comparison of migration paths in all layers of the supercell.

Table 5.1: Binding energies (E_B) in eV of Br vacancies to the surface (results obtained using the $2 \times 1 \times 6$ setup).

Position	**Layer**	**Termination**	E_B **(eV)**
axial	1	A	0.42
		B	0.23
	2	A	0.22
		B	0.23
	3	A	0.05
		B	0.02
equatorial along [100]	1	A	0.35
		B	0.15
equatorial along [010]	1	A	2.57
		B	2.43

Figure 5.3 b) and c) shows the average $Pb - Br$ bond length average variation with respect to that of the undistorted bulk system upon creating a Br vacancy and optimizing the geometry of the defective system. The introduction of a halide vacancy at A-terminated surface leads to severe distortions and sizeable contraction of the system, whereas the creation of a Br vacancy at B-terminated surface leads to a less distorted structure with smaller bond length variations. This large compression of more than 20 % in L_1 of A-terminated is another artifact of the asymmetric $2 \times 1 \times 6$ unit cell. As shown in Figure A.10 of the Appendix, the overall compression of a symmetric $2 \times 2 \times 6$ unit cell upon vacancy formation is smaller, with a relative bond length variation of 3.4 % in L_1 of surface A and similar trends for subsequent layers. Although the absolute value of the

bond length fluctuation upon introducing a halide vacancy in the subsurface layers differs, the variation of the axial bond length is ∼5 times larger than the variation of equatorial bonds. Furthermore, the compression of the slab system at the surface is considerably reduced when the Br vacancy is created in the deeper lying layers.

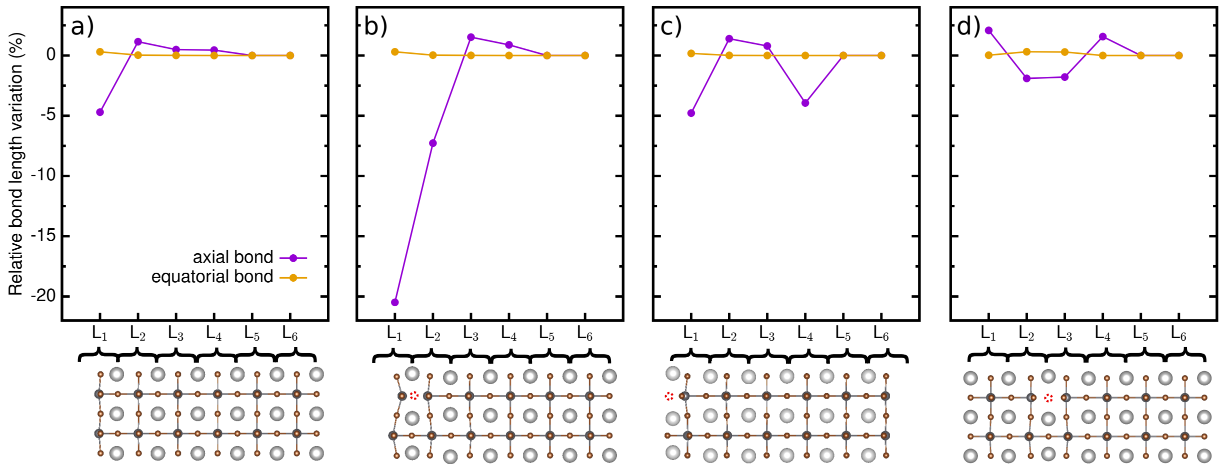

Figure 5.3: a) Relative variation of the bond lengths in the surface slab with respect to the undistorted bulk bond lengths. Relative bond length variation when a Br vacancy is introduced b) at A-terminated surface; c) at B-terminated surface; d) in the bulk. Each point represent the average over all axial and equatorial $Pb - Br$ bonds (per layer), respectively. The geometry optimized structure is shown below each panel, with the position of the Br vacancy highlighted in red.

Using the same approach, we studied the influence of vacancy creation within the bulk structure and find similar consequences. Figure 5.3 d) shows that the insertion of Br vacancy within the bulk leads to an appreciable compression in the vicinity of the vacancy. However, the more rigid bulk structure (with fewer degrees of freedom in comparison with the slab systems) leads to suppressed distortions and an overall negligible average variation of the bond lengths.

5.3. Br-mediated vacancy migration

In the final step, we simulate the in-plane migration process of a Br-mediated vacancy between two adjacent axial positions, using cNEB method. To asses the influence of the different surfaces, we compute the migration barrier energies for a vacancy migrating in the bulk system, at both A- and B-terminated surfaces and in the subsurface layers L_2 and L_3. As discussed in section 2.2, the migration energy is defined as the difference between the total energies of the initial and saddle points.

5.3.1. Bulk structure

The migration barrier of 0.65 eV computed for the $2 \times 1 \times 6$ bulk unit cell is in good agreement with the experimental values reported in the literature for cubic $CsPbBr_3$, ranging from 0.66 eV [309] to 0.72 eV [310]. Furthermore, the discrepancy of 40 meV between the migration energy reported by Zhang et al. in Ref. [186] and our result may be explained based on different approximations for the exchange correlation potential and phases of the $CsPbBr_3$ perovskite (Ref. [186] analyses orthorombic phase of $CsPbBr_3$, within the PBE approximation). Note that we systematically overestimate the migration barriers by neglecting the large, anharmonic vibrations reported for $CsPbBr_3$ at room and higher temperatures [321].

Figure 5.4 shows the profile of the migration energy of a Br vacancy in the $2 \times 1 \times 6$ bulk unit cell, along with the migration path. We link the almost straight path, with the rigid lattice of the bulk. The closely packed network does not permit noticeable restructuring of the lattice and force the migrating Br ion to move from one axial vacancy position to the other along the shortest possible path.

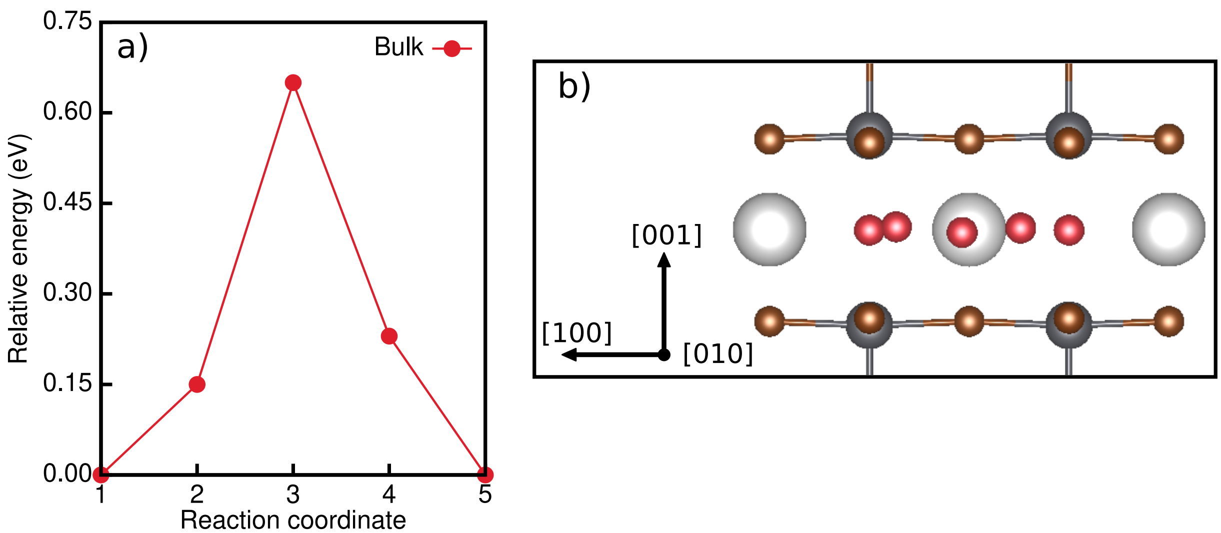

Figure 5.4: a) Energy profiles and b) migration paths for halide migration process within the bulk system. The structure corresponds to the average atomic configurations of the two equivalent endpoints of each cNEB calculation overlaid with the position of the migrating Br ion along the migration path.

5.3.2. Unpassivated slab structure

The migration barriers for a Br-mediated vacancy migration at A- and B-terminated surfaces and within the deeper lying layers of the $2 \times 1 \times 6$ slab supercell are reported in Table 5.2, showing the value corresponding to the bulk migration for comparison.

Table 5.2: Calculated energies (in eV) of Br vacancy migration across two adjacent axial Br positions, and deviation (in Å) from the straight migration path in $CsPbBr_3$ perovskite

System	Mobile layers	Termination	Layer	Migration energy (eV)	δ (Å)
bulk				0.65	0.13
slab	3	A	1	0.40	1.24
			2	0.29	0.94
			3	0.30	1.04
		B	1	0.31	0.77
			2	0.30	0.67
			3	0.30	0.70
slab	4	A	1	0.38	1.24
			2	0.26	1.04
			3	0.27	1.06
			4	0.29	1.10

As showed in figure 5.5, the energy barrier of a Br vacancy migrating within the bulk is substantially higher than that of a vacancy migration process at any of the two analysed surfaces. Furthermore, the migration energy at B-terminated surface is lower than half of that in the bulk structure, suggesting favorable vacancy-assisted diffusion of the halide ions at the surface. The computed migration barrier at A-terminated surface is 90 meV larger than that at B-terminated surface, in agreement with previous observations showing iodine vacancy clustering at MAI-terminated surfaces in $MAPbI_3$ [322]. Curiously, the computed migration barrier for a Br vacancy in subsurface layer L_2 is ∼110 meV lower than that directly at the surface and ∼55 % lower than that in the bulk. Moreover, the migration barrier in the deeper subsurface layers increases extremely slow and does not reach the value obtained for the vacancy migration within the bulk structure. We believe that this extremely slow convergence is an effect of our unit cell setup. As described in section 5.1, the bottom layers of the surface slab are fixed to the bulk positions. This constraint that introduces spurious strain in the structure the closer to the fixed layer, might affect the magnitude of the calculated migration barriers especially in the deeper lying layers. We therefore computed migration energies for an A-terminated surface slab with four mobile layers as well. The absolute values of the corresponding migration barriers reported in Table 5.2, are slightly lower but follow the same trend. To validate this rather counterintuitive trend of migration barriers as a function of surface depth, we also compute the migration barriers in a $2\times2\times6$ unit cell setup and find the largest migration energy of 0.48 eV in the bulk and the lowest energy of only 0.20 eV in L_2 of A-terminated surface slab. A detailed analysis of the results for the $2 \times 2 \times 6$ unit cell can be found in Appendix A.4. Figure 5.5 shows that this variation of the migration energy within the slab structure is correlated with the relative bond length variations of axial and equatorial bonds with respect to the bulk, such that significant axial compression of the surface leads to smaller migration energies. The observation that migration barrier is correlated with sizeable bond length variation is in agreement with previous results showing that larger lattice distortions lead to smaller migration energies for the through-cell migration of a Br vacancy in organic-inorganic perovskites [90]. However, a combination of factors is associated with the slightly higher migration barrier at the A-terminated surface as compared to that of the deeper lying layers. The subtle interplay between the interface with the vacuum layer and the extremely distorted structure with longer equatorial and unusually smaller axial bonds at A-terminated surface leads to additional space for lattice to restructure, which affect the absolute value of the migration energy.

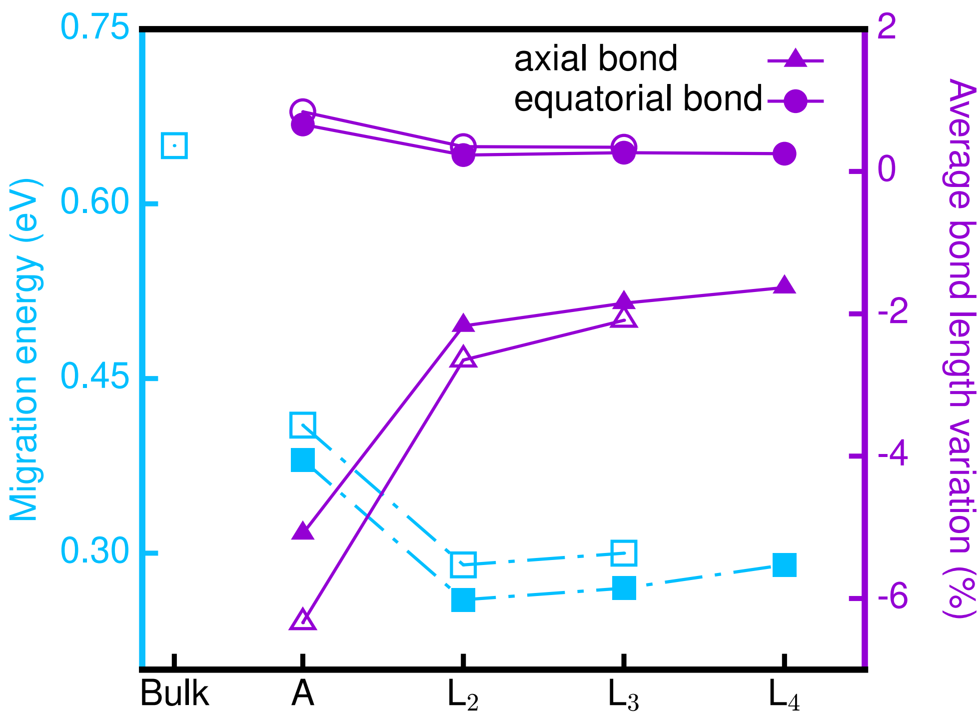

Figure 5.5: Migration energy and average bond length variation in the slab structure as a function of the layer in which Br vacancy migration takes place. The migration energy in the bulk is also shown in blue for comparison. Open and closed symbols correspond to the surface slab with three and four mobile top layers, respectively.

Figure 5.6 b) and c) show a zoomed-in side view of the migration paths of the moving Br ion, associated with the energy profiles showed in panel a). The structures of A- and B-terminated surfaces represent an average over the atomic configuration of the equivalent endpoints of the migration paths, overlaid with the representation of the path of the migrating Br ion. While in the bulk the moving Br ion migrates along an almost straight line, the migration path at both surfaces is described by a curve, with the saddle image pointing away from the surface. The shape of the migration path at the surface is consistent with previous experimental [323, 324] and theoretical [87, 325] reports finding similar curved migration paths for a vacancy drifting between an equatorial and an axial position in inorganic oxide perovskites. More recently, various theoretical studies [88, 186] reported similar curved paths for Pb-based halide perovskites.

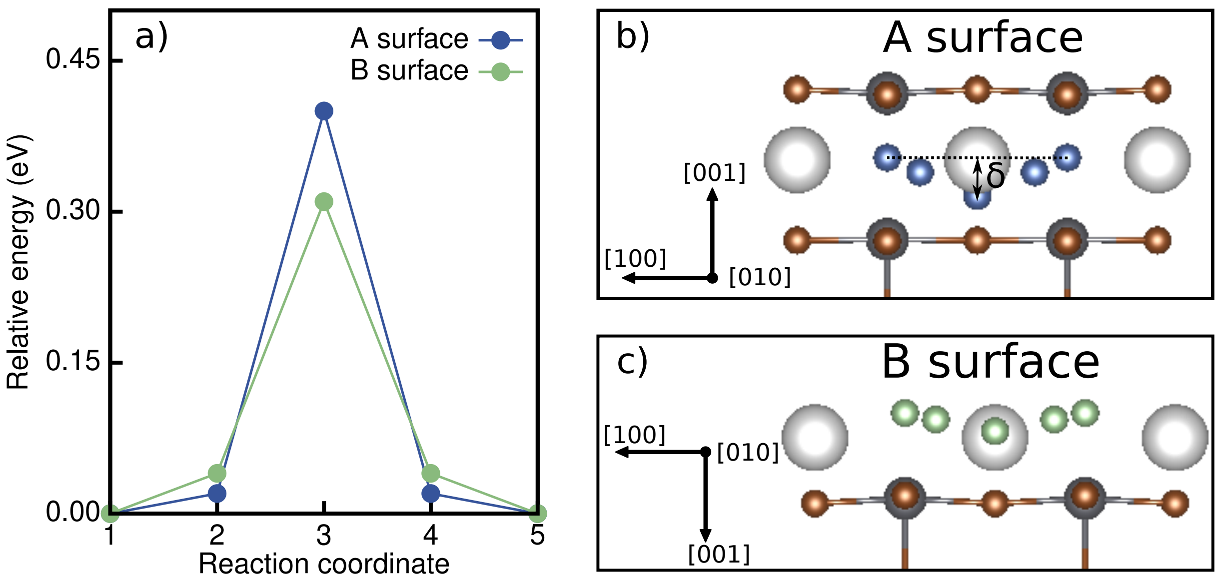

Figure 5.6: a) Energy profiles and migration paths for Br vacancy migration b) at the A-terminated surface (blue) and c) at the B-terminated surface (green). The structures correspond to the average atomic configurations of the two equivalent endpoints of each cNEB calculation overlaid with the position of the migrating Br ion along the migration path. The definition of the deviation δ from the linear path is shown in the structure corresponding to surface A.

To quantify the differences observed in the curvature of the migration path we compute the deviation δ from the linear path defined as the perpendicular distance between the position of the migrating Br ion in the saddle point configuration and the linear trajectory determined by the initial and final positions and schematically represented in Figure 5.6 b). As reported in table 5.2, we find that the migration Br ion follows an almost linear path in the bulk, with a deviation more than 7 times lower than those at the surface, showing the more flexible nature of the slab, which can deform and accommodate a defect more easily. Furthermore, we find that at B-terminated surface the deviation δ is almost half than that at A-terminated surface. This can be explained based on the less lattice restructuring necessary to accommodate the Br vacancy at B-terminated surface.

5.3.3. Surface passivation with alkali-halide monolayers

While in the previous sections we demonstrated that the migration barrier is highly influenced by the lattice distortions and surface restructuring, we now analyse the effect of surface modification on Br vacancy migration energies.

One of the most common strategies to suppress ionic migration at the surface and interfaces is passivation through surface modification [326]. Chemical surface treatment with organic ligands is an extensively used method to achieve increased photoluminescence lifetimes and quantum yields [327, 328], but it leads to additional stability issues. Recently, the passivation with simple inorganic alkali-halide salts has been suggested as an alternative approach [329–331]. Chen et al. showed that introducing a NaCl layer at the interface between the halide perovskite absorber and the electron- or hole-transport layers in solar cells leads to an enhanced stability due to a more more ordered perovskite crystal structure [330]. Furthermore, Apergi et al. showed using first principles calculations that the electronic level alignment between the halide perovskite absorber and hole-transport layer can be improved by using alkali-halide surface modifiers [331].

We investigate four alkali-halide monolayers (NaBr, NaCl, KBr and KCl) as possible candidates to reduce the halide-mediated migration at the surface of $CsPbBr_3$. We construct the passivated systems by placing the monolayers on top of the A-terminated surface and optimizing the structures. An example of such a system is depicted in Figure 5.7 a) that shows a slab structure passivated with a NaCl monolayer. Upon geometry optimization we find that the perovskite lattice is generally less compressed than the unpassivated slab system. Figure 5.7 b) shows that for passivation with Na-based monolayers, the variation of $Pb - Br$ axial bonds at A-terminated surface is less than 2 % and that of equatorial bonds is negligible. In contrast, passivation with K-based monolayers does not reduce the distortions as much. Moreover, using KBr monolayer leads bond lengths very similar to the ones in the unpassivated slab system. These larger distortions are induced by the lattice mismatch between the perovskite and the KBr passivation layer featuring bonds longer than those in the undistorted bulk structure. Na-based monolayers feature bond lengths only 0.08 Å different from the undistorted bulk and thus one would expect an increased migration barrier for the surfaces passivated with these Na-based monolayers.

Using the approach previously described, we analyse the migration process of a Br-mediated vacancy at the A-terminated surface of a slab passivated with Na-based monolayers, by introducing a Br vacancy in the surface layer and computing its migration barrier. Figure 5.8 a) shows that the migration at the A-terminated surface is highly suppressed when passivated with NaCl monolayer, featuring a migration energy of 0.57 eV, only 80 meV lower than that computed for the Br vacancy migration in the bulk. This increase in the migration barrier is an indirect effect of the surface restructuring induced by the NaCl monolayer with slightly smaller lattice parameter than the undistorted $CsPbBr_3$ bulk. However, as shown in Figure 5.8 b), the vacancy follows a curved migration path,

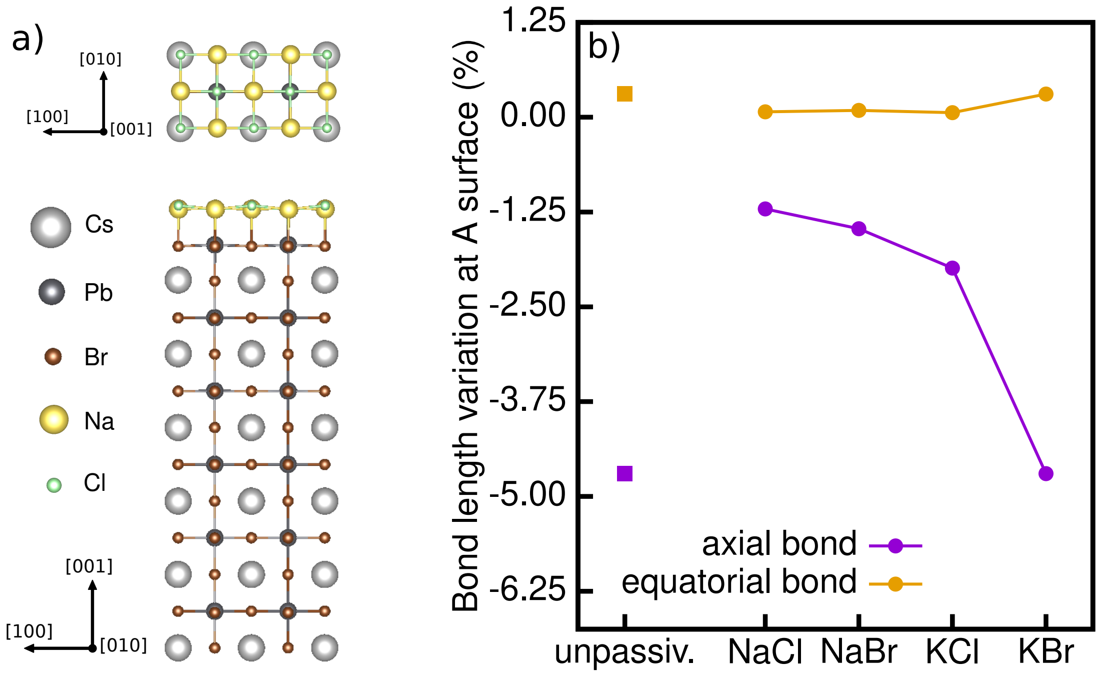

Figure 5.7: a) Slab supercell passivated with NaCl monolayer at A-terminated surface (top and side views). b) $Pb-Br$ bond length variation at surface A of the slab structure as a function of passivation layer. For comparison, the $Pb-Br$ bond lengths at surface A of the unpassivated slab structure are represented as squares.

with a larger deviation than in the unpassivated system (δ = 1.68 Å), highlighting the "softer" lattice of the slab surface system. Furthermore, we find that, influenced by the larger distortions, the migration barrier of 0.48 eV computed for the NaBr-passivated system is considerably lower than in the bulk and only 70 meV larger than at the unpassivated A surface. This difference in the migration barriers of the two Na-based-passivated systems confirms our previous finding that larger distortions of the perovskite lattice lead to smaller migration barriers.

In summary, in this chapter we presented a first principles DFT study of Br-mediated vacancy through-cell migration in cubic $CsPbBr_3$. Our first main finding is that the migration barrier within the close-packed bulk structure is roughly twice as large as that at either of the two CsBr-terminated or $PbBr_2$-terminated (001) surfaces of the system. Furthermore, we showed that the halide migration at the surface is facilitated by the larger structural flexibility of the surface, allowing for significant bond lengths variations as compared to the bulk. We also studied the effect of surface passivation with alkali-halide monolayers and demonstrated that a thoughtful choice of the passivation layer might decrease the ion migration at the surface, leading to a migration energy almost equal to its bulk value. Our study demonstrated that surfaces facilitates the ion migration process that is believed to be one of the main causes of the poor stability of perovskites. Our

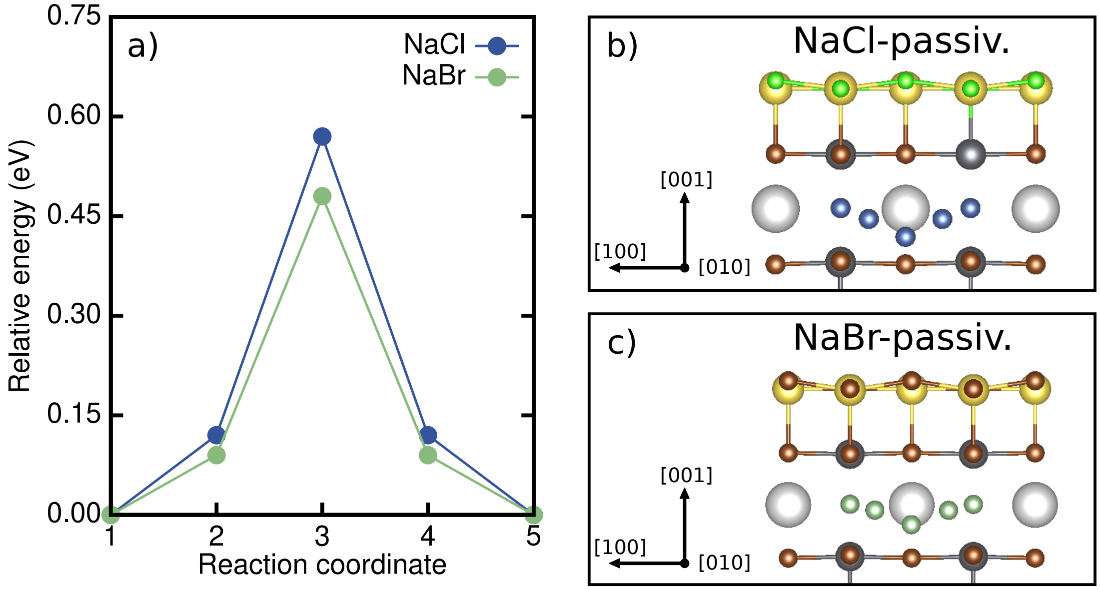

Figure 5.8: a) Energy profiles and migration paths for Br vacancy migration at the A-terminated surface passivated with b) NaCl monolayer (blue) and c) NaBr monolayer (green). The structures correspond to the average atomic configurations of the two equivalent endpoints of each cNEB calculation overlaid with the position of the migrating Br ion along the migration path.

observation that the migration barriers depend on the compression of the axial $Pb - Br$ bonds suggests that strain engineering could be another viable route for suppressing ion migration in halide perovskites [332].

Chapter 6

Conclusions and Outlook

6.1. Summary

A large part of the continuously growing research in the photovoltaics community is focused on studying promising absorber materials for light harvesting devices and their fundamental physical properties. In the past decade, metal-halide perovskites emerged as a new class of such materials with great potential, despite their soft structure prone to various kinds of inhomogeneities. With the present thesis we contributed to this topic by providing a detailed understanding of how different heterogeneities affect the structural and optoelectronic properties of metal-halide perovskites by means of state-of-the-art first principles calculations.

In our pursuit to elucidate the intricacies of physical properties of metal-halide perovskites, we concentrated our attention on three forms of inhomogeneities. We thus analysed the effect of macroscopic chemical heterogeneity in 3D double metal-halide perovskites, macroscopic structural heterogeneity in quasi-2D simple and double perovskites and microscopic local structural heterogeneity in the all-inorganic halide perovskite $CsPbBr_3$.

The macroscopic structural heterogeneity manifests in RP perovskites through the distinct separation of the inorganic perovskite backbone by long organic molecules. Our results showed that the DFT electronic band structure of Pb-based RP perovskites at the band edges is indirectly impacted by the organic cations via steric effects. Furthermore, we demonstrated that the energetic position of the electronic states emerging directly from the organic cation is inherited from the HOMO-LUMO gap of the freestanding molecule.

Motivated by the tremendous diversity of perovskite materials, we turned our attention to Pb-free compounds and performed a quick DFT screening of a series of 3D and quasi-2D double perovskites, which revealed two main families of Pb-free materials exhibiting promising semiconducting properties. Therefore, in the next part of this thesis we studied the electronic properties of Ag-Bi, Ag-Sb, Ag-In and Ag-Tl double metal-halide perovskites. Using DFT and *ab initio* many-body perturbation theory within G_0W_0 approximation, we demonstrated that the chemical heterogeneity of the 3D double perovskites leads to high anisotropy of the effective masses and electronic states at the band edges localized within individual octahedra. Furthermore, the lower-dimensional derivatives of Ag-In and Ag-Tl double perovskites exhibit fundamentally different electronic properties than their 3D counterparts, highlighted by a striking change in color as the thickness of the inorganic layer decreases. We also proved that the change in the band gap character of these RP perovskites is a direct consequence of the dimensional reduction.

The optical properties of the Pb-free double halide perovskites were also a subject of interest in our broad study. Thus, in the next section of this thesis we performed G_0W_0+BSE calculations for $Cs_2AgB^{III}X_6$ with B^{III}=Bi, Sb, In and X_6=Br, Cl and computed their absorption spectra, exciton binding energies and average electron-hole separations. We find that the Ag-pnictogen compounds exhibit strongly localized resonant excitons. The binding energies of these excitons scale linearly with the lowest direct band gap and their localization correlates with the composition of CBM. The exceptionally high exciton binding energies of up to $\sim$450 meV computed for these materials are similar to what have been typically observed for quantum confined systems. We showed that Elliott's theory, the most common technique used to extract exciton binding energies from experimental optical absorption spectra, fails for all these systems because it relies on equivocal assumptions that are not generally valid regardless of the nature of analysed material. By computing and representing the excitonic wave functions in Ag-Bi and Ag-Sb double perovskites, we demonstrated that the chemical "confinement" observed in these compounds is caused by the localization of electrons and holes in chemically distinct octahedra. For $Cs_2AgInCl_6$ we found that the parity-forbidden lowest direct transition leads to a range of optically inactive excitonic states. However, by analysing the subsequent bright states, we noted that the fundamental band gap of $Cs_2AgInCl_6$ could still be defined as the optical gap.

In the final part of this thesis we turned to all-inorganic simple perovskite $CsPbBr_3$ in an effort to understand one of the most common issues leading to material degradation, namely the migration process of microscopic structural inhomogeneities represented by Br-vacancies. We performed DFT calculations and used cNEB method to show that the vacancy migration process is facilitated at the surface, for which we computed a migration barrier that is roughly half of the value in the closed-pack bulk. Our results indicate that the "softer" structure of the surface, affording for larger distortions, is responsible for the significantly lower migration energy and curved path described by the Br-vacancy. We also studied the effect of surface passivation with alkali-halide monolayers and validated our hypothesis by showing that the migration process can be diminished through passivation with a judicious choice of a simple alkali halide salt.

6.2. Outlook

Despite the fact that we conducted a rather detailed study employing a high-level of theory throughout our calculations, there are still several open questions.

For example, based on recent reports claiming that exciton binding energy is highly affected by the coupling of free electrons and holes to phonons [283, 333], one possible improvement would be the inclusion of polaronic and phonon screening effects within the BSE formalism. However, the GW+BSE calculations are already known to be extremely computational demanding and efforts to include dynamical screening from phonons are still ongoing. Apart from the overall improvement of the agreement between the computed and experimental binding energies, the inclusion of the electron-phonon coupling is particularly relevant at one specific point in our work. The presence of multiple dark excitonic states up to 414 meV below the first bright state, arising from the band folding, in the $I4/m$ phase of $Cs_2AgBiBr_6$ suggests that the experimentally observed photoluminescence ~1 eV below the absorption onset could be related to phonon-assisted optical transitions [334].

An intriguing feature observed in our study of optical properties in double metal-halide perovskites is that even though $Cs_2AgInCl_6$ features similar chemical heterogeneity as the Ag-pnictogen compounds, induced by the alternating metal sites, its excitonic properties are essentially different. This suggests that optoelectronic properties of double metal-halide perovskites are highly dependent on the band edge orbital character and calls for further study to elaborate a robust model for elucidating the excitonic properties of the already synthesised compounds and consistently predicting them for the perovskites that currently are only at the stage of theoretical models.

Another compelling finding that have also been demonstrated in literature [264, 270] is the change in the nature of the band gap when Ag-Bi and Ag-Tl perovskites are thinned to monolayers. The direct band gap of Ag-Bi $n = 1$ RP perovskite combined with its increased stability under ambient conditions render this material especially desirable for photovoltaic applications. However, apart from some experimental optical spectra recently reported [264], there is no in-depth study of the excitonic features of the layered double metal-halide perovskites and the origin of the peak seen at the onset of the optical absorption spectrum is still under debate. Furthermore, the change in the nature of the band gap of Ag-Tl perovskites is not apparent in the optical absorption spectra [270]. We note that by employing a GW+BSE approach one can assess the excitonic features, if present, and evaluate the suitability of 2D RP perovskites for light-harvesting applications through an in-depth analysis of the fine structure of the absorption spectra. Therefore, one of our main focuses is to extend the study presented in Chapter 4 to experimentally-determined and model systems of RP derivatives of the already studied double metal-halide perovskites.

Although further investigations are required for a full understanding of the optoelectronic properties in these notoriously complex materials, we believe that this thesis uncovers a new intuition for the physics of heterogeneous metal-halide perovskites and opens up new paths in the research of these tremendously diverse and captivating compounds.

Appendix

Computational details

A.1. Convergence parameters in practical calculations

In this section we aim to describe the main convergence parameters involved in the performed calculations. We note that the setups of the calculations for 2D perovskites are based on parameters previously reported in literature and therefore no further testing was done. For all other calculations, the convergence of the parameters described in the following sections have been extensively tested and is presented in detail in the rest of this chapter.

For electronic structure calculations of periodic systems, such as perovskite materials analysed in this thesis, the most common approach is to use a plane-wave basis. Furthermore, as demonstrated in Ref. [3, 335], their crystal perodicity allows us to rewrite the KS eigenfunctions involved in DFT and G_0W_0 methodologies described in chapter 2 using Bloch's theorem. Within this framework, KS orbitals can be written as a product of a wave-like part with the same periodicity as the underlying lattice and a cell-periodic part that can be further expanded in terms of a discrete plane-wave basis set:

$$\phi_{n\mathbf{k}}(\mathbf{r}) = \frac{1}{\sqrt{\Omega}} \sum_{\mathbf{G}} c_{n\mathbf{k}+\mathbf{G}} e^{i(\mathbf{k}+\mathbf{G})\cdot\mathbf{r}}, \tag{A.1}$$

where Ω is the unit cell volume and $\mathbf{G}$ is a vector in the reciprocal lattice. In the equation A.1 the basis functions are known and the coefficients $c_{n\mathbf{k}+\mathbf{G}}$ are to be determined, turning the solving of a set of KS equations into a problem of linear algebra, which can be solved using standard diagonalization techniques.

A.1.1. DFT calculations

The electronic charge density $n(\mathbf{r})$ can also be written based on Bloch's theorem as

$$n(\mathbf{r}) = \sum_n \int_{BZ} \frac{d\mathbf{k}}{\Omega} \sum_{\mathbf{G}} c_{n\mathbf{k}+\mathbf{G}} e^{i(\mathbf{k}+\mathbf{G})\cdot\mathbf{r}}, \tag{A.2}$$

where $\sum_n$ is a sum over occupied states and the integration is performed in the first Brillouin zone. In practice, the Brillouin zone is sampled using a discrete mesh and the integral is numerically computed on this grid of $\mathbf{k}$-points. The density of the $\mathbf{k}$-point mesh increases with the increase of the system and in the limit of an ideal unbound crystal, the $\mathbf{k}$-point grid is infinite. However, calculations with extremely dense grids are prohibitive and usually an optimal finite set of $\mathbf{k}$-points is employed to sample the Brillouin zone. For accurate practical calculations, the relevant physical quantities should be converged with respect to the size of the $\mathbf{k}$-point grid.

The sum $\sum_{\mathbf{G}}$ is performed for all vectors in the plane-wave basis. In principle, the basis functions should form a complete functional space requiring an infinite number of plane-waves. However, for computational reasons, the basis set necessarily consists of a finite number of basis functions. In practice this number is determined by the cutoff energy $E_{cut}^{MF} = \frac{1}{2}\left|\mathbf{G}_{cut}^{MF}\right|^2$. Therefore, the convergence of the relevant quantities should be tested against the maximum allowed kinetic energy of the plane-waves E_{cut}^{MF} which is a crucial parameter in DFT calculations. Since larger E_{cut}^{MF} leads to denser basis set approaching a complete one and smaller E_{cut}^{MF} reduces the number of coefficients to be computed, the cutoff energy is usually determined as a compromise between numerical accuracy and computational load.

The main challenge of the plane-wave basis set based calculations is the accurate description of localized features such as core orbitals. To overcome this issue the strong Coulomb potential is replaced by a weaker pseudopotential [336] using the frozen core approximation first introduced by Fermi [337] where the valence electrons are separated from the tightly bound core electrons. Therefore, the valence region features smooth pseudo wave function identical to the all-electron one while the pseudo wave function of the core region is nodeless and has the same norm as the all-electron wave function. As consequence, the chemical bonding in crystalline systems is accurately described using the combination of plane-wave methodology and pseudopotential concept [338]. Two of the most common formalisms for designing pseudopotentials are projector augmented waves (PAW) [339–341] and norm-conservation [342–344]. The results presented in this thesis were obtained using one of these two approaches depending on the software package in which the calculations were performed.

A.1.2. G_0W_0 calculations

One of the most computationally demanding step is calculation of (static or frequency-dependent) polarizability and dielectric function. In the BerkeleyGW software package these quantities are computed within the RPA using as input the electronic eigenvalues and eigenfunctions from a mean-field reference system [345]. The static RPA polarizability is expressed in a plane-wave basis based on the equation [42]:

$$\chi_{\mathbf{G}\mathbf{G}'}(\mathbf{q};0) = \sum_{n}^{occ} \sum_{n'}^{unocc} \sum_{\mathbf{k}} M^*_{nn'}(\mathbf{k},\mathbf{q},\mathbf{G}) M_{nn'}(\mathbf{k},\mathbf{q},\mathbf{G}') \frac{1}{E_{n\mathbf{k}+\mathbf{q}} - E_{n'\mathbf{k}}}, \tag{A.3}$$

where $M^*_{nn'}(\mathbf{k},\mathbf{q},\mathbf{G}) = \langle \phi_{n\mathbf{k}+\mathbf{q}} | e^{i(\mathbf{q}+\mathbf{G})\cdot\mathbf{r}} | \phi_{n'\mathbf{k}} \rangle$ are the plane-wave matrix elements. In practice, the number of plane-waves is determined by $|\mathbf{q}+\mathbf{G}|^2 < E^{\varepsilon}_{cut}$, where E^{ε}_{cut} is the polarizability cutoff energy and the number of unoccupied states n' is determined such that the highest unoccupied state has an energy corresponding to E^{ε}_{cut} [345]. Therefore, in equation A.3 there is only one independent convergence parameter. One should converge either polarizability cutoff or number of unoccupied states, keeping the other parameter fixed at the correspondent value.

The RPA dielectric matrix can be obtained from the polarizability defined in equation A.3, as described in Ref. [345]:

$$\varepsilon_{\mathbf{G}\mathbf{G}'}(\mathbf{q};0) = \delta_{\mathbf{G}\mathbf{G}'} - v(\mathbf{q}+\mathbf{G})\chi_{\mathbf{G}\mathbf{G}'}(\mathbf{q};0), \tag{A.4}$$

where the bare Coulomb interaction $v(\mathbf{q}+\mathbf{G})$ has the following form for the crystalline systems:

$$v(\mathbf{q}+\mathbf{G}) = \frac{4\pi}{|\mathbf{q}+\mathbf{G}|^2}. \tag{A.5}$$

Furthermore, using the equations A.4 and A.5, the screened Coulomb interaction is defined as

$$W_{\mathbf{G}\mathbf{G}'}(\mathbf{q};0) = \varepsilon^{-1}_{\mathbf{G}\mathbf{G}'}(\mathbf{q};0) v(\mathbf{q}+\mathbf{G}'). \tag{A.6}$$

All the calculations presented in this thesis were performed using the Godby-Needs generalised plasmon pole model [32, 44, 346] (GPP) to extend the dielectric response to non-zero frequencies. Within GPP model, the dynamic screening is expressed as discussed in Ref. [42] by the following equation:

$$\varepsilon_{\mathbf{G}\mathbf{G}'}(\mathbf{q};\omega) = \delta_{\mathbf{G}\mathbf{G}'} + \frac{\Omega^2_{\mathbf{G}\mathbf{G}'}(\mathbf{q})}{\omega^2 - \tilde{\omega}^2_{\mathbf{G}\mathbf{G}'}(\mathbf{q})}, \tag{A.7}$$

where $\Omega^2_{\mathbf{G}\mathbf{G}'}(\mathbf{q})$ and $\tilde{\omega}^2_{\mathbf{G}\mathbf{G}'}(\mathbf{q})$ are the effective bare plasma frequencies and are determined by evaluating the RPA dielectric matrix at $\omega = 0$ and $\omega = i\omega_p$, ω_p being the plasma frequency [32, 44, 346].

The self-energy operator Σ in QP equation 2.36 can be written as the sum between the screened exchange operator Σ_{SX} and the Coulomb-hole operator Σ_{CH} [26, 40, 42]. Furthermore, both exchange and correlation self-energy matrix elements can in turn be expressed in a plane-wave basis set [42]. Using the form for the dielectric function given by the GPP model in equation A.7, the self-energy matrix elements can be written as described in Ref. [42, 345]:

$$\begin{aligned}\langle\phi_{n\mathbf{k}}|\,\Sigma_{SX}(E)\,|\phi_{n'\mathbf{k}}\rangle = &-\sum_{m}^{occ}\sum_{\mathbf{q}}\sum_{\mathbf{GG'}} M^{*}_{mn}(\mathbf{k},-\mathbf{q},-\mathbf{G})M_{mn'}(\mathbf{k},-\mathbf{q},-\mathbf{G})\\ &\times\left[\delta_{\mathbf{GG'}}+\frac{\Omega^{2}_{\mathbf{GG'}}(\mathbf{q})}{(E-E_{m\mathbf{k}-\mathbf{q}})^{2}-\tilde{\omega}^{2}_{\mathbf{GG'}}(\mathbf{q})}\right]v(\mathbf{q}+\mathbf{G'})\end{aligned} \tag{A.8a}$$

$$\begin{aligned}\langle\phi_{n\mathbf{k}}|\,\Sigma_{CH}(E)\,|\phi_{n'\mathbf{k}}\rangle = &\frac{1}{2}\sum_{m}\sum_{\mathbf{q}}\sum_{\mathbf{GG'}} M^{*}_{mn}(\mathbf{k},-\mathbf{q},-\mathbf{G})M_{mn'}(\mathbf{k},-\mathbf{q},-\mathbf{G})\\ &\times\frac{\Omega^{2}_{\mathbf{GG'}}(\mathbf{q})}{\tilde{\omega}_{\mathbf{GG'}}(\mathbf{q}(E-E_{m\mathbf{k}-\mathbf{q}}-\tilde{\omega}_{\mathbf{GG'}}(\mathbf{q})}v(\mathbf{q}+\mathbf{G'})\end{aligned} \tag{A.8b}$$

In the expressions of the self-energy matrix elements the last sums run over all $\mathbf{q}$ points of the grid used to sample the Brillouin zone and all $\mathbf{G}$ vectors defined by a set cutoff energy. In equation A.8a the first sum includes all occupied m states, while in equation A.8b both occupied and unoccupied states. This leads to the presence of two interdependent convergence parameters: total number of states and screened Coulomb cutoff energy. In practice, the convergence of the QP band gap is tested first with respect to the screened Coulomb cutoff while keeping the number of total bands extremely high such that $m \to \infty$ and next against total number of bands m while assuming a constant, very high value for the dielectric matrix cutoff energy

A.1.3. BSE calculations

The BSE defined in equation 2.43 of section 2.4 is solved in two main steps: first, the electron-hole interaction kernel K_{eh} is constructed on a coarse $\mathbf{k}$-point grid and then the kernel is interpolated to a much more denser (fine) $\mathbf{k}$-point grid and diagonalized.

All calculations presented in chapter 4 were performed using K_{eh} within the static limit as defined in Ref. [345], where it can be expressed as the sum $K_{eh} = K^{d} + K^{x}$ between a screened direct interaction K^{d} and a bare exchange interaction K^{x}. The two components are expressed in plane-wave basis set as firstly described by Rohlfing et al. [29]:

$$\langle\phi_{vc\mathbf{k}}|\,K^{d}\,|\phi_{v'c'\mathbf{k'}}\rangle = \sum_{\mathbf{GG'}} M^{*}_{cc'}(\mathbf{k},\mathbf{q},\mathbf{G})W_{\mathbf{GG'}}(\mathbf{q};0)M_{vv'}(\mathbf{k},\mathbf{q},\mathbf{G'}), \tag{A.9a}$$

$$\langle \phi_{vc\mathbf{k}} | K^x | \phi_{v'c'\mathbf{k}'} \rangle = \sum_{\mathbf{G}!=0} M^*_{vc}(\mathbf{k},\mathbf{q},\mathbf{G}) v(\mathbf{q}+\mathbf{G}) M_{v'c'}(\mathbf{k},\mathbf{q},\mathbf{G}). \tag{A.9b}$$

Usually, the coarse **k**-grid used to construct these matrices is the same as the one used to calculate the dielectric matrix $\varepsilon^{-1}_{\mathbf{q}}$ as discussed in the previous section. In principle in the number of valence v and conduction c bands are convergence parameters that should be tested to acquire accurate optical absorption spectra. However, in practice the range determined by the energy corresponding to v and c, respectively is approximately 10 eV, ensuring an optical spectrum converged beyond the visible region [345].

Very dense **k**-point grids are required to capture the dependece of the exciton binding energies and absorption spectra with the joint density of states (JDoS) in periodic systems. Since the direct calculation of kernel matrix elements on such a fine grid is computationally inaccessible the electron-hole kernel computed on a coarse **k**-grid and interpolated on the fine one. The final step is the diagonalization that leads to the set of exciton eigenvalues Ω^S and eigenfunctions $A^S_{cv\mathbf{k}}$ which in turn can be used to obtain the absorption spectrum. The convergence of the relevant quantities should be tested against the density of points in the fine k-grid used for the interpolation of the kernel.

A.2. Electronic properties

A.2.1. Computational screening of Pb-free double perovskites

The study presented in section 3.3 was conducted using Vienna Ab-initio Software Package (VASP) [347, 348] software package and projector augmented wave (PAW) pseudopotentials [349], provided by VASP libraries. For all geometry optimisation calculations we sampled the Brillouin zone using **k**-grids with $12 \times 12 \times 12$ points for the bulk materials and $4\times4\times2$ for the 2D RP compounds, respectively and the PBEsol (a version of PBE approximation specifically revised for solids) functional [350] to approximate the xc energy. The electronic band structure calculations were performed using PBE functional [67], on a $8 \times 8 \times 8$ **k**-point mesh for bulk systems and $4 \times 4 \times 2$ for the quasi-2D RP derivatives. Furthermore, the effect of spin-orbit coupling (SOC) was included self-consistently throughout all the calculations.

Our computational screening had $Cs_2AgBiBr_6$ double perovskite as starting point. All the other studied structures are theoretical systems achieved by replacing the corresponding ions in the crystal lattice of the bulk or 2D RP derivative of $Cs_2AgBiBr_6$ and optimising the respective structure without imposing any constraints, i.e. atomic positions, unit cell shape and volume were allowed to modify during the structural relaxations. Therefore, we tested the convergence of the plane-wave cutoff energy only for $Cs_2AgBiBr_6$ and used the same value for all the other compounds. In Figure A.1 we show that the chosen value of 450 meV for the cutoff energy ensures a convergence of the total energy to within ∼10 meV. Thus, we performed all calculation using the same value for the plane-wave cutoff energy.

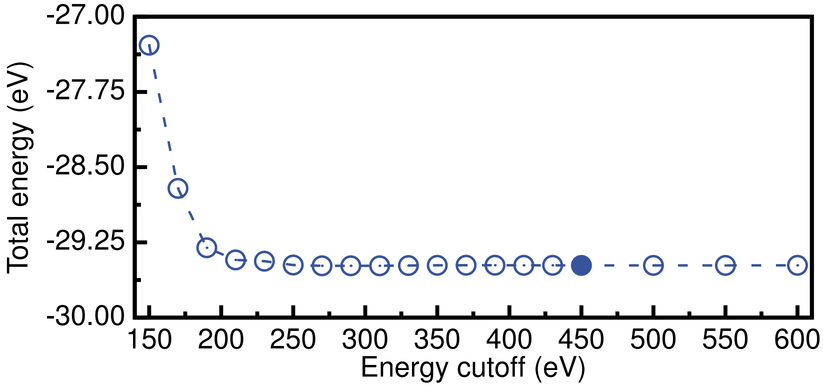

Figure A.1: $Cs_2AgBiBr_6$ total energy (in eV) with respect to plane-waves kinetic energy cutoff for. Closed symbol represents the value selected to be used further.

A.2.2. $Cs_2AgB^{III}X_6$ halide double perovskites

All mean-field DFT calculations in section 3.4 have been performed using the Quantum espresso software package [351, 352]. The electronic structure of $Cs_2AgB^{III}X_6$ halide double perovskites, with B=Bi, Sb and X=Br, Cl has been computed using LDA [61, 62] for the xc functional, while for that of $Cs_2AgInCl_6$ we used PBE [67]. We used a set of norm-conserving, fully relativistic Troullier-Martins[344] pseudopotentials similar with the ones from Ref. [226], where it has been demonstrated that the semicore states are particular important for the calculation of the QP energies. Therefore, the following electronic configurations have been employed throughout in our calculations: $5s^25p^66s^1$ for Cs, $4s^24p^64d^{10}5s^1$ for Ag, $5d^{10}6s^26p^3$ for Bi, $4d^{10}5s^25p^3$ for Sb, $4d^{10}5s^25p^1$ for In, $4s^24p^5$ for Br and $3s^23p^5$ for Cl.

Figure A.2 shows that the self-consistent ground-state calculations have been performed such that the total energy is converged to within 5 meV. For Ag-pnictogen double perovskites we used a plane-waves kinetic energy cutoff of 150 Ry (∼2040 eV), while for $Cs_2AgInCl_6$ a plane-waves kinetic energy cutoff of 60 Ry (∼816 eV) was employed. The calculations for all materials have been performed by sampling the Brillouin zone on a $10 \times 10 \times 10$ Γ-centered uniform **k**-point mesh, comprising 220 irreducible points.

The zeroth-order one-particle Green's function G_0 and screened Coulomb interaction W_0 in order to obtain the QP band structure have been constructed using the DFT eigensystem computed with the above settings. As showed in Ref. [16, 226, 264], the spin-orbit coupling leads the formation of an isolated conduction band in the Bi-based compounds, due to a splitting of Bi $p_{1/2}$ and Bi $p_{3/2}$ states, of at least 1.5 eV. To account for

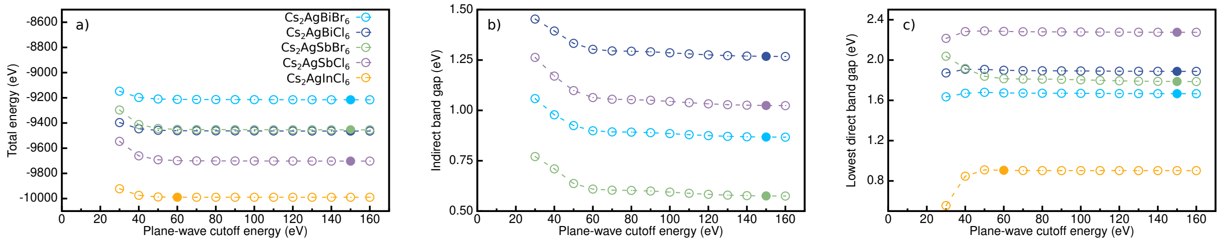

Figure A.2: a) Total energy, b) indirect band gap of Ag-pnictogen materials and c) lowest direct band gap (in eV) with respect to plane-waves kinetic energy cutoff for $Cs_2AgB^{III}X_6$ halide double perovskites. Closed symbols represent the values selected to be used further.

this effect, fully-relativistic spin-orbit coupling (SOC) has been employed self-consistently in the construction of G_0 and W_0 for Ag-pnictogen materials. In contrast, for $Cs_2AgInCl_6$, as demonstrated in Ref. [257], SOC does not influence the electronic band structure. Therefore, our calculations for Ag-In double perovskite do not include SOC.

All GW calculations have been performed using the BerkeleyGW software package [345], with the generalized plasmon-pole method of Godby and Needs [346]. To establish the computational setup we checked the convergence of all parameters described in section A.1.2. Figure A.3 a) shows the convergence of the static dielectric constant ε_∞ with respect to the polarizability cutoff. Figure A.3 b) and c) show the convergence of the lowest direct band gap with respect to interdependent parameters screened Coulomb cutoff and number of bands. To determine the optimal values we first analysed the variation of the lowest energy direct gap with the screened Coulomb cutoff, while keeping the total number of bands fixed to 1000 for Ag-pnictogen perovskites and 800 for $Cs_2AgInCl_6$. Second, we fixed the cutoff energy to 10 Ry for Ag-pnictogen materials and 8 Ry for $Cs_2AgInCl_6$ and checked the convergence of the lowest energy direct gap with respect to total number of bands.

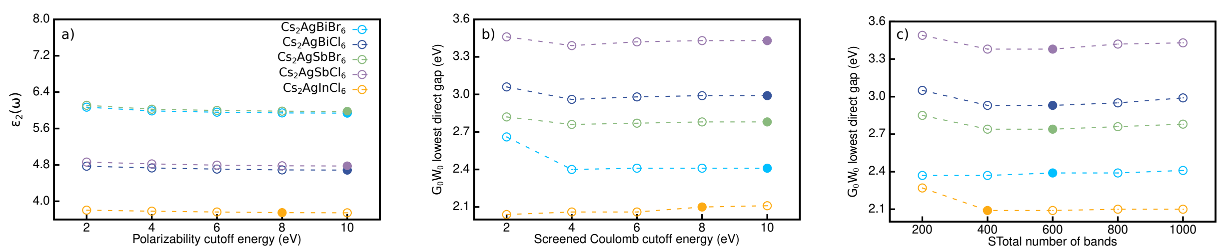

Figure A.3: a) Static dielectric constant (ε_∞) with respect to polarizability cutoff energy and G_0W_0 lowest energy direct band gap (in eV) as a function of b) screened Coulomb cutoff energy (using 1000 bands) and c) total number of bands (using a screened Coulomb cutoff of 10 Ry) for $Cs_2AgB^{III}X_6$ halide double perovskites. Closed symbols represent the values selected used in our setup.

We used a 600 bands for Ag-pnictogen materials and 400 bands for $Cs_2AgInCl_6$, a polarizability cutoff of 10 Ry (136 eV) and 8 Ry (109 eV) for Ag-pnictogen and Ag-In double perovskites, respectively, and an energy cutoff of 60 Ry (816 eV) for the bare Coulomb interaction. As showed in Figure A.3, using these parameters we achieve QP band gaps converged to within 50 meV and static dielectric constant converged to within 10^{-3}. DFT and G_0W_0 electronic band structures showed in Figure A.4 are obtained by Wannier interpolation using the WANNIER90 code [353]. We note that the use of G_0W_0 approximation opens up the band gap of all studied materials by at least 0.8 eV. We used a set of 42 and 24 maximally localized Wannier functions for the valence and conduction, respectively, to accurately interpolate the DFT band structures of $Cs_2AgB^{III}X_6$ double perovskites in the vicinity of the band gap, corresponding to Ag s, Ag d, B^{III} s, B^{III} p and X p states, with B^{III}=Bi, Sb and X=Br, Cl. For $Cs_2AgInCl_6$ we used 14 and 16 Wannier functions for the valence and conduction region, respectively, corresponding to Ag s, Ag d, In s, In d and Cl p states.

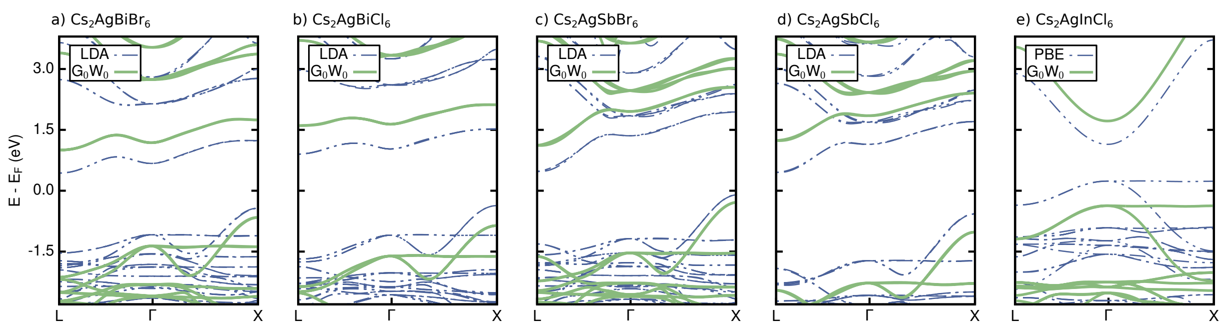

Figure A.4: DFT (blue dashed line) and G_0W_0 (green solid line) Wannierized band structures of a) $Cs_2AgBiBr_6$; b) $Cs_2AgBiCl_6$; c) $Cs_2AgSbBr_6$ and d) $Cs_2AgSbCl_6$, e) $Cs_2AgInCl_6$.

The effective masses reported in section 3.4.2 were calculated using the Wannier interpolation scheme and a grid spacing of 0.02 Å^{-1}. The effective masses are determined by calculating the second derivatives of the valence and conduction band edges, evaluating them numerically on a dense reciprocal space grid. In Table A.1 we show an extensive analysis of the parameters introducing uncertainties in the effective mass calculation for the particular case of $Cs_2AgBiBr_6$ double perovskite but we note that all studied materials display a similar behaviour. The interpolation scheme used to compute the energies of the bands leads to a systematic error of ~8 %, while the grid spacing introduced a further error of up to ~14 % in the calculated hole effective mass. The DFT starting point is another source of uncertainty in the effective mass calculations.

Note that, as previously stated, for Ag-pnictogen materials we employed DFT-LDA starting point, whereas for $Cs_2AgInCl_6$ we used DFT-PBE as starting point.

Table A.1: Effective masses and reduced mass at X (in units of the electron rest mass m_0), BSE and Wannier-Mott exciton binding energies (in meV) of cubic $Cs_2AgBiBr_6$ for LDA and PBE starting points.

Methodology		**Grid**	**Effective masses (m_0)**		
theory	**interpolation**	**spacing (1/Å)**	$\mathbf{m}_h^*$	$\mathbf{m}_e^*$	μ
G_0W_0@LDA	linear	0.093	0.33	1.23	0.26
	Wannier	0.093	0.35	1.12	0.27
		0.020	0.31	0.86	0.23

A.2.3. Pb-based 2D Ruddlesden-Popper perovskites

The results presented in section 3.2, were computed via DFT calculations performed within the generalized gradient approximation of Perdew-Burke-Ernzerhof (PBE) [67] as implemented in VASP [347, 348], using PAW potentials [349] that are part of the VASP library. The PAW pseudopotentials have the following atomic configurations: $2s^2p^3$ for N, $1s^1$ for H, $2s^22p^2$ for C, $6s^26p^2$ for Pb and $5s^25p^5$ for I. All the calculations include the effect of fully-relativistic spin-orbit coupling (SOC) self-consistently. We used Γ-centered **k**-point grids with $2 \times 2 \times 1$ points for the ground-state calculations and $6 \times 6 \times 2$ points for the density of states (DOS) calculations, respectively, and a cutoff energy for the plane-wave expansion of 500 eV. All model systems with layer thickness of $n = 1$ were designed by replacing the organic cation with Cs. The undistorted model system has been constructed using untilted and undistorted metal-halide octahedra as found in the 3D cubic phase (with $Pm\bar{3}m$ symmetry) of $MAPbI_3$, with Pb-I bond lengths of 3.15 Å. The distorted model systems MA-, BA- and PEA-like feature the tilts and distortions found in the experimental structures of tetragonal $I4/mcm$ $MAPbI_3$, BA_2PbI_4 and PEA_2PbI_4, respectively. In order to avoid spurious interactions between periodic images in these monolayer model systems, a vacuum layer of at least 20 Å was introduced and a dipole correction was applied in all calculations.

A.2.4. Dimensional reduction of Pb-free double perovskites

In section 3.5, we carried out first principles DFT calculations on single-crystal X-ray diffraction structures (SCXRD) to understand the effects of reduced dimensionality on the electronic structure of the Ag-Tl, Ag-In and Ag-Bi families of layered double perovskites.

All calculations were performed using VASP [347, 348] and PAW pseudopotentials [349], with the following atomic configurations: $5s^25p^66s^1$ for Cs, $6s^26p^1$ for Tl, $4d^105s^1$ for Ag, $6s^26p^3$ for Bi, $5s^25p^1$ for In, $4s^24p^5$ for Br, $2s^22p^2$ for C and $2s^22p^3$ for N. To sample the Brillouin zone, we used **k**-point grids containing $4 \times 4 \times 4$ points for the 3D double perovskites $Cs_2AgTlBr_6$, $Cs_2AgInCl_6$ and $Cs_2AgBiBr_6$ and $2 \times 2 \times 1$ points for the 2D derivatives **2-Tl**, **1-Tl**, **1'-Tl**, **1-In**, **2-Bi** and **1-Bi**. Furthermore, we used a cutoff energy of 500 eV for the plane-wave expansion and obtained band gaps converged within 50 meV.

The electronic band structure of Ag-Bi layered double perovskites was computed using PBE exchange-correlation functional [67] and including SOC self-consistently. In line with the results from Ref. [264], we found that the inclusion of SOC highly impacts the electronic bands of Ag-Bi layered double perovskite family, introducing a large spin-orbit splitting between the $J = 1/2$ and $J = 3/2$ bands in the conduction region. However, the valence band remains almost unaffected by SOC due to its predominantly Ag d, Bi s and Br p character and the lack of contribution from Bi p states.

Despite the well known limitations of the semilocal approximations to the exchange-correlation functional leading to underestimation of the bandgaps in semiconductors, the overall features of the electronic band structures, as well as trends for band gap and band dispersion are generally predicted very well. Thus, our choice of using PBE is justified. However, as reported in Ref. [271], for $Cs_2AgTlBr_6$ the use of PBE leads to an nonphysical metallic character of the system, by pushing the CBM below the VBM. To correct this severe underestimation of the band gap we used the screened hybrid functional of Heyd, Scuseria and Ernzerhofer (HSE06) [77] for all members of the Ag-Tl and Ag-In double perovskite families. Although the absolute values of band gaps are still seriously underestimated, HSE06 exchange-correlation functional yields qualitatively accurate results, predicting the Ag-Tl materials to be semiconductors. Furthermore, the trend of the HSE06 computed band gaps ($E_{gap}^{Cs_2AgTlBr_6} < E_{gap}^{\textbf{2-Tl}} < E_{gap}^{\textbf{1-Tl}} < E_{gap}^{\textbf{1'-Tl}} < E_{gap}^{\textbf{1-In}}$) is in line with the experimentally determined trend in the absorption onsets reported in Ref. [270]. Note that, to obtain band gaps with absolute values comparable with the experimental ones, one need to explicitly account for electron-hole interactions. Furthermore, we tested the effect of SOC and obtained almost no change in the bands dispersion, leading to band gap differences lower than 0.1 eV. This is a consequence of the predominantly s orbital character of the CBM in these materials. Therefore, the effect of SOC have been neglected in all calculations for Ag-Tl and Ag-In materials.

Next, to disentangle the effect of dimensional reduction from the ones of structural distortion induced in the perovskite lattice, we computed the electronic structure of a series of undistorted model systems. The undistorted model systems with perovskite layer thickness $n = 1$ and $n = 2$ (**1M** and **2M**) discussed in section 3.5 were constructed with $Ag - Br$ and $Tl - Br$ bond lengths of 2.81 Å and2.73 Å, respectively, corresponding to the average bond lengths in the 3D parent $Cs_2AgTlBr_6$ material. The undistorted model systems were constructed such that the organic molecules have been replaced by Cs cations. To avoid the spurious interactions between the periodic images of the unit cells, a vacuum layer of 20 Å was introduced between the perovskite layers and a dipole correction was applied.

Figure A.5 shows that the general features of the electronic band structures of **1M** and **2M** are very similar to those of **1-Tl** and **2-Tl**. The model systems retain the nature of the band gap observed in the experimentally-determined perovskite structure, suggesting that the direct-to-indirect gap transition in $n = 1$ derivatives is induced by the reduced dimensionality of the inorganic layer. However, the structural distortions present in the experimental structures **1-Tl** and **2-Tl** lead to significant differences in the band dispersion of these systems. The CBM of **1M** shifts to Γ, leaving the lowest energy transition to take place between the VBM at A and the CBM at Γ. Moreover, structural distortions indirectly impact the band gaps, leading to lower gaps in the model systems as compared to the experimental structures.

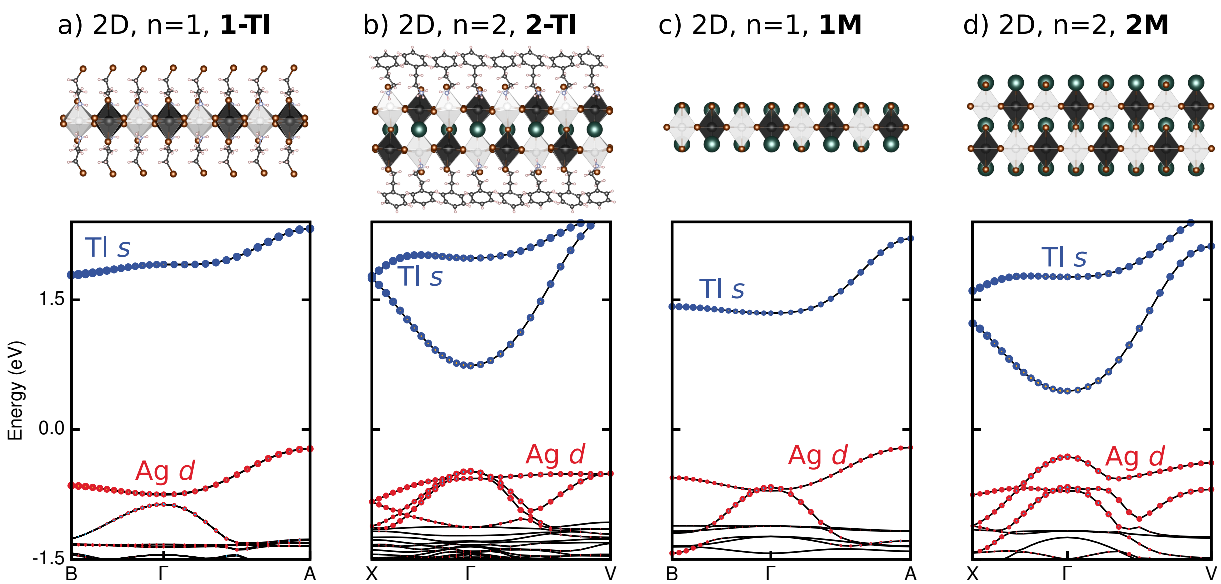

Figure A.5: Electronic band structures of the experimental structures of a) $n = 1$ **1-Tl**, b) $n = 2$ **2-Tl** and the analogous undistorted model systems c) **1M** and d) **2M**, as computed with HSE06 approximation, overlaid with the orbital character of the bands. Note that the halide contributions were omitted for clarity. The corresponding crystal structures are showed on top of each panel to facilitate the comparison.

The $n = 3$ model system used in section 3.5 to demonstrate the preserving of the indirect nature of the band gap in 2D $n \geq 2$ derivatives, was constructed by cutting out a three-octahedra-thick perovskite layer from the 3D parent $Cs_2AgTlBr_6$ and relaxing its structure. The geometry optimisation was performed using DFT in the generalized gradient approximation PBE [67] with the van der Waals corrections computed using Tkatchenko and Scheffler method [354].

A.3. Optical properties of $Cs_2AgB^{III}X_6$ halide double perovskites

All calculations presented in chapter 4 were performed in BerkeleyGW software package [345], using the Tamm-Dancoff approximation (TDA) [45] for the electron-hole interaction kernel K_{eh}, expanded in a set of 22 valence and 22 conduction bands, corresponding to an energy window of at least 8.85 eV. We further note that a Gaussian smearing of 50 meV was applied in the optical absorption spectra.

The optical properties of Ag-pnictogen double perovskites discussed in sections 4.1 and 4.2 were computed by solving the BSE using 16 occupied and 8 unoccupied states. Figure A.6 a) shows that interpolating K_{eh} from a $4 \times 4 \times 4$ coarse **k**-point grid to a fine grid comprising $12 \times 12 \times 12$ **k**-points leads to the exciton binding energy converged to within 10 meV.

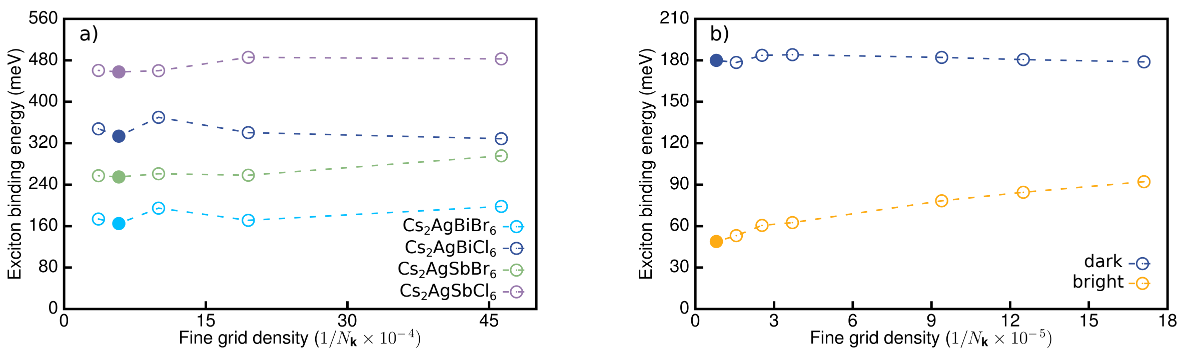

Figure A.6: Binding energy of the first bright excited state as a function of the number of **k**-points used for the interpolation of the kernel for a) Ag-pnictogen and b) $Cs_2AgInCl_6$ double perovskites. Closed symbols represent the values selected to be used further.

The optical properties of $Cs_2AgInCl_6$ double perovskite presented in section 4.5 were obtained by solving BSE with 2 occupied and 1 unoccupied states, yielding a convergent absorption spectrum up to at ∼5 eV above the onset. Because the band edges at the lowest energy direct transition are very disperse, a considerably dense **k**-point grid is required to sample the bands and to accurately interpolate the kernel. Since the BSE calculations are essentially prohibitive for extremely fine grids, to achieve a high density **k**-point mesh, we use the patched sampling scheme, originally described in Ref. [132]. Therefore, in order to achieve **k**-point grids finer than $34 \times 34 \times 34$ points, we diagonalized the BSE Hamiltonian taking into account only **k**-points in a small patch around the Γ point. Figure A.6 b) shows that using an interpolation mesh with $50 \times 50 \times 50$ **k**-points exciton binding energies are converged to within better than 5 meV. However, we note that to be able to represent the optical absorption spectrum the entire Brillouin zone should be sampled. Therefore, the optical absorption spectrum presented in Figure 4.9 was computed using a $34 \times 34 \times 34$

fine grid.

For clarity reasons, a detailed summary of our complete computational setups for the results presented in chapter 4 is showed in Table A.2.

Table A.2: Computational setup and resulting QP band gaps and exciton binding energies for Ag-pnictogen and Ag-In halide double perovskites.

	Input	**Ag-pnictogen**	**Ag-In**
DFT	xc functional	LDA	PBE
	cutoff energy (Ry)	150	60
	k-point grid	$10 \times 10 \times 10$	$10 \times 10 \times 10$
	spin-orbit coupling	yes	no
G_0W_0	ε cutoff (Ry)	10	8
	Σ_c cutoff (Ry)	10	8
	Σ_x cutoff (Ry)	60	48
	bands	600	400
BSE	states in kernel	22 occupied 22 unoccupied	22 occupied 22 unoccupied
	input **k**-point grid	$4 \times 4 \times 4$	$4 \times 4 \times 4$
	interpolation **k**-point grid	$12 \times 12 \times 12$	$50 \times 50 \times 50$
	states on the interpolated grid	16 occupied 8 unoccupied	2 occupied 1 unoccupied

A.4. Halogen migration in $CsPbBr_3$

The structural models depicted in Figure 5.1 of section 5.1 are constructed based on the optimized structure of the experimental high temperature crystal structure of $CsPbBr_3$ with $Pm\bar{3}m$ symmetry. First step in the creation of a surface slab system is establishing the necessary values of the input parameters for a well-converged bulk calculation. The main parameters that influence the computational cost and accuracy are the **k**-point mesh and the energy cutoff of the plane-wave expansion. In order to converge the total energy of the bulk with respect to these two interdependent parameters, one need to first fix one of them at a very large value and converge the total energy with respect to the other one and then interchange the parameters and repeat the procedure. Using this approach, we first fixed the cutoff energy to 500 eV and tested the convergence of the total energy of the bulk with respect to the number of points in the **k**-point grid used to sample the Brillouin zone. Figure A.7 a) shows that a $4 \times 4 \times 4$ **k**-grid lead to a total energy converge within 43 meV. Next, we fixed the **k**-point grid to a mesh of $12 \times 12 \times 12$ points and converged the total energy of the bulk with respect to the cutoff energy. Figure A.7 b) shows that calculations using a cutoff energy of 300 eV yield a total energy with only 1 meV lower than that obtained with the maximum tested value. Last, we performed a geometry optimisation of the bulk structure, using DFT within the PBEsol approximation [350] as implemented in VASP [347, 348]. We also checked the validity of our optimized lattice parameter by computing the total energy of the bulk as a function of different lattice parameters and show in Figure A.7 c) that this convergence test yield the same result. Note that the resulting optimized lattice parameter of 5.86 Å is in very good agreement with the experimental value from X-ray diffraction [355].

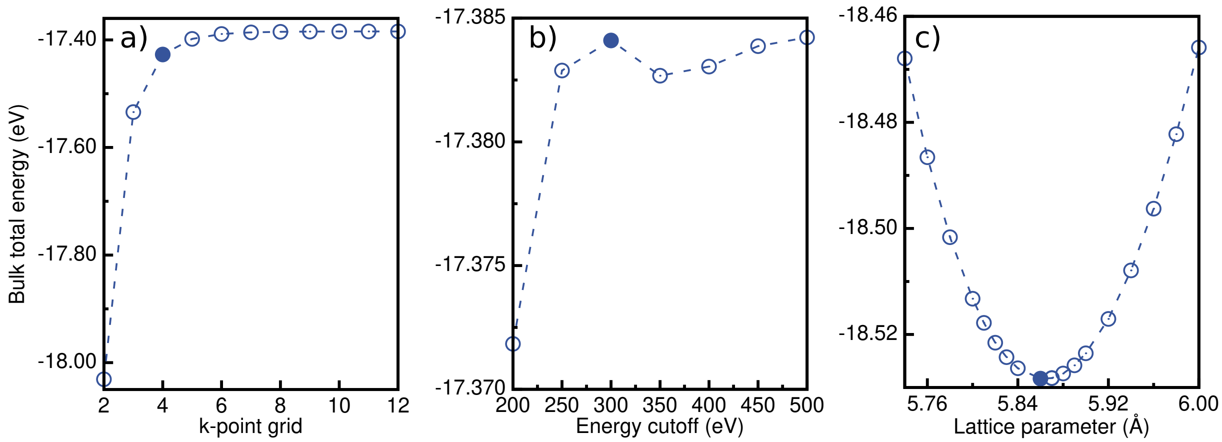

Figure A.7: Total energy of the cubic $CsPbBr_3$ bulk (E_{bulk} in eV) as a function of a) **k**-point grid (in one dimension, with cutoff energy fixed at 500 eV), b) energy cutoff for the plane-wave expansion (with **k**-point grid fixed at $12 \times 12 \times 12$) and c) lattice parameter (with previously determined values for the energy cutoff and **k**-point grid). Closed symbols represent the values selected to be used in our setup.

Second step is the convergence of the surface energy with respect to the slab thickness. The total number of layers in the slab structure must ensure the convergence of the surface energy

$$\sigma = \frac{1}{2}\left(E_{slab} - NE_{bulk}\right) \tag{A.10}$$

where E_{slab} is the total energy of the slab system, E_{bulk} is the energy per atom of the bulk, N is the number of atoms in the surface slab structure and 1/2 pre-factor accounts for the two surfaces of a slab supercell. Furthermore, the effect of fixing layers on the surface energy has also been tested. Figure A.8 a) and b) shows that our unit cell setup featuring 6 total layers, 3 of which fully mobile, grants a surface energy converged to within 25 meV with respect to the slab thickness. Note that, by constraining the bottom layers to the bulk atomic positions, spurious strain is introduced in the structure closer to the fixed layers.

Third, in order to avoid spurious interactions between periodic images, a vacuum layer must be introduced between neighbouring slabs. In Figure A.8 c) we show that our choice

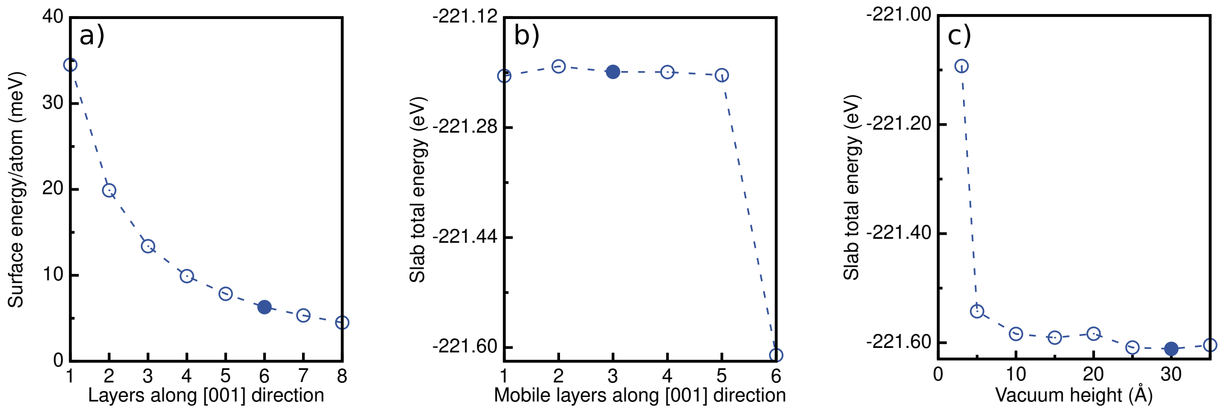

Figure A.8: Surface energy per atom (in meV) a) as a function of number of total layers. Total energy of the supercell featuring 6 layers along out-of-plane [001] direction (E_{slab} in eV) b) as a function of mobile layers and c) as a function of vacuum layer height between adjacent unit cells. Closed symbols represent the values selected to be used in our setup.

of 30 Å of vacuum along the [001] direction is sufficient to cut any interactions between adjacent unit cells.

In summary, all calculation were performed using PAW pseudopotentials [349], a cutoff energy of 300 eV for the plane-wave expansion and a **k**-point grid with $4\times4\times4$ and $4\times4\times1$ points for the bulk and and slab systems, respectively. All structural optimisations were performed with fixed volume and shape of the unit cells and featuring a convergence criterion of at least 0.05 eV/Å for the forces and 10^{-4} eV for the energy.

The migration paths and energies were computed using the climbing-image nudged elastic band (cNEB) method [81] described in section 2.2. We simulated the vacancy-mediate bromine migration using three intermediate images between the fixed initial and final states of the system that have been optimized beforehand. The migration barrier energy has been computed as the difference between the energy of the saddle point and the energy of the initial state of the transition.

To validate our computational setup, we repeated the cNEB calculation of the migration between two adjacent axial positions at the A-terminated surface with five intermediate images and find a migration energy of 0.36 eV, 40 meV lower than our result obtained with three NEB images. The energy profile and migration path are shown in Figure A.9 and are qualitatively similar to our results with three NEB images. This difference between the migration energies can be attributed to slightly different settings that we chose. The calculations with 3 images were done on a $4 \times 4 \times 1$ **k**-grid and optimized with a conjugate gradient algorithm and a convergence criterion of 0.05 eV/Å, while the calculation with 5 images was done on a $2 \times 4 \times 1$ **k**-grid using a LBFGS algorithm and a convergence criterion of 0.001 eV/Å.

Axial-to-axial migration paths have also been reported for cubic (but highly distorted)

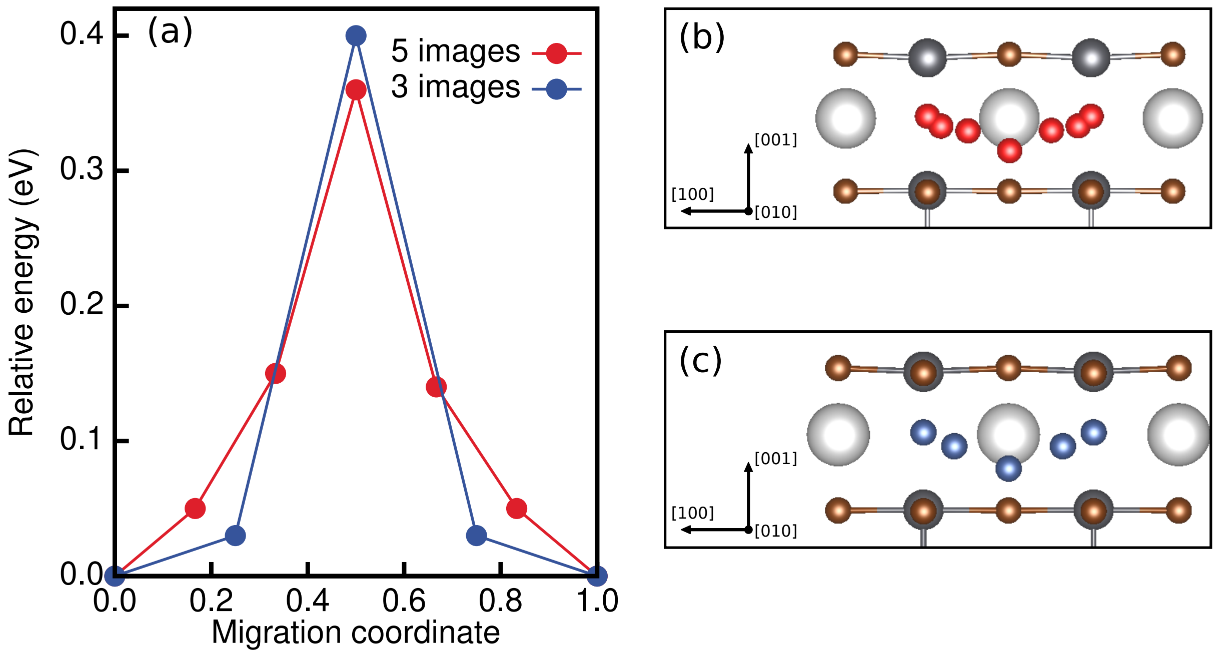

Figure A.9: a) Energy profiles and migration paths for the axial-to-axial migration in L1 of the A-terminated surface, as computed with the cNEB approach using 5 (panel b) and 3 (panel c) intermediate images, respectively. The structures correspond to the average atomic configurations of the two equivalent endpoints of each cNEB calculation overlaid with the position of the migrating Br ion along the migration path.

bulk $MAPbBr_3$ and $FAPbBr_3$ by Oranskaia et al. using 7-13 NEB images [90]. These migration energies are $\sim$0.68 eV and $\sim$0.45 eV (depending on the direction in the distorted unit cell) for $MAPbBr_3$ and $\sim$0.85 eV for $FAPbBr_3$, and the energy profile of the axial-to-axial path looks qualitatively similar to our calculations. Furthermore, more recently Smolders et al. reported migration energies for orthorhombic $CsPbBr_3$ using 4 NEB images, and although absolute values are hard to compare due to different unit cell setups, structural symmetries and differences in the details of the DFT calculations, the energy profile of the axial-to-axial migration path reported in Ref. [308] appear to be qualitatively similar as well. Therefore we conclude that the use of 3 images introduces only a small systematic error in our calculations, but does not change the trends.

In order to confirm that the result of significantly smaller migration energy at the surface than in the bulk is robust, we also test it against the size and symmetry of the slab supercell. Using the same approach, we designed a $2 \times 2 \times 6$ bulk system and $2 \times 2 \times 6$ A-terminated surface slab supercell. First, we calculated the bond length variation upon vacancy introduction in the $2 \times 2 \times 6$ slab unit cell. As expected, the axial compression directly at the surface is smaller in the larger unit cell than that in the $2 \times 1 \times 6$ unit cell. However, Figure A.10 shows that the trends as a function of the surface layer are similar. Generally, the size of distortions will be smaller for larger supercells, but they will not vanish, and hence the migration energies will differ from the ones in the bulk. Similarly, bond length variations in the bulk will also decrease upon going to larger unit cells. Furthermore, both are restricted by the same boundary conditions in the in-plane directions, facilitating the direct comparison between these two dimensional different systems. However, neither the bulk nor the surface models are good representations of real systems in the limit of dilute vacancy concentrations.

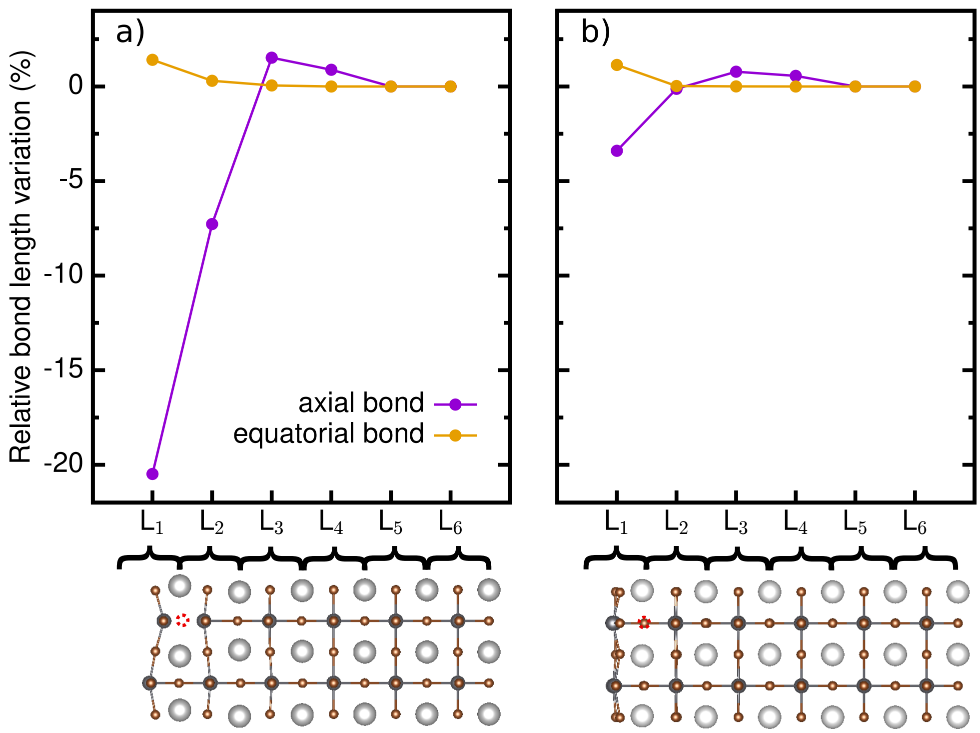

Figure A.10: Relative bond length variation when a Br vacancy is introduced at the A-terminated surface for a) $2 \times 1 \times 6$ unit cell and b) $2 \times 2 \times 6$ unit cell, respectively. The geometry optimized structure is shown below each panel, with the position of the Br vacancy highlighted in red.

Next, by computing the migration energies throughout the A-terminated surface slab of both unit cell setups, we find that the result of a much lower migration energy at the surface also holds for a larger unit cell. The comparison of the migration energies in the two unit cells shown in Table A.3 reveals a 0.17 eV reduction of the migration energy in the bulk and a 0.12 eV reduction of the migration energy at the surface as a consequence of using a larger, symmetric unit cell. The migration energy is smaller for the surface slab than in the bulk. In both unit cell setups, L_2 features the lowest migration energy, followed by a slight increase in L_3. We attribute this finding to an interplay of axial bond length contraction and equatorial bond length elongation at the surface and the slow convergence of the migration energy towards the bulk value to the presence of fixed layers in our surface slab model.

Table A.3: Calculated migration energies (in eV) for a Br vacancy migration across two adjacent axial halide positions in the bulk and in the A-terminated surface slab.

System	**Migration energy (eV)**	
	$2 \times 1 \times 6$	$2 \times 2 \times 6$
bulk	0.65	0.48
slab L_1	0.40	0.28
slab L_2	0.29	0.20
slab L_3	0.30	0.26

List of abbreviations

3-BPA 3-Bromopropylammonium
Ag Silver
BA Butylammonium
Bi Bismuth
Br Bromine
BSE Bethe-Salpeter Equation
CBM Conduction Band Minimum
(c)NEB (climbing-image) Nudged Elastic Band
Cl Chlorine
Cs Caesium
DFT Density Functional Theory
EA Electron Affinity
evGW Eigenvalue Self-consistent *GW*
FA Formamidinium
GPP Generalised Plasmon Pole
HIS Histammonium
(h)TST (harmonic) Transition State Theory
HOMO Highest Occupied Molecular Orbital
HSE xc screened hybrid functional of Heyd, Scuseria and Ernzerhofer
I Iodine
In Indium
IP Ionisation Potential
IPES Inverse Photoelectron Spectroscopy
LDA Local Density Approximation
LED Light Emitting Diode
LUMO Lowest Unoccupied Molecular Orbital
MA Methylammonium

MBPT Many Body Perturbation Theory
MEP Minimum Energy Pathway
PAW Projector Augmented Wave
Pb Lead
PBE xc functional of Perdew, Burke and Ernzerhof
PEA Phenethylamine
PES Photoelectron Spectroscopy
QE Quantum Espresso software package
QP Quasi-Particle
QSGW Quasiparticle Self-consistent *GW*
RP Ruddlesden-Popper
RPA Random Phase Approximation
RT Room Temperature
Sb Antimony
scGW self-consistent *GW*
SCXRD Single-Crystal X-Ray Diffraction
SOC Spin-Orbit Coupling
TDA Tamm-Dancoff Approximation
TDDFT Time-Dependent Density Functional Theory
Tl Thalium
UPS Ultraviolet Photoelectron Spectroscopy
VASP Vienna-Ab-initio-Simulation Package
VBM Valence Band Maximum
WM Wannier-Mott model
xc exchange-correlation

List of publications

1. B. A. Connor, **R.-I. Biega**, L. Leppert, Linn and H. I. Karunadasa. Dimensional reduction of the small-bandgap double perovskite Cs2AgTlBr6. *Chem. Sci.*, **29**, 7708–7715 (2020).

2. **R.-I. Biega**, M. R. Filip, L. Leppert, and J. B. Neaton. Chemically Localized Resonant Excitons in Silver–Pnictogen Halide Double Perovskites. *J. Phys. Chem. Lett.*, **12**, 2057–2063 (2021).

3. **R.-I. Biega** and L. Leppert. Halogen Vacancy Migration at Surfaces of $CsPbBr_3$ Perovskites: Insights from Density Functional Theory. *Journal of Physics: Energy*, **3**, 034017 (2021).

References

[1] International Energy Agency. *International Energy Agency*. 2021. URL: https://www.iea.org/fuels-and-technologies/electricity.

[2] Dorothea Golze et al. "Core-Level Binding Energies from GW: An Efficient Full-Frequency Approach within a Localized Basis". In: *Journal of Chemical Theory and Computation* 14.9 (2018), pp. 4856–4869.

[3] Feliciano Giustino. *Materials modelling using density functional theory*. Oxford Univ. Press, 2014.

[4] Gilbert El-Hajje et al. "Quantification of spatial inhomogeneity in perovskite solar cells by hyperspectral luminescence imaging". In: *Energy Environ. Sci.* 9 (7 2016), pp. 2286–2294.

[5] Qing Sun, Paul Fassl, and Yana Vaynzof. "Large-Scale Compositional and Electronic Inhomogeneities in CH3NH3PbI3 Perovskites and Their Effect on Device Performance". In: *ACS Applied Energy Materials* 1.6 (2018), pp. 2410–2416.

[6] Elizabeth M. Tennyson, Tiarnan A. S. Doherty, and Samuel D. Stranks. "Heterogeneity at multiple length scales in halide perovskite semiconductors". In: *Nature Reviews Materials* 4.9 (2019), pp. 573–587.

[7] T. Sherahilo. *Oxford PV perovskite solar cell achieves 28% efficiency. Oxford PV.* 2018. URL: https://www.oxfordpv.com/news/oxford-pv-perovskite-solar-cell-achieves-28-efficiency.

[8] National Renewable Energy Laboratory. *Best Research-Cell Efficiencies*. 2021. URL: https://www.nrel.gov/pv/assets/pdfs/best-research-cell-efficiencies.20200104.pdf.

[9] Stefaan De Wolf et al. "Organometallic Halide Perovskites: Sharp Optical Absorption Edge and Its Relation to Photovoltaic Performance". In: *The Journal of Physical Chemistry Letters* 5.6 (2014), pp. 1035–1039.

[10] Samuel D. Stranks et al. "Electron-Hole Diffusion Lengths Exceeding 1 Micrometer in an Organometal Trihalide Perovskite Absorber". In: *Science* 342.6156 (2013), pp. 341–344.

[11] Tingting Shi et al. "Unipolar self-doping behavior in perovskite $CH_3NH_3PbBr_3$". In: *Applied Physics Letters* 106.10 (2015), p. 103902.

[12] Li Na Quan et al. "Perovskites for Next-Generation Optical Sources". In: *Chemical Reviews* 119.12 (2019), pp. 7444–7477.

[13] Alessandro Senocrate et al. "Thermochemical Stability of Hybrid Halide Perovskites". In: *ACS Energy Letters* 4.12 (2019), pp. 2859–2870.

[14] Hsinhan Tsai et al. "High-efficiency two-dimensional Ruddlesden–Popper perovskite solar cells". In: *Nature* 536.7616 (2016), pp. 312–316.

[15] Feliciano Giustino and Henry J. Snaith. "Toward Lead-Free Perovskite Solar Cells". In: *ACS Energy Lett.* 1.6 (2016), pp. 5359–5363.

[16] George Volonakis et al. "Lead-Free Halide Double Perovskites via Heterovalent Substitution of Noble Metals". In: *J. Phys. Chem. Lett.* 7 (2016), pp. 1254–1259.

[17] Jacky Even et al. "Importance of Spin–Orbit Coupling in Hybrid Organic/Inorganic Perovskites for Photovoltaic Applications". In: *J. Phys. Chem. Lett.* 4.17 (2013), pp. 2999–3005.

[18] Giacomo Giorgi et al. "Small Photocarrier Effective Masses Featuring Ambipolar Transport in Methylammonium Lead Iodide Perovskite: A Density Functional Analysis". In: *J. Phys. Chem. Lett.* 4.24 (2013), pp. 4213–4216.

[19] Jing Feng and Bing Xiao. "Crystal Structures, Optical Properties, and Effective Mass Tensors of CH3NH3PbX3 (X = I and Br) Phases Predicted from HSE06". In: *J. Phys. Chem. Lett.* 5.7 (2014), pp. 1278–1282.

[20] Jun Nagamatsu et al. "Superconductivity at 39 K in magnesium diboride". In: *Nature* 410 (6824 2001), pp. 63–63.

[21] R. Car and M. Parrinello. "Unified Approach for Molecular Dynamics and Density-Functional Theory". In: *Phys. Rev. Lett.* 55 (22 1985), pp. 2471–2474.

[22] Jean-Yves Raty and Giulia Galli. "Ultradispersity of diamond at the nanoscale". In: *Nature Materials* 2 (12 2003), pp. 792–795.

[23] Marina R. Filip and Feliciano Giustino. "Computational Screening of Homovalent Lead Substitution in Organic–Inorganic Halide Perovskites". In: *J. Phys. Chem. C* 120.1 (2016), pp. 166–173.

[24] C. S. Wang and Warren E. Pickett. "Density-Functional Theory of Excitation Spectra of Semiconductors: Application to Si". In: *Phys. Rev. Lett.* 51.7 (1983), p. 597.

[25] Jacky Even et al. “Density-Functional Theory for Time-Dependent Systems”. In: *Phys. Rev. Lett.* 52.12 (1984), p. 997.

[26] Lars Hedin. “New Method for Calculating the One-Particle Green’s Function with Application to the Electron-Gas Problem”. In: *Phys. Rev.* 139 (1965), A796.

[27] A.L. Fetter and J.D. Walecka. *Quantum Theory of Many-Particle Systems*. New York: MacGraw-Hill, 1971.

[28] Lars Hedin. “On correlation effects in electron spectroscopies and the GW approximation”. In: *J. Phys.: Condens. Matter* 11 (1999), R489.

[29] Michael Rohlfing and Steven G. Louie. “Electron-hole excitations and optical spectra from first principles”. In: *Phys. Rev. B* 62.8 (2000), p. 4927.

[30] G. Strinati, H. J. Mattausch, and W. Hanke. “Dynamical correlation effects on the quasiparticle bloch states of a covalent crystal”. In: *Phys. Rev. Lett.* 45.4 (1980), pp. 290–294.

[31] Mark S. Hybertsen and Steven G. Louie. “First-principles theory of quasiparticles: Calculation of band gaps in semiconductors and insulators”. In: *Phys. Rev. Lett.* 55.13 (1985), pp. 1418–1421.

[32] F. Aryasetiawan and O. Gunnarson. “The GW method”. In: *Rep. Prog. Phys.* 61 (1998), p. 237.

[33] Isaac Tamblyn et al. “Electronic energy level alignment at metal-molecule interfaces with a GW approach”. In: *Phys. Rev. B* 84.20 (2011), p. 201402.

[34] Michiel J van Setten et al. “GW 100: Benchmarking G0W0 for Molecular Systems”. In: *J. Chem. Theory Comput.* 11.12 (2015), pp. 5665–5687.

[35] Sahar Sharifzadeh et al. “Low-Energy Charge-Transfer Excitons in Organic Solids from First-Principles: The Case of Pentacene”. In: *J. Phys. Chem. Lett.* 4.13 (2013), p. 2197.

[36] Tonatiuh Rangel et al. “An assessment of low-lying excitation energies and triplet instabilities of organic molecules with an ab initio Bethe-Salpeter equation approach and the Tamm-Dancoff approximation”. In: *The Journal of Chemical Physics* 146.19 (2017), p. 194108.

[37] Dahvyd Wing et al. “Comparing time-dependent density functional theory with many-body perturbation theory for semiconductors: Screened range-separated hybrids and the *GW* plus Bethe-Salpeter approach”. In: *Phys. Rev. Materials* 3 (6 2019), p. 064603.

[38] M. C. Payne et al. “Iterative minimization techniques for ab initio total-energy calculations: molecular dynamics and conjugate gradients”. In: *Rev. Mod. Phys.* 64 (4 1992), pp. 1045–1097.

[39] R. M. Martin. *Electronic structure: basic theory and practical methods*. Cambridge Univ. Press, 2004.

[40] Lars Hedin and Stig O. Lundqvist. “Effects of Electron-Electron and Electron-Phonon Interactions on the One-Electron States of Solids”. In: *Solid State Physics*. Vol. 23. United States: Academinc Press, 1969, pp. 1–181.

[41] John C Inkson. *Many-Body Theory of Solids*. Springer, 1984.

[42] Mark S. Hybertsen and Steven G. Louie. “Electron correlation in semiconductors and insulators: Band gaps and quasiparticle energies”. In: *Phys. Rev. B* 34 (8 1986), pp. 5390–5413.

[43] G. Strinati. “Application of the Green’s functions method to the study of the optical properties of semiconductors”. In: *La Rivista del Nuovo Cimento (1978-1999)* 11 (12 1988), pp. 1–86.

[44] Giovanni Onida, Lucia Reining, and Angel Rubio. “Electronic excitations: density-functional versus many-body Green’s-function approaches”. In: *Rev. Mod. Phys.* 74.April (2002), p. 601.

[45] Leeor Kronik and Jeffrey B. Neaton. “Excited-State Properties of Molecular Solids from First Principles”. In: *Annual Review of Physical Chemistry* 67.1 (2016), pp. 587–616.

[46] P. Hohenberg and W. Kohn. “Inhomogeneous Electron Gas”. In: *Phys. Rev.* 136 (3B 1964), B864–B871.

[47] M. Born and R. Oppenheimer. “Zur Quantentheorie der Molekeln”. In: *Annalen der Physik* 389.20 (1927), pp. 457–484.

[48] L. H. Thomas. “The calculation of atomic fields”. In: *Mathematical Proceedings of the Cambridge Philosophical Society* 23.5 (1927), pp. 542–548.

[49] E. Fermi. “Eine statistische Methode zur Bestimmung einiger Eigenschaften des Atoms und ihre Anwendung auf die Theorie des periodischen Systems der Elemente”. In: *Zeitschrift für Physik* 48.1 (1928), pp. 73–79.

[50] D. R. Hartree. “The Wave Mechanics of an Atom with a Non-Coulomb Central Field. Part II. Some Results and Discussion”. In: *Mathematical Proceedings of the Cambridge Philosophical Society* 24.1 (1928), pp. 111–132.

[51] Linus. Pauling. “The Application of the Quantum Mechanics to the Structure of the Hydrogen Molecule and Hydrogen Molecule-Ion and to Related Problems.” In: *Chemical Reviews* 5.2 (1928), pp. 173–213.

[52] J. C. Slater. “The Theory of Complex Spectra”. In: *Phys. Rev.* 34 (10 1929), pp. 1293–1322.

[53] V. Fock. “Näherungsmethode zur Lösung des quantenmechanischen Mehrkörperproblems”. In: *Zeitschrift für Physik* 61 (1 1930), pp. 126–148.

[54] W. Kohn and L. J. Sham. “Self-Consistent Equations Including Exchange and Correlation Effects”. In: *Phys. Rev.* 140 (4A 1965), A1133–A1138.

[55] E. Merzbacher. *Quantum mechanics (3rd edn)*. Wiley, New York, 1998.

[56] L. H. Thomas. “The Motion of the Spinning Electron”. In: *Nature* 117.2945 (1926), pp. 514–514.

[57] A. Messiah. *Quantum Mechanics, vol. II.* Dover Publications, Inc., 1999.

[58] P. A. M. Dirac. “The Quantum Theory of the Electron”. In: *Proceedings of the Royal Society of London. Series A, Containing Papers of a Mathematical and Physical Character* 117.778 (1927), pp. 610–624.

[59] U. von Barth and L. Hedin. “A local exchange-correlation potential for the spin polarized case. i”. In: *Journal of Physics C: Solid State Physics* 5.13 (1972), pp. 1629–1642.

[60] Stephan Kümmel and Leeor Kronik. “Orbital-dependent density functionals: Theory and applications”. In: *Rev. Mod. Phys.* 80 (1 2008), pp. 3–60.

[61] D. M. Ceperley and B. J. Alder. “Ground State of the Electron Gas by a Stochastic Method”. In: *Phys. Rev. Lett.* 45.7 (1980), pp. 566–569.

[62] J. P. Perdew and Alex Zunger. “Self-interaction correction to density-functional approximations for many-electron systems”. In: *Phys. Rev. B* 23.10 (1981), pp. 5048–5079.

[63] P. A. M. Dirac. “Note on Exchange Phenomena in the Thomas Atom”. In: *Mathematical Proceedings of the Cambridge Philosophical Society* 26.3 (1930), pp. 376–385.

[64] J. C. Slater. “A Simplification of the Hartree-Fock Method”. In: *Phys. Rev.* 81 (3 1951), pp. 385–390.

[65] S. H. Vosko, L. Wilk, and M. Nusair. “Accurate spin-dependent electron liquid correlation energies for local spin density calculations: a critical analysis”. In: *Canadian Journal of Physics* 58.8 (1980), pp. 1200–1211.

[66] John P. Perdew and Yue Wang. “Accurate and simple analytic representation of the electron-gas correlation energy”. In: *Phys. Rev. B* 45 (23 1992), pp. 13244–13249.

[67] John P. Perdew, Kieron Burke, and Matthias Ernzerhof. “Generalized Gradient Approximation Made Simple”. In: *Phys. Rev. Lett.* 77 (18 1996), pp. 3865–3868.

[68] A. D. Becke. “Density-functional exchange-energy approximation with correct asymptotic behavior”. In: *Phys. Rev. A* 38 (6 1988), pp. 3098–3100.

[69] C. Lee, W. Yang, and R. G. Parr. "Development of the Colle-Salvetti correlation-energy formula into a functional of the electron density". In: *Phys. Rev. B Condens. Matter.* 15 (37 1988), pp. 785–789.

[70] Axel D. Becke. "A new mixing of Hartree-Fock and local density-functional theories". In: *The Journal of Chemical Physics* 98.2 (1993), pp. 1372–1377.

[71] Mel Levy. "Electron densities in search of Hamiltonians". In: *Phys. Rev. A* 26 (3 1982), pp. 1200–1208.

[72] Carlo Adamo and Vincenzo Barone. "Toward reliable density functional methods without adjustable parameters: The PBE0 model". In: *The Journal of Chemical Physics* 110.13 (1999), pp. 6158–6170.

[73] Jochen Heyd, Gustavo E. Scuseria, and Matthias Ernzerhof. "Hybrid functionals based on a screened Coulomb potential". In: *The Journal of Chemical Physics* 118.18 (2003), pp. 8207–8215.

[74] Alejandro J. Garza and Gustavo E. Scuseria. "Predicting Band Gaps with Hybrid Density Functionals". In: *The Journal of Physical Chemistry Letters* 7.20 (2016), pp. 4165–4170.

[75] Pedro Borlido et al. "Large-Scale Benchmark of Exchange–Correlation Functionals for the Determination of Electronic Band Gaps of Solids". In: *Journal of Chemical Theory and Computation* 15.9 (2019), pp. 5069–5079.

[76] Pedro Borlido et al. "Exchange-correlation functionals for band gaps of solids: benchmark, reparametrization and machine learning". In: *npj Computational Materials* 6.1 (2020), p. 96.

[77] Aliaksandr V. Krukau et al. "Influence of the exchange screening parameter on the performance of screened hybrid functionals". In: *The Journal of Chemical Physics* 125.22 (2006), p. 224106.

[78] Hannes Jónsson, Greg Mills, and Karsten W. Jacobsen. "Nudged elastic band method for finding minimum energy paths of transitions". In: *Classical and Quantum Dynamics in Condensed Phase Simulations*. 1998, pp. 385–404.

[79] Arthur F. Voter and Jimmie D. Doll. "Dynamical corrections to transition state theory for multistate systems: Surface self-diffusion in the rare-event regime". In: *The Journal of Chemical Physics* 82.1 (1985), pp. 80–92.

[80] Graeme Henkelman and Hannes Jónsson. "Improved tangent estimate in the nudged elastic band method for finding minimum energy paths and saddle points". In: *The Journal of Chemical Physics* 113.22 (2000), pp. 9978–9985.

[81] G. Henkelman and H. Jónsson. "A climbing image nudged elastic band method for finding saddle points and minimum energy paths". In: *J. Chem. Phys.* 113 (2000), pp. 9901–9904.

[82] W. Windl et al. “First-Principles Study of Boron Diffusion in Silicon”. In: *Phys. Rev. Lett.* 83 (21 1999), pp. 4345–4348.

[83] Blas P. Uberuaga et al. “Diffusion of Ge below the Si(100) Surface: Theory and Experiment”. In: *Phys. Rev. Lett.* 84 (11 2000), pp. 2441–2444.

[84] T.-C. Shen, J. A. Steckel, and K. D. Jordan. “Electron-stimulated bond rearrangements on the H/Si(100)-3×1 surface”. In: *Surface Science* 446.3 (2000), pp. 211–218.

[85] Marie Villarba and Hannes Jónsson. “Diffusion mechanisms relevant to metal crystal growth: Pt/Pt(111)”. In: *Surface Science* 317.1 (1994), pp. 15–36.

[86] Marie Villarba and Hannes Jónsson. “Atomic exchange processes in sputter deposition of Pt on Pt(111)”. In: *Surface Science* 324.1 (1995), pp. 35–46.

[87] M. Saiful Islam. “Ionic transport in ABO3 perovskite oxides: a computer modelling tour”. In: *J. Mater. Chem.* 10 (4 2000), pp. 1027–1038.

[88] Christopher Eames et al. “Ionic transport in hybrid lead iodide perovskite solar cells”. In: *Nature Communications* 6.1 (2015), p. 7497.

[89] Simone Meloni et al. “Ionic polarization-induced current-voltage hysteresis in CH3NH3PbX3 perovskite solar cells”. In: *Nature Communications* 7.1 (2016), p. 10334.

[90] Aleksandra Oranskaia et al. “Halogen Migration in Hybrid Perovskites: The Organic Cation Matters”. In: *Journal of Physical Chemistry Letters* 9.18 (2018), pp. 5474–5480.

[91] Daniele Meggiolaro, Edoardo Mosconi, and Filippo De Angelis. “Formation of Surface Defects Dominates Ion Migration in Lead-Halide Perovskites”. In: *ACS Energy Lett.* 4.3 (2019), pp. 779–785.

[92] L. J. Sham and M. Schlüter. “Density-Functional Theory of the Energy Gap”. In: *Phys. Rev. Lett.* 51 (20 1983), pp. 1888–1891.

[93] J. Paier et al. “Screened hybrid density functionals applied to solids”. In: *The Journal of Chemical Physics* 124.15 (2006), p. 154709.

[94] Fabien Tran and Peter Blaha. “Accurate Band Gaps of Semiconductors and Insulators with a Semilocal Exchange-Correlation Potential”. In: *Phys. Rev. Lett.* 102 (22 2009), p. 226401.

[95] Linn Leppert, Tonatiuh Rangel, and Jeffrey B. Neaton. “Towards predictive band gaps for halide perovskites: Lessons from one-shot and eigenvalue self-consistent GW”. In: *Phys. Rev. Materials* 3.10 (2019), p. 103803.

[96] E. W. Plummer and W. Eberhardt. “Angle-Resolved Photoemission as a Tool for the Study of Surfaces”. In: *Advances in Chemical Physics*. John Wiley & Sons, Ltd, 1982, pp. 533–656.

[97] F. J. Himpsel. “Angle-resolved measurements of the photoemission of electrons in the study of solids”. In: *Advances in Physics* 32.1 (1983), pp. 1–51.

[98] Stephen Douglas Kevan. *Angle-resolved photoemission: theory and current applications*. Elsevier, 1992.

[99] Dorothea Golze, Marc Dvorak, and Patrick Rinke. “The GW Compendium: A Practical Guide to Theoretical Photoemission Spectroscopy”. In: *Frontiers in Chemistry* 7 (2019), p. 377.

[100] V. Dose. “Momentum-resolved inverse photoemission”. In: *Surface Science Reports* 5.8 (1985), pp. 337–378.

[101] N. V. Smith. “Inverse photoemission”. In: *Reports on Progress in Physics* 51.9 (1988), pp. 1227–1294.

[102] John C. Fuggle and John E. (eds.) Inglesfield. *Unoccupied Electronic States*. Berlin: Springer-Verlag, 1992.

[103] Carl-Olof Almbladh and Lars Hedin. “Beyond the One-Electron Model. Many-Body Effects in Atoms, Molecules, and Solids”. In: *Handbook of Synchrotron Radiation*. Vol. 1b. North-Holland, 1983, pp. 607–904.

[104] G. C. Wick. “The Evaluation of the Collision Matrix”. In: *Phys. Rev.* 80 (2 1950), pp. 268–272.

[105] Wilfried G. Aulbur, Lars Jönsson, and John W. Wilkins. “Quasiparticle Calculations in Solids”. In: *Journal of Physics C: Solid State Physics* 54 (2000), pp. 1–218.

[106] Stephen L. Adler. “Quantum Theory of the Dielectric Constant in Real Solids”. In: *Phys. Rev.* 126 (2 1962), pp. 413–420.

[107] Nathan Wiser. “Dielectric Constant with Local Field Effects Included”. In: *Phys. Rev.* 129 (1 1963), pp. 62–69.

[108] F. Fuchs et al. “Quasiparticle band structure based on a generalized Kohn-Sham scheme”. In: *Phys. Rev. B* 76 (11 2007), p. 115109.

[109] Emmanouil Kioupakis et al. “*GW* quasiparticle corrections to the $\mathrm{LDA}+U/\mathrm{GGA}+U$ electronic structure of bcc hydrogen”. In: *Phys. Rev. B* 77 (15 2008), p. 155114.

[110] Christopher E Patrick and Feliciano Giustino. “GW quasiparticle band gaps of anatase TiO_2 starting from DFT +U”. In: *Journal of Physics: Condensed Matter* 24.20 (2012), p. 202201.

[111] Fabien Bruneval and Miguel A. L. Marques. “Benchmarking the Starting Points of the GW Approximation for Molecules”. In: *Journal of Chemical Theory and Computation* 9.1 (2013), pp. 324–329.

[112] Noa Marom et al. "Benchmark of GW methods for azabenzenes". In: *Phys. Rev. B* 86 (24 2012), p. 245127.

[113] X. Blase, C. Attaccalite, and V. Olevano. "First-principles GW calculations for fullerenes, porphyrins, phtalocyanine, and other molecules of interest for organic photovoltaic applications". In: *Phys. Rev. B* 83 (11 2011), p. 115103.

[114] Jan Wilhelm, Mauro Del Ben, and Jürg Hutter. "GW in the Gaussian and Plane Waves Scheme with Application to Linear Acenes". In: *Journal of Chemical Theory and Computation* 12.8 (2016), pp. 3623–3635.

[115] M. Shishkin and G. Kresse. "Self-consistent GW calculations for semiconductors and insulators". In: *Phys. Rev. B* 75 (23 2007), p. 235102.

[116] Matteo Gatti et al. "Understanding Correlations in Vanadium Dioxide from First Principles". In: *Phys. Rev. Lett.* 99 (26 2007), p. 266402.

[117] Irene Aguilera et al. "First-principles study of the band structure and optical absorption of $CuGaS_2$". In: *Phys. Rev. B* 84 (8 2011), p. 085145.

[118] Manish Jain et al. "Improved quasiparticle wave functions and mean field for G_0W_0 calculations: Initialization with the COHSEX operator". In: *Phys. Rev. B* 90 (11 2014), p. 115148.

[119] Joseph W. Knight et al. "Accurate Ionization Potentials and Electron Affinities of Acceptor Molecules III: A Benchmark of GW Methods". In: *Journal of Chemical Theory and Computation* 12.2 (2016), pp. 615–626.

[120] B. Holm and U. von Barth. "Fully self-consistent GW self-energy of the electron gas". In: *Phys. Rev. B* 57 (4 1998), pp. 2108–2117.

[121] P. García-González and R. W. Godby. "Self-consistent calculation of total energies of the electron gas using many-body perturbation theory". In: *Phys. Rev. B* 63 (7 2001), p. 075112.

[122] Wolf-Dieter Schöne and Adolfo G. Eguiluz. "Self-Consistent Calculations of Quasiparticle States in Metals and Semiconductors". In: *Phys. Rev. Lett.* 81 (8 1998), pp. 1662–1665.

[123] Manuel Grumet et al. "Beyond the quasiparticle approximation: Fully self-consistent GW calculations". In: *Phys. Rev. B* 98 (15 2018), p. 155143.

[124] Adrian Stan, Nils Erik Dahlen, and Robert van Leeuwen. "Levels of self-consistency in the GW approximation". In: *The Journal of Chemical Physics* 130.11 (2009), p. 114105.

[125] C. Rostgaard, K. W. Jacobsen, and K. S. Thygesen. "Fully self-consistent GW calculations for molecules". In: *Phys. Rev. B* 81 (8 2010), p. 085103.

[126] F. Caruso et al. "Unified description of ground and excited states of finite systems: The self-consistent *GW* approach". In: *Phys. Rev. B* 86 (8 2012), p. 081102.

[127] Fabio Caruso et al. "Self-consistent *GW*: All-electron implementation with localized basis functions". In: *Phys. Rev. B* 88 (7 2013), p. 075105.

[128] M. Strange et al. "Self-consistent GW calculations of electronic transport in thiol- and amine-linked molecular junctions". In: *Phys. Rev. B* 83 (11 2011), p. 115108.

[129] Ferdi Aryasetiawan and Silke Biermann. "Generalized Hedin equations and *GW* approximation for quantum many-body systems with spin-dependent interactions". In: *Journal of Physics: Condensed Matter* 21.6 (2009), p. 064232.

[130] F. Aryasetiawan and S. Biermann. "Generalized Hedin's Equations for Quantum Many-Body Systems with Spin-Dependent Interactions". In: *Phys. Rev. Lett.* 100 (11 2008), p. 116402.

[131] Giovanni Onida et al. "Ab Initio Calculations of the Quasiparticle and Absorption Spectra of Clusters: The Sodium Tetramer". In: *Phys. Rev. Lett.* 75 (5 1995), pp. 818–821.

[132] Michael Rohlfing and Steven G. Louie. "Electron-Hole Excitations in Semiconductors and Insulators". In: *Phys. Rev. Lett.* 81 (11 1998), pp. 2312–2315.

[133] Lorin X. Benedict and Eric L. Shirley. "Ab initio calculation of $\epsilon_2(\omega)$ including the electron-hole interaction: Application to GaN and CaF_2". In: *Phys. Rev. B* 59 (8 1999), pp. 5441–5451.

[134] Sabine Körbel et al. "Benchmark Many-Body GW and Bethe–Salpeter Calculations for Small Transition Metal Molecules". In: *Journal of Chemical Theory and Computation* 10.9 (2014), pp. 3934–3943.

[135] Fabien Bruneval and Jeffrey B. Hamed Samia M.and Neaton. "A systematic benchmark of the ab initio Bethe-Salpeter equation approach for low-lying optical excitations of small organic molecules". In: *The Journal of Chemical Physics* 142.24 (2015), p. 244101.

[136] Denis Jacquemin, Ivan Duchemin, and Xavier Blase. "Benchmarking the Bethe–Salpeter Formalism on a Standard Organic Molecular Set". In: *Journal of Chemical Theory and Computation* 11.7 (2015), pp. 3290–3304.

[137] Hannu-Pekka Komsa and Arkady V. Krasheninnikov. "Effects of confinement and environment on the electronic structure and exciton binding energy of MoS_2 from first principles". In: *Phys. Rev. B* 86 (24 2012), p. 241201.

[138] Diana Y. Qiu, Felipe H. da Jornada, and Steven G. Louie. "Optical Spectrum of MoS_2: Many-Body Effects and Diversity of Exciton States". In: *Phys. Rev. Lett.* 111 (21 2013), p. 216805.

[139] Hongliang Shi et al. “Quasiparticle band structures and optical properties of strained monolayer MoS_2 and WS_2”. In: *Phys. Rev. B* 87 (15 2013), p. 155304.

[140] Miguel M. Ugeda et al. “Giant bandgap renormalization and excitonic effects in a monolayer transition metal dichalcogenide semiconductor”. In: *Nature Materials* 13 (12 2014), pp. 1091–1095.

[141] Marc Dvorak and Zhigang Wu. “Tunable many-body interactions in semiconducting graphene: Giant excitonic effect and strong optical absorption”. In: *Phys. Rev. B* 92 (3 2015), p. 035422.

[142] Diana Y. Qiu, Felipe H. da Jornada, and Steven G. Louie. “Screening and many-body effects in two-dimensional crystals: Monolayer MoS_2”. In: *Phys. Rev. B* 93 (23 2016), p. 235435.

[143] A. Schleife et al. “Tin dioxide from first principles: Quasiparticle electronic states and optical properties”. In: *Phys. Rev. B* 83 (3 2011), p. 035116.

[144] Patrick Rinke et al. “First-Principles Optical Spectra for F Centers in MgO”. In: *Phys. Rev. Lett.* 108 (12 2012), p. 126404.

[145] Paul Erhart et al. “Quasiparticle spectra, absorption spectra, and excitonic properties of NaI and SrI_2 from many-body perturbation theory”. In: *Phys. Rev. B* 89 (7 2014), p. 075132.

[146] André Schleife et al. “Optical properties of In2O3 from experiment and first-principles theory: influence of lattice screening”. In: *New Journal of Physics* 20.5 (2018), p. 053016.

[147] Sebastian Rieger et al. “Excitons and narrow bands determine the optical properties of cesium bismuth halides”. In: *Phys. Rev. B* 100 (2019), 201404(R).

[148] Maurizia Palummo et al. “Optical Properties of Lead-Free Double Perovskites by Ab Initio Excited-State Methods”. In: *ACS Energy Lett.* 5 (2020), pp. 457–463.

[149] Raisa-Ioana Biega et al. “Chemically Localized Resonant Excitons in Silver–Pnictogen Halide Double Perovskites”. In: *The Journal of Physical Chemistry Letters* 12.8 (2021), pp. 2057–2063.

[150] Samrana Kazim et al. “Perovskite as Light Harvester: A Game Changer in Photovoltaics”. In: *Angewandte Chemie International Edition* 53.11 (2014), pp. 2812–2824.

[151] V. M. Goldschmidt. “Die Gesetze der Krystallochemie”. In: *Naturwissenschaften* 14.21 (1926), pp. 477–485.

[152] A. G. Chynoweth. “Surface Space-Charge Layers in Barium Titanate”. In: *Phys. Rev.* 102 (3 1956), pp. 705–714.

[153] David B. Mitzi. “Templating and structural engineering in organic inorganic perovskites”. In: *J. Chem. Soc., Dalton Trans.* (1 2001), pp. 1–12.

[154] Peng Gao, Michael Grätzel, and Mohammad K. Nazeeruddin. “Organo- halide lead perovskites for photovoltaic applications”. In: *Energy Environ. Sci.* 7 (8 2014), pp. 2448–2463.

[155] F. S. Chen. “Optically Induced Change of Refractive Indices in LiNbO3 and LiTaO3”. In: *Journal of Applied Physics* 40.8 (1969), pp. 3389–3396.

[156] Yasunobu Inoue et al. “Photoassisted water decomposition by ferroelectric lead zirconate titanate ceramics with anomalous photovoltaic effects”. In: *The Journal of Physical Chemistry* 90.13 (1986), pp. 2809–2810.

[157] Meng Qin, Kui Yao, and Yung C. Liang. “High efficient photovoltaics in nanoscaled ferroelectric thin films”. In: *Applied Physics Letters* 93.12 (2008), p. 122904.

[158] Marin Alexe and Dietrich Hesse. “Tip-enhanced photovoltaic effects in bismuth ferrite”. In: *Nature Communications* 2.1 (2011), p. 256.

[159] Steve M. Young and Andrew M. Rappe. “First Principles Calculation of the Shift Current Photovoltaic Effect in Ferroelectrics”. In: *Phys. Rev. Lett.* 109 (11 2012), p. 116601.

[160] Steve M. Young, Fan Zheng, and Andrew M. Rappe. “First-Principles Calculation of the Bulk Photovoltaic Effect in Bismuth Ferrite”. In: *Phys. Rev. Lett.* 109 (23 2012), p. 236601.

[161] Dawei Cao et al. “High-Efficiency Ferroelectric-Film Solar Cells with an n-type Cu2O Cathode Buffer Layer”. In: *Nano Letters* 12.6 (2012), pp. 2803–2809.

[162] Ilya Grinberg et al. “Perovskite oxides for visible-light-absorbing ferroelectric and photovoltaic materials”. In: *Nature* 203.7477 (2013), pp. 509–512.

[163] Ming Wu et al. “Ni-doped SrBi2Nb2O9 – Perovskite oxides with reduced band gap and stable ferroelectricity for photovoltaic applications”. In: *Journal of Alloys and Compounds* 724 (2017), pp. 1093–1100.

[164] Arashdeep Singh Thind et al. “KBaTeBiO6: A Lead-Free, Inorganic Double Perovskite Semiconductor for Photovoltaic Applications”. In: *Chemistry of Materials* 31.13 (2019), pp. 4769–4778.

[165] Wan-Jian Yin et al. “Oxide perovskites, double perovskites and derivatives for electrocatalysis, photocatalysis,and photovoltaics”. In: *Energy Environ. Sci.* 12 (2 2019), pp. 442–462.

[166] Teruya Ishihara, Jun Takahashi, and Takenari Goto. “Exciton state in two dimensional perovskite semiconductor (C10H21NH3)2PbI4”. In: *Solid State Communications* 69.9 (1989), pp. 933–936.

[167] David B. Mitzi. “Synthesis, Crystal Structure, and Optical and Thermal Properties of (C4H9NH3)2MI4 (M = Ge, Sn, Pb)”. In: *Chemistry of Materials* 8.3 (1996), pp. 791–800.

[168] G. C. Papavassiliou and I.B. Koutselas. “Structural, optical and related properties of some natural three- and lower-dimensional semiconductor systems”. In: *Synthetic Metals* 71.1 (1995). Proceedings of the International Conference on Science and Technology of Synthetic Metals (ICSM ’94), pp. 1713–1714.

[169] J. Calabrese et al. “Preparation and characterization of layered lead halide compounds”. In: *Journal of the American Chemical Society* 113.6 (1991), pp. 2328–2330.

[170] Akihiro Kojima et al. “Organometal Halide Perovskites as Visible-Light Sensitizers for Photovoltaic Cells”. In: *Journal of the American Chemical Society* 131.17 (2009), pp. 6050–6051.

[171] Hui-Seon Kim et al. “Lead Iodide Perovskite Sensitized All-Solid-State Submicron Thin Film Mesoscopic Solar Cell with Efficiency Exceeding 9%”. In: *Scientific Reports* 2.1 (2012), p. 591.

[172] Michael M. Lee et al. “Efficient Hybrid Solar Cells Based on Meso-Superstructured Organometal Halide Perovskites”. In: *Science* 338.6107 (2012), pp. 643–647.

[173] A. M. Glazer. “The classification of tilted octahedra in perovskites”. In: *Acta Crystallographica Section B* 28.11 (1972), pp. 3384–3392.

[174] A. M. Glazer. “Simple ways of determining perovskite structures”. In: *Acta Crystallographica Section A* 31.6 (1975), pp. 756–762.

[175] P. M. Woodward. “Octahedral Tilting in Perovskites. I. Geometrical Considerations”. In: *Acta Crystallographica Section B* 53.1 (1997), pp. 32–43.

[176] Helen D. Megaw. “Changes in Polycrystalline Barium-Strontium Titanate at its Transition Temperature”. In: *Nature* 157.3975 (1946), pp. 20–21.

[177] Christopher J. Howard and Harold T. Stokes. “Structures and phase transitions in perovskites – a group-theoretical approach”. In: *Acta Crystallographica Section A* 61.1 (2005), pp. 93–111.

[178] C. J. Howard and H. T. Stokes. “Group-Theoretical Analysis of Octahedral Tilting in Perovskites”. In: *Acta Crystallographica Section B* 54.6 (1998), pp. 782–789.

[179] A.P. Jones, F. Wall, and C.T. Williams. *Rare Earth Minerals: Chemistry, Origin and Ore Deposits*. The Mineralogical Society Series. Springer, 1996.

[180] Martin A. Green, Anita Ho-Baillie, and Henry J. Snaith. “The emergence of perovskite solar cells”. In: *Nature Photonics* 8.7 (2014), pp. 506–514.

[181] Ulrich Müller. *Inorganic structural chemistry*. 04; QD151. 2, M8. New York, 1993.

[182] Alexander Frank Wells. *Structural inorganic chemistry*. Oxford university press, 2012.

[183] Mats Johnsson and Peter Lemmens. *Handbook of Magnetism and Advanced Magnetic Materials*. American Cancer Society, 2007.

[184] David B Mitzi. "Progress in inorganic chemistry". In: *Synthesis, Structure, and Properties of Organic-Inorganic Perovskites and Related Materials* (1999), pp. 1–121.

[185] Yongbo Yuan and Jinsong Huang. "Ion Migration in Organometal Trihalide Perovskite and Its Impact on Photovoltaic Efficiency and Stability". In: *Accounts of Chemical Research* 49.2 (2016), pp. 286–293.

[186] Bin-Bin Zhang et al. "Defect proliferation in CsPbBr3 crystal induced by ion migration". In: *Applied Physics Letters* 116.6 (2020), p. 063505.

[187] Constantinos C. Stoumpos, Christos D. Malliakas, and Mercouri G. Kanatzidis. "Semiconducting Tin and Lead Iodide Perovskites with Organic Cations: Phase Transitions, High Mobilities, and Near-Infrared Photoluminescent Properties". In: *Inorganic Chemistry* 52.15 (2013), pp. 9019–9038.

[188] Haotong Wei et al. "Sensitive X-ray detectors made of methylammonium lead tribromide perovskite single crystals". In: *Nature Photonics* 10.5 (2016), pp. 333–339.

[189] Michael Saliba et al. "Cesium-containing triple cation perovskite solar cells: improved stability, reproducibility and high efficiency". In: *Energy Environ. Sci.* 9 (6 2016), pp. 1989–1997.

[190] Kihyung Sim et al. "Performance boosting strategy for perovskite light-emitting diodes". In: *Applied Physics Reviews* 6.3 (2019), p. 031402.

[191] He Huang et al. "Colloidal lead halide perovskite nanocrystals: synthesis, optical properties and applications". In: *NPG Asia Mater.* 8.11 (2016), e328.

[192] Yang-Fan Xu et al. "A CsPbBr3 Perovskite Quantum Dot/Graphene Oxide Composite for Photocatalytic CO2 Reduction". In: *Journal of the American Chemical Society* 139.16 (2017), pp. 5660–5663.

[193] Yihui He et al. "High spectral resolution of gamma-rays at room temperature by perovskite CsPbBr3 single crystals". In: *Nature Communications* 9.1 (2018), p. 1609.

[194] Mojtaba Abdi-Jalebi et al. "Maximizing and stabilizing luminescence from halide perovskites with potassium passivation". In: *Nature* 555.7697 (2018), pp. 497–501.

[195] Eric G. Tulsky and Jeffrey R. Long. "Dimensional Reduction: A Practical Formalism for Manipulating Solid Structures". In: *Chemistry of Materials* 13.4 (2001), pp. 1149–1166.

[196] Ian C. Smith et al. "A Layered Hybrid Perovskite Solar-Cell Absorber with Enhanced Moisture Stability". In: *Angewandte Chemie International Edition* 53.42 (2014), pp. 11232–11235.

[197] Duyen H. Cao et al. "2D Homologous Perovskites as Light-Absorbing Materials for Solar Cell Applications". In: *Journal of the American Chemical Society* 137.24 (2015), pp. 7843–7850.

[198] Constantinos C. Stoumpos et al. "Ruddlesden–Popper Hybrid Lead Iodide Perovskite 2D Homologous Semiconductors". In: *Chemistry of Materials* 28.8 (2016), pp. 2852–2867.

[199] Julian Gebhardt, Youngkuk Kim, and Andrew M. Rappe. "Influence of the Dimensionality and Organic Cation on Crystal and Electronic Structure of Organometallic Halide Perovskites". In: *The Journal of Physical Chemistry C* 121.12 (2017), pp. 6569–6574.

[200] Ashutosh Giri et al. "Ultralow Thermal Conductivity of Two-Dimensional Metal Halide Perovskites". In: *Nano Letters* 20.5 (2020), pp. 3331–3337.

[201] Magnus B. Fridriksson, Sudeep Maheshwari, and Ferdinand C. Grozema. "Structural Dynamics of Two-Dimensional Ruddlesden–Popper Perovskites: A Computational Study". In: *The Journal of Physical Chemistry C* 124.40 (2020), pp. 22096–22104.

[202] Laurent Pedesseau et al. "Advances and Promises of Layered Halide Hybrid Perovskite Semiconductors". In: *ACS Nano* 10.11 (2016), pp. 9776–9786.

[203] Letian Dou. "Emerging two-dimensional halide perovskite nanomaterials". In: *J. Mater. Chem. C* 5 (43 2017), pp. 11165–11173.

[204] Enzheng Shi et al. "Two-dimensional halide perovskite nanomaterials and heterostructures". In: *Chem. Soc. Rev.* 47 (16 2018), pp. 6046–6072.

[205] Matthew D. Smith et al. "The Diversity of Layered Halide Perovskites". In: *Annual Review of Materials Research* 48.1 (2018), pp. 111–136.

[206] Duyen H. Cao et al. "Thin Films and Solar Cells Based on Semiconducting Two-Dimensional Ruddlesden–Popper $(CH_3(CH_2)_3NH_3)_2(CH_3NH_3)_{n-1}Sn_nI_{3n+1}$ Perovskites". In: *ACS Energy Letters* 2.5 (2017), pp. 982–990.

[207] Yuqin Liao et al. "Highly Oriented Low-Dimensional Tin Halide Perovskites with Enhanced Stability and Photovoltaic Performance". In: *Journal of the American Chemical Society* 139.19 (2017), pp. 6693–6699.

[208] X. Hong, T. Ishihara, and A. V. Nurmikko. "Dielectric confinement effect on excitons in PbI_4-based layered semiconductors". In: *Phys. Rev. B* 45 (12 1992), pp. 6961–6964.

[209] Yani Chen et al. “2D Ruddlesden–Popper Perovskites for Optoelectronics”. In: *Advanced Materials* 30.2 (2018), p. 1703487.

[210] Omer Yaffe et al. “Excitons in ultrathin organic-inorganic perovskite crystals”. In: *Phys. Rev. B* 92 (4 2015), p. 045414.

[211] Dewei Ma et al. “Single-crystal microplates of two-dimensional organic–inorganic lead halide layered perovskites for optoelectronics”. In: *Nano Research* 10 (6 2017), pp. 2117–2129.

[212] Bo Li et al. “Colloidal engineering for monolayer CH3NH3PbI3 films toward high performance perovskite solar cells”. In: *J. Mater. Chem. A* 5 (46 2017), pp. 24168–24177.

[213] Bettina V. Lotsch. “New Light on an Old Story: Perovskites Go Solar”. In: *Angewandte Chemie International Edition* 53.3 (2014), pp. 635–637.

[214] Aslihan Babayigit et al. “Assessing the toxicity of Pb- and Sn-based perovskite solar cells in model organism Danio rerio”. In: *Scientific Reports* 6.1 (2016), p. 18721.

[215] Peidong Su et al. “Pb-Based Perovskite Solar Cells and the Underlying Pollution behind Clean Energy: Dynamic Leaching of Toxic Substances from Discarded Perovskite Solar Cells”. In: *The Journal of Physical Chemistry Letters* 11.8 (2020), pp. 2812–2817.

[216] Tom Baikie et al. “Synthesis and crystal chemistry of the hybrid perovskite (CH3NH3)PbI3 for solid-state sensitised solar cell applications”. In: *J. Mater. Chem. A* 1 (18 2013), pp. 5628–5641.

[217] Feng Hao et al. “Lead-free solid-state organic–inorganic halide perovskite solar cells”. In: *Nature Photonics* 8.6 (2014), pp. 489–494.

[218] Nakita K. Noel et al. “Lead-free organic–inorganic tin halide perovskites for photovoltaic applications”. In: *Energy Environ. Sci.* 7 (9 2014), pp. 3061–3068.

[219] Sabine Körbel, Miguel A. L. Marques, and Silvana Botti. “Stability and electronic properties of new inorganic perovskites from high-throughput ab initio calculations”. In: *J. Mater. Chem. C* 4 (15 2016), pp. 3157–3167.

[220] Sami Vasala and Maarit Karppinen. “A2B’B”O6 perovskite: A review”. In: *Prog. Solid State Chem.* 43.1-2 (2015), pp. 1–36.

[221] Adam H. Slavney et al. “A pencil-and-paper method for elucidating halide double perovskite band structures”. In: *Chem. Sci.* 10 (48 2019), pp. 11041–11053.

[222] Felix A. Faber et al. “Machine Learning Energies of 2 Million Elpasolite (ABC2D6) Crystals”. In: *Phys. Rev. Lett.* 117.13 (2016), p. 135502.

[223] Marina R. Filip and Feliciano Giustino. “The geometric blueprint of perovskites”. In: *Proc. Nat. Acad. Sci.* 115.21 (2018), pp. 5397–5402.

[224] A. H. Slavney et al. “A Bismuth-Halide Double Perovskite with Long Carrier Recombination Lifetime for Photovoltaic Applications”. In: *J. Am. Chem. Soc.* 138.7 (2016), pp. 2138–2141.

[225] Eric T. McClure et al. “Cs_2AgBiX_6 (X = Br, Cl): New Visible Light Absorbing, Lead-Free Halide Perovskite Semiconductors”. In: *Chem. Matter.* 28.5 (2016), pp. 1348–1354.

[226] Marina R. Filip et al. “Band Gaps of the Lead-Free Halide Double Perovskites Cs2BiAgCl6 and Cs2BiAgBr6 from Theory and Experiment”. In: *J. Phys. Chem. Lett.* 7.13 (2016), pp. 2579–2585.

[227] Zeyu Deng et al. “Exploring the properties of lead-free hybrid double perovskites using a combined computational-experimental approach”. In: *J. Mater. Chem. A* 4 (2016), pp. 12025–12029.

[228] Lamjed Debbichi et al. “Mixed Valence Perovskite Cs2Au2I6 : A Potential Material for Thin-Film Pb-Free Photovoltaic Cells with Ultrahigh Efficiency”. In: *Adv. Mater.* 30.12 (2018), p. 1707001.

[229] Bin Yang et al. “Lead-Free Silver-Bismuth Halide Double Perovskite Nanocrystals”. In: *Angew. Chem., Int. Ed.* 57 (2018), pp. 5359–5363.

[230] Jiajun Luo et al. “Efficient and stable emission of warm-white light from lead-free halide double perovskites”. In: *Nature* 563.7732 (2018), pp. 541–545.

[231] Koushik Biswas and Mao Hua Du. “Energy transport and scintillation of cerium-doped elpasolite Cs 2LiYCl 6: Hybrid density functional calculations”. In: *Phys. Rev. B* 86.1 (2012), pp. 1–7.

[232] Kenichiro Tanaka et al. “Image charge effect on two-dimensional excitons in an inorganic-organic quantum-well crystal”. In: *Phys. Rev. B* 71 (4 2005), p. 045312.

[233] Jacky Even, Laurent Pedesseau, and Claudine Katan. “Understanding quantum confinement of charge carriers in layered 2D hybrid perovskites”. In: *Chem Phys Chem* 15.17 (2014), pp. 3733–3741.

[234] Archana Raja et al. “Coulomb engineering of the bandgap and excitons in two-dimensional materials”. In: *Nature Communications* 8 (2017), pp. 1–7.

[235] Yeongsu Cho and Timothy C. Berkelbach. “Environmentally sensitive theory of electronic and optical transitions in atomically thin semiconductors”. In: *Phys. Rev. B* 97.4 (2018), 041409(R).

[236] J. C. Blancon et al. “Scaling law for excitons in 2D perovskite quantum wells”. In: *Nature Comm.* 9.1 (2018), p. 2254.

[237] Mikaël Kepenekian et al. “Concept of Lattice Mismatch and Emergence of Surface States in Two-dimensional Hybrid Perovskite Quantum Wells”. In: *Nano Letters* 18.9 (2018), pp. 5603–5609.

[238] J. Even et al. “Electronic model for self-assembled hybrid organic perovskite semiconductors: Reverse band edge electronic states ordering and spin-orbit coupling”. In: *Phys. Rev. B* 86 (20 2012), p. 205301.

[239] J.-C. Blancon et al. “Extremely efficient internal exciton dissociation through edge states in layered 2D perovskites”. In: *Science* 355.6331 (2017), pp. 1288–1292.

[240] Scott Silver et al. “Characterization of the Valence and Conduction Band Levels of n = 1 2D Perovskites: A Combined Experimental and Theoretical Investigation”. In: *Advanced Energy Materials* 8.16 (2018), p. 1703468.

[241] Ke-zhao Du et al. “Two-Dimensional Lead(II) Halide-Based Hybrid Perovskites Templated by Acene Alkylamines: Crystal Structures, Optical Properties, and Piezoelectricity”. In: *Inorganic Chemistry* 56.15 (2017), pp. 9291–9302.

[242] David G. Billing and Andreas Lemmerer. “Synthesis, characterization and phase transitions in the inorganic–organic layered perovskite-type hybrids $[(C_nH_2n + 1NH_3)_2PbI_4]$, $n = 4$, 5 and 6”. In: *Acta Crystallographica Section B* 63.5 (2007), pp. 735–747.

[243] James Endres et al. “Valence and Conduction Band Densities of States of Metal Halide Perovskites: A Combined Experimental–Theoretical Study”. In: *The Journal of Physical Chemistry Letters* 7.14 (2016), pp. 2722–2729.

[244] Shuxia Tao et al. “Absolute energy level positions in tin- and lead-based halide perovskites”. In: *Nature Communications* 10.1 (2019), pp. 2041–1723.

[245] Gang Tang et al. “Revealing the role of thiocyanate anion in layered hybrid halide perovskite (CH3NH3)2Pb(SCN)2I2”. In: *The Journal of Chemical Physics* 146.22 (2017), p. 224702.

[246] Yu-Qing Zhao et al. “Layer-dependent transport and optoelectronic property in two-dimensional perovskite: (PEA)2PbI4”. In: *Nanoscale* 10 (18 2018), pp. 8677–8688.

[247] Sheng Liu et al. “Manipulating efficient light emission in two-dimensional perovskite crystals by pressure-induced anisotropic deformation”. In: *Science Advances* 5.7 (2019).

[248] Ryan A. DeCrescent et al. “Bright magnetic dipole radiation from two dimensional lead-halide perovskites”. In: *Science Advances* 6.6 (2020).

[249] Lei Zhang and WanZhen Liang. “How the Structures and Properties of Two-Dimensional Layered Perovskites MAPbI3 and CsPbI3 Vary with the Number of Layers”. In: *The Journal of Physical Chemistry Letters* 8.7 (2017), pp. 1517–1523.

[250] R. D. Shannon. “Revised effective ionic radii and systematic studies of interatomic distances in halides and chalcogenides”. In: *Acta Crystallographica Section A* 32.5 (1976), pp. 751–767.

[251] Laura Schade et al. “Structural and Optical Properties of $Cs_2AgBiBr_6$ Double Perovskite”. In: *ACS Energy Letters* 4.1 (2019), pp. 299–305.

[252] Julian A. Steele et al. “Giant electron-phonon coupling and deep conduction band resonance in metal halide double perovskite”. In: *ACS Nano* 12.8 (2018), pp. 8081–8090.

[253] Wan Deng et al. “Synthesis of $Cs_2AgSbCl_6$ and improved optoelectronic properties of $Cs_2AgSbCl_6/TiO_2$ heterostructure driven by the interface effect for lead-free double perovskites solar cells”. In: *Appl. Phys. Lett.* 111 (2017), p. 151602.

[254] Jakob C. Dahl et al. “Probing the Stability and Band Gaps of $Cs_2AgInCl_6$ and $Cs_2AgSbCl_6$ Lead-Free Double Perovskite Nanocrystals”. In: *Chem. Mater.* 31 (2019), pp. 3134–3143.

[255] T. Thao Tran et al. “Designing indirect-direct bandgap transitions in double perovskites”. In: *Mater. Horiz.* 4.4 (2017), pp. 688–693.

[256] Ying Liu et al. “Lead-Free Double Perovskite $Cs_2AgInCl_6$”. In: *Angewandte Chemie International Edition* 60.21 (2020), pp. 11592–11603.

[257] George Volonakis et al. “Cs2InAgCl6: A New Lead-Free Halide Double Perovskite with Direct Band Gap”. In: *The Journal of Physical Chemistry Letters* 8.4 (2017), pp. 772–778.

[258] Jun Zhou et al. “Composition design, optical gap and stability investigations of lead-free halide double perovskite $Cs_2AgInCl_6$”. In: *Journal of Materials Chemistry A* 5.29 (2017), pp. 15031–15037.

[259] Fangyi Zhao et al. “Double perovskite $Cs_2AgInCl_6$:Cr3+: broadband and near-infrared luminescent materials”. In: *Inorg. Chem. Front.* 6.12 (2019), pp. 3621–3628.

[260] Wentiao Wu et al. “Investigation of the Mn dopant-enhanced photoluminescence performance of lead-free $Cs_2AgInCl_6$ double perovskite crystals”. In: *Phys. Chem. Chem. Phys.* 22.4 (2020), pp. 1815–1819.

[261] Yanqi Luo et al. “Direct Observation of Halide Migration and its Effect on the Photoluminescence of Methylammonium Lead Bromide Perovskite Single Crystals”. In: *Advanced Materials* 29.43 (2017), p. 1703451.

[262] Federico Locardi et al. “Colloidal Synthesis of Double Perovskite $Cs_2AgInCl_6$ and Mn-Doped $Cs_2AgInCl_6$ Nanocrystals”. In: *J. Am. Chem. Soc.* 140.40 (2018), pp. 12989–12995.

[263] Ankit Jain, Oleksandr Voznyy, and Edward H. Sargent. “High-Throughput Screening of Lead-Free Perovskite-like Materials for Optoelectronic Applications”. In: *J. Phys. Chem. C* 121.13 (2017), pp. 7183–7187.

[264] Bridget A. Connor et al. “Layered Halide Double Perovskites: Dimensional Reduction of $Cs_2AgBiBr_6$”. In: *J. Am. Chem. Soc.* 140.15 (2018), pp. 5235–5240.

[265] Mark S Hybertsen and Steven G Louie. “Ab initio static dielectric matrices from the density-functional approach. I Formulation and application to semiconductors and insulators”. In: *Phys. Rev. B* 35.11 (1987), p. 5585.

[266] Federico Brivio et al. “Relativistic quasiparticle self-consistent electronic structure of hybrid halide perovskite photovoltaic absorbers”. In: *Phys. Rev. B* 89.15 (2014), p. 155204.

[267] Bayrammurad Saparov and David B. Mitzi. “Organic–Inorganic Perovskites: Structural Versatility for Functional Materials Design”. In: *Chemical Reviews* 116.7 (2016), pp. 4558–4596.

[268] Laura M. Castro-Castro and Arnold M. Guloy. “Organic-Based Layered Perovskites of Mixed-Valent Gold(I)/Gold(III) Iodides”. In: *Angewandte Chemie International Edition* 42.24 (2003), pp. 2771–2774.

[269] Le-Yu Bi et al. “Two-dimensional lead-free iodide-based hybrid double perovskites: crystal growth, thin-film preparation and photocurrent responses”. In: *J. Mater. Chem. A* 7 (34 2019), pp. 19662–19667.

[270] Bridget A. Connor et al. “Dimensional reduction of the small-bandgap double perovskite Cs2AgTlBr6”. In: *Chem. Sci.* 11 (29 2020), pp. 7708–7715.

[271] A. H. Slavney et al. “Small-Band-Gap Halide Double Perovskites”. In: *Angew. Chem. Int. Ed.* 57 (2018), pp. 12765–12770.

[272] Nattamai S. P. Bhuvanesh and Jagannatha Gopalakrishnan. “Solid-state chemistry of early transition-metal oxides containing d0 and d1 cations”. In: *J. Mater. Chem.* 7 (12 1997), pp. 2297–2306.

[273] Thomas A. Kodenkandath and John B. Wiley. “Synthesis and structure of a double-layered perovskite and its hydrate, K2SrTa2O7·mH2O (m = 0, 2)”. In: *Materials Research Bulletin* 35.10 (2000), pp. 1737–1742.

[274] Lingling Mao et al. “Chemical and Structural Diversity of Hybrid Layered Double Perovskite Halides”. In: *Journal of the American Chemical Society* 141.48 (2019), pp. 19099–19109.

[275] Andrea Splendiani et al. “Emerging Photoluminescence in Monolayer MoS2”. In: *Nano Letters* 10.4 (2010), pp. 1271–1275.

[276] Kin Fai Mak et al. “Atomically Thin MoS_2: A New Direct-Gap Semiconductor”. In: *Phys. Rev. Lett.* 105 (13 2010), p. 136805.

[277] Robin Kentsch et al. “Exciton Dynamics and Electron-Phonon Coupling Affect the Photovoltaic Performance of the $Cs_2AgBiBr_6$ Double Perovskite”. In: *Journal of Physical Chemistry C* 122.45 (2018), pp. 25940–25947.

[278] Julian A. Steele et al. “Photophysical Pathways in Highly Sensitive Cs 2 AgBiBr 6 Double-Perovskite Single-Crystal X-Ray Detectors”. In: *Advanced Materials* 30.46 (2018), pp. 1–7.

[279] S. J. Zelewski et al. “Revealing the nature of photoluminescence emission in the metal-halide double perovskite $Cs_2AgBiBr_6$”. In: *Journal of Materials Chemistry C* 7.27 (2019), pp. 8350–8356.

[280] Giulia Longo et al. “Understanding the Performance-Limiting Factors of Cs 2 AgBiBr 6 Double-Perovskite Solar Cells”. In: *ACS Energy Lett.* 5 (2020), pp. 2200–2207.

[281] R. J. Elliott. “Intensity of optical absorption by excitons”. In: *Physical Review* 108.6 (1957), pp. 1384–1389.

[282] Marina R. Filip et al. “Steric engineering of metal-halide perovskites with tunable optical band gaps”. In: *Nat. Comm.* 5 (2014), p. 5757.

[283] Menno Bokdam et al. “Role of Polar Phonons in the Photo Excited State of Metal Halide Perovskites”. In: *Sci. Rep.* 6.i (2016), p. 28618.

[284] Gregory H. Wannier. “The Structure of Electronic Excitation Levels in Insulating Crystals”. In: *Phys. Rev.* 52.3 (1937), pp. 191–197.

[285] Claus F. Klingshirn. *Semiconductor Optics.* Berlin: Springer, 2005.

[286] Arno Schindlmayr. “Excitons with anisotropic effective mass”. In: *Euro. J. Phys.* 18.5 (1997), pp. 374–376.

[287] Steven G. Louie, James R. Chelikowsky, and Marvin L. Cohen. “Local-field effects in the optical spectrum of silicon”. In: *Phys. Rev. Lett.* 34.3 (1975), pp. 155–158.

[288] Peter Puschnig and Claudia Ambrosch-Draxl. “Optical absorption spectra of semiconductors and insulators including electron-hole correlations: An ab initio study within the LAPW method”. In: *Phys. Rev. B* 66.16 (2002), p. 165105.

[289] Peigeng Han et al. “Size effect of lead-free halide double perovskite on luminescence property”. In: *Sci. China Chem.* 62 (2019), pp. 1405–1413.

[290] Mingzhen Liu, Michael B. Johnston, and Henry J. Snaith. “Efficient planar heterojunction perovskite solar cells by vapour deposition”. In: *Nature* 501.7467 (2013), pp. 395–398.

[291] Samuel D. Stranks and Henry J. Snaith. “Metal-halide perovskites for photovoltaic and light-emitting devices”. In: *Nature Nanotechnology* 10.5 (2015), pp. 391–402.

[292] Zhi-Kuang Tan et al. “Bright light-emitting diodes based on organo- metal halide perovskite”. In: *Nature Nanotechnology* 9.9 (2014), pp. 687–692.

[293] Yichuan Ling et al. “Bright Light-Emitting Diodes based on organo- metal halide perovskite nanoplatelets”. In: *Advanced Materials* 28.2 (2016), pp. 305–311.

[294] Makhsud I. Saidaminov et al. "Inorganic Lead Halide Perovskite Single Crystals: Phase-Selective Low-Temperature Growth, Carrier Transport Properties, and Self-Powered Photodetection". In: *Advanced Optical Materials* 5.2 (2017), p. 1600704.

[295] Jianxu Ding et al. "High Detectivity and Rapid Response in Perovskite CsPbBr3 Single-Crystal Photodetector". In: *The Journal of Physical Chemistry C* 121.9 (2017), pp. 4917–4923.

[296] Peng Zhang et al. "Anisotropic Optoelectronic Properties of Melt-Grown Bulk CsPbBr3 Single Crystal". In: *The Journal of Physical Chemistry Letters* 9.17 (2018), pp. 5040–5046.

[297] Yang Zhou et al. "Metal Halide Perovskites for X-ray Imaging Scintillators and Detectors". In: *ACS Energy Letters* 6.2 (2021), pp. 739–768.

[298] Jia Liang et al. "All-Inorganic Perovskite Solar Cells". In: *Journal of the American Chemical Society* 138.49 (2016), pp. 15829–15832.

[299] Giorgio Schileo and Giulia Grancini. "Halide perovskites: current issues and new strategies to push material and device stability". In: *Journal of Physics: Energy* 2.2 (2020), p. 021005.

[300] Wan-Jian Yin, Tingting Shi, and Yanfa Yan. "Unusual defect physics in CH3NH3PbI3 perovskite solar cell absorber". In: *Applied Physics Letters* 104.6 (2014), p. 063903.

[301] Andrei Buin et al. "Materials Processing Routes to Trap-Free Halide Perovskites". In: *Nano Letters* 14.11 (2014), pp. 6281–6286.

[302] Andrei Buin et al. "Halide-Dependent Electronic Structure of Organo- lead Perovskite Materials". In: *Chemistry of Materials* 27.12 (2015), pp. 4405–4412.

[303] Banavoth Murali et al. "Surface Restructuring of Hybrid Perovskite Crystals". In: *ACS Energy Letters* 1.6 (2016), pp. 1119–1126.

[304] Huichao Zhang et al. "Phase segregation due to ion migration in all-inorganic mixed-halide perovskite nanocrystals". In: *Nature Communications* 10.1 (2019), p. 1088.

[305] David A. Egger, Leeor Kronik, and Andrew M. Rappe. "Theory of Hydrogen Migration in Organic–Inorganic Halide Perovskites". In: *Angewandte Chemie International Edition* 54.42 (2015), pp. 12437–12441.

[306] Jon M. Azpiroz et al. "Defect migration in methylammonium lead iodide and its role in perovskite solar cell operation". In: *Energy and Environmental Science* 8.7 (2015), pp. 2118–2127.

[307] Jun Haruyama et al. "First-principles study of ion diffusion in perovskite solar cell sensitizers". In: *Journal of the American Chemical Society* 137.32 (2015), pp. 10048–10051.

[308] Thijs J. A. M. Smolders, Alison B. Walker, and Matthew J. Wolf. "3D-to-2D Transition of Anion Vacancy Mobility in CsPbBr3 under Hydrostatic Pressure". In: *The Journal of Physical Chemistry Letters* 12.21 (2021), pp. 5169–5177.

[309] Junichiro Mizusaki, Kimiyasu Arai, and Kazuo Fueki. "Ionic conduction of the perovskite-type halides". In: *Solid State Ionics* 11.3 (1983), pp. 203–211.

[310] R. Lakshmi Narayan, M. V.S. Sarma, and S. V. Suryanarayana. "Ionic conductivity of CsPbCl3 and CsPbBr3". In: *Journal of Materials Science Letters* 6.1 (1987), pp. 93–94.

[311] Tae-Youl Yang et al. "The Significance of Ion Conduction in a Hybrid Organic–Inorganic Lead-Iodide-Based Perovskite Photosensitizer". In: *Angewandte Chemie International Edition* 54.27 (2015), pp. 7905–7910.

[312] Jin Wook Lee et al. "Verification and mitigation of ion migration in perovskite solar cells". In: *APL Materials* 7.4 (2019), p. 041111.

[313] Edoardo Mosconi and Filippo De Angelis. "Mobile Ions in Organohalide Perovskites: Interplay of Electronic Structure and Dynamics". In: *ACS Energy Letters* 1.1 (2016), pp. 182–188.

[314] Alessandro Senocrate et al. "The Nature of Ion Conduction in Methylammonium Lead Iodide: A Multimethod Approach". In: *Angewandte Chemie International Edition* 56.27 (2017), pp. 7755–7759.

[315] Ji Hui Yang et al. "Fast self-diffusion of ions in CH3NH3PbI3: The interstiticaly mechanism: Versus vacancy-assisted mechanism". In: *Journal of Materials Chemistry A* 4.34 (2016), pp. 13105–13112.

[316] Jun Kang and Lin-Wang Wang. "High Defect Tolerance in Lead Halide Perovskite CsPbBr3". In: *The Journal of Physical Chemistry Letters* 8.2 (2017), pp. 489–493.

[317] Jie Xing et al. "Ultrafast ion migration in hybrid perovskite polycrystalline thin films under light and suppression in single crystals". In: *Phys. Chem. Chem. Phys.* 18.44 (2016), p. 30484.

[318] Jae S. Yun et al. "Critical Role of Grain Boundaries for Ion Migration in Formamidinium and Methylammonium Lead Halide Perovskite Solar Cells". In: *Adv. Energy Mater.* 6.13 (2016), p. 1600330.

[319] Claudio Quarti et al. "Interplay of Orientational Order and Electronic Structure in Methylammonium Lead Iodide: Implications for Solar Cells Operation". In: *Chem. Mater.* 26.22 (2014), pp. 6557–6569.

[320] Raisa-Ioana Biega and Linn Leppert. "Halogen vacancy migration at surfaces of CsPbBr3 perovskites: insights from density functional theory". In: *Journal of Physics: Energy* 3.3 (2021), p. 034017.

[321] Omer Yaffe et al. “Local Polar Fluctuations in Lead Halide Perovskite Crystals”. In: *Phys. Rev. Lett.* 118 (13 2017), p. 136001.

[322] Linghai Zhang and Patrick H.-L. Sit. “Ab initio study of the dynamics of electron trapping and detrapping processes in the CH3NH3PbI3 perovskite”. In: *J. Mater. Chem. A* 7 (5 2019), pp. 2135–2147.

[323] Lorenzo Malavasi, Craig A. J. Fisher, and M. Saiful Islam. “Oxide-ion and proton conducting electrolyte materials for clean energy applications: structural and mechanistic features”. In: *Chem. Soc. Rev.* 39 (11 2010), pp. 4370–4387.

[324] Masatomo Yashima et al. “Conduction path and disorder in the fast oxide-ion conductor (La0.8Sr0.2)(Ga0.8Mg0.15Co0.05)O2.8”. In: *Chem. Phys. Lett.* 380.3 (2003), pp. 391–396.

[325] Ana B. Muñoz-García et al. “Oxygen transport in perovskite-type solid oxide fuel cell materials: Insights from quantum mechanics”. In: *Acc. Chem. Res.* 47.11 (2014), pp. 3340–3348.

[326] Jingjing Xue, Rui Wang, and Yang Yang. “The surface of halide perovskites from nano to bulk”. In: *Nat. Rev. Mater.* 5.11 (2020), pp. 809–827.

[327] D. W. DeQuilettes et al. “Impact of microstructure on local carrier lifetime in perovskite solar cells”. In: *Science* 384 (2015), p. 683.

[328] Dane W. DeQuilettes et al. “Photo-induced halide redistribution in organic-inorganic perovskite films”. In: *Nat. Comm.* 7 (2016), p. 11683.

[329] Xu Liu et al. “Exploring Inorganic Binary Alkaline Halide to Passivate Defects in Low-Temperature-Processed Planar-Structure Hybrid Perovskite Solar Cells”. In: *Adv. Energy Mater.* 8.20 (2018), p. 1800138.

[330] Wei Chen et al. “Alkali Chlorides for the Suppression of the Interfacial Recombination in Inverted Planar Perovskite Solar Cells”. In: *Adv. Energy Mater.* 9.19 (2019), p. 1803872.

[331] Sofia Apergi, Geert Brocks, and Shuxia Tao. “Tuning the electronic levels of NiO with alkali halides surface modifiers for perovskite solar cells”. In: *Phys. Rev. Materials* 4 (8 2020), p. 085403.

[332] Yimu Chen et al. “Strain engineering and epitaxial stabilization of halide perovskites”. In: *Nature* 577 (7789 2020), pp. 209–215.

[333] Paolo Umari, Edoardo Mosconi, and Filippo De Angelis. “Infrared Dielectric Screening Determines the Low Exciton Binding Energy of Metal-Halide Perovskites”. In: *The Journal of Physical Chemistry Letters* 9.3 (2018), pp. 620–627.

[334] Amrita Dey et al. “Transfer of Direct to Indirect Bound Excitons by Electron Intervalley Scattering in $Cs_2AgBiBr_6$ Double Perovskite Nanocrystals”. In: *ACS Nano* 14 (2020), pp. 5855–5861.

[335] Charles Kittel. *Introduction to solid state physics (8th ed.)* John Wile & Sons., 2004.

[336] Martin Fuchs and Matthias Scheffler. "Ab initio pseudopotentials for electronic structure calculations of poly-atomic systems using density-functional theory". In: *Computer Physics Communications* 119.1 (1999), pp. 67–98.

[337] E. Fermi. "Displacement by Pressure of the High Lines of the Spectral Series". In: *Nuovo Cimento* 11 (1934), pp. 157–166.

[338] G. P. Srivastava and D. Weaire. "The theory of the cohesive energies of solids". In: *Advances in Physics* 36.4 (1987), p. 463517.

[339] P. E. Blöchl. "Projector augmented-wave method". In: *Phys. Rev. B* 50 (24 1994), pp. 17953–17979.

[340] N. A. W. Holzwarth et al. "Comparison of the projector augmented-wave, pseudopotential, and linearized augmented-plane-wave formalisms for density-functional calculations of solids". In: *Phys. Rev. B* 55 (4 1997), pp. 2005–2017.

[341] G. Kresse and D. Joubert. "From ultrasoft pseudopotentials to the projector augmented-wave method". In: *Phys. Rev. B* 59 (3 1999), pp. 1758–1775.

[342] D. R. Hamann, M. Schlüter, and C. Chiang. "Norm-Conserving Pseudopotentials". In: *Phys. Rev. Lett.* 43 (20 1979), pp. 1494–1497.

[343] G. B. Bachelet, D. R. Hamann, and M. Schlüter. "Pseudopotentials that work: From H to Pu". In: *Phys. Rev. B* 26 (8 1982), pp. 4199–4228.

[344] N. Troullier and José Luís Martins. "Efficient pseudopotentials for plane-wave calculations". In: *Phys. Rev. B* 43 (1991), pp. 1993–2006.

[345] Jack Deslippe et al. "BerkeleyGW: A massively parallel computer package for the calculation of the quasiparticle and optical properties of materials and nanostructures". In: *Comp. Phys. Comm.* 183.6 (2012), pp. 1269–1289.

[346] R. W. Godby and R. J. Needs. "Metal-insulator transition in Kohn-Sham theory and quasiparticle theory". In: *Phys. Rev. Lett.* 62 (1989), p. 1169.

[347] G. Kresse and J. Hafner. "Ab initio molecular dynamics for liquid metals". In: *Phys. Rev. B* 47 (1 1993), pp. 558–561.

[348] G. Kresse and J. Furthmuller. "Efficient iterative schemes for ab initio total-energy calculations using a plane-wave basis set". In: *Phys. Rev. B* 54 (16 1996), pp. 11169–11186.

[349] Jiri Klimes, Merzuk Kaltak, and Georg Kresse. "Predictive *GW* calculations using plane waves and pseudopotentials". In: *Phys. Rev. B* 90 (7 2014), p. 075125.

[350] John P. Perdew et al. "Restoring the Density-Gradient Expansion for Exchange in Solids and Surfaces". In: *Phys. Rev. Lett.* 100 (13 2008), p. 136406.

[351] Paolo Giannozzi et al. "QUANTUM ESPRESSO: a modular and open-source software project for quantum simulations of materials". In: *Journal of Physics: Condensed Matter* 21.39 (2009), p. 395502.

[352] P Giannozzi et al. "Advanced capabilities for materials modelling with QUANTUM ESPRESSO". In: *Journal of Physics: Condensed Matter* 29.46 (2017), p. 465901.

[353] Giovanni Pizzi et al. "Wannier90 as a community code: new features and applications". In: *Journal of Physics: Condensed Matter* 32.16 (2020), p. 165902.

[354] Alexandre Tkatchenko and Matthias Scheffler. "Accurate Molecular Van Der Waals Interactions from Ground-State Electron Density and Free-Atom Reference Data". In: *Phys. Rev. Lett.* 102 (7 2009), p. 073005.

[355] Carlos A. Lopez et al. "Crystal Structure Features of CsPbBr3 Perovskite Prepared by Mechanochemical Synthesis". In: *ACS Omega* 5.11 (2020), pp. 5931–5938.

Acknowledgments

During the past four years a lot of people helped me throughout one of the most exciting periods of my life. I reserve the next few lines to express my deepest gratitude and appreciation because without them the completion of this thesis would not have been possible. I am particularly grateful to the following people:

My supervisor, **Dr. Linn Leppert**, who guided me incessantly and helped me grow both as a researcher and as a human being. I have to thank her for all the exciting projects I was involved in and for the freedom she always granted me in choosing the topics that I liked the most and wanted to pursue in my research. Over the past four years, I saw nothing but enthusiasm towards my work, full dedication and constant support, encouragement and advice from her, even when nothing seemed to work. With immense patience and optimism, she was a true mentor and I do have to thank her for offering me this great opportunity of pursuing my PhD under her supervision, which proved to be one of the greatest adventures of my life.

Prof. Jeffrey Neaton and the entire Neaton group, for heaving me at UC Berkeley in my research exchange. They helped me understand what an academic life in a highly competitive and rewarding environment really means. They all showed me how important is to be part of a close-knit group of colleagues and friends who are always willing to help each other whether it comes to research or fun, with just as much enthusiasm.

Marina Filip, for dedicating so much of her time to introduce me to all that BSE formalism means. I am deeply grateful for our weekly discussions and her patience and availability in helping me whenever was necessary. We started as collaborators, but thanks to her kindness and joviality we soon became friends. I have to thank her for a nice and fruitful collaboration that I am sure will continue, as well as for all support and advice regarding this thesis.

John Mohanraj, for his willingness to always help me with any possible experiment and for performing the UPS measurements reported in section 3.2. I will terribly miss our endless discussions covering the broadest imaginable areas from perovskites to favorite dishes and from science to books, movies and latest developments worldwide. For almost three years, Monday evenings meant a lot of cakes, coffee and countless debates that I will never forget.

The entire **Leppert group** and especially to my office mate **Zoreh Hashemi** for the daily jovial atmosphere which made me look forward to a new day at the office and **Sonja Krach** who was very prompt in helping me with the translation needed in this thesis.

Monika Birkelbach, **Susanne Süss**, **Markus Hilt** and **Ingo Schelter** for being extremely responsive in helping me with any technical and administrative matter I encountered.

My family, and in particular my mom, who supported me unconditionally and was always there for me during the best, the worst and the hardest moments.

Last, but by no means least, I have to have to thank one person without whom I wouldn't be here today. I am incredibly grateful to my first physics teacher, **Florina Andrei**, who piqued my curiosity to discover how the world works and my interest in physics. Combining rigor with constant encouragement, she never ceased to motivate me and she always trusted that I would achieve everything I set out to do. For that I will owe her forever.

I further acknowledge financial and intellectual support from the Bavarian State Ministry of Science and the Arts through the Collaborative Research Network Solar Technologies go Hybrid (**SolTech**), the German Research Foundation (**DFG**) through the project **SFB840 B7** and program **GRK1640**.

For computational resources I am grateful to the Bavarian Polymer Institute (**BPI**), the Dutch national supercomputer **Cartesius** with the support of SURF Cooperative, **MESA+** Institute of Nanotechnology, and the National Energy Research Scientific Computing Center (**NERSC**).

Eidesstattliche Versicherung

Hiermit versichere ich an Eides statt, dass ich die vorliegende Arbeit selbstständig verfasst und keine anderen als die von mir angegebenen Quellen und Hilfdmittel verwendet habe.

Weiterhin erkläre ich, dass ich die Hilfe von gewerblichen Promotionsberatern bzw. -vermittlern oder ähnlichen Dienstleistern weder bisher in Anspruch genommen habe, noch künftig in Anspruch nehmen werde.

Zusätzlich erkläre ich hiermit, dass ich keinerlei frühere Promotionsversuche unternommen habe.

Bayreuth, den

Raisa-Ioana Biega